MaMaSELF

Master Program in Material Science

Diffraction investigation of the Half-Heusler to Full-Heusler transition in $Ni_{2-x}MnSb$

David Simonne, davidsimonne@tum.de

Heusler alloys can be divided into two important classes. If off-stochiometric full-Heusler (FH) X_2YZ alloys are famous for their ferromagnetic shape memory properties, half-Heusler (HH) alloys of formula XYZ have shown application in spintronics due to their ferromagnetic properties. Some systems present both structures as a function of temperature and/or composition.

It has been shown that magnetic transitions as well as structural transitions take place in the $Ni_{2-x}MnSb$ system. However, a half to full Heusler transition has never been studied precisely in term of long-range ordering, i.e. by scattering. Moreover, the kinetics of ordering at room temperature after a given heat treatment are still unknown. In this thesis we will present an overview of the crystalline structures of the system and of its temperature dependent half-Heusler to full-Heusler transition.

In-situ temperature dependent neutron powder diffraction (NPD) has been performed on samples with different concentrations x of Ni to have a better grasp of the atomic scale dynamics during the $C1_b$ - $L2_1$ phase transition. A particular emphasis has been put on instrumental corrections and refinement during this project. Ordering kinetics were determined by the extraction of both structural and dynamical information from diffractograms covering a wide range of temperature and composition in $Ni_{2-x}MnSb$.

Master Thesis (30 ECTS)
September 2019
Supervisor: Dr. Michael Leitner, Technische Universität München
Examiner: Prof. Dr. Wolfgang Schmahl, Ludwig-Maximilians-Universität München

Signed Declaration

David Simonne

I declare that this thesis was composed by myself, that the work contained herein is my own except where explicitly stated otherwise in the text, and that this work has not been submitted for any other degree or processional qualification except as specified.

Approved by:	Dr. Michael Leitner	Advisor
	Prof. Dr. Wolfgang Schmahl	MaMaSELF responsible for LMU
	David Simonne	Author

Acceptance date: September 30, 2019

I would like to thank my advisor Dr. Michael Leitner for taking me into his group at TUM and for having the time to help during my stay in Garching. Even if following your explanations were sometimes challenging, I truly learned a lot thanks to you during this master thesis. The advice were precious and helped me to familiarize myself with a new field. I came to Germany without much experience in programming applied to science or dynamics in hard condensed matter before this thesis and did not know what kind of research I would like to perform in the future. I think now that thanks to this thesis, I have discovered fields in which I would like to continue my research.

Dr. Di Matteo has always been very kind to me and it is thanks to him that I know about MaMaSELF and am part of this program. Along with the other physics professors in Rennes, he continuously kept my interest in physics high up during my bachelor and my first year of master.

Dr. Laurent Guérin made my life incredibly more interesting by sending me to Japan after my bachelor. At that time, I had in plan to participate in MaMaSELF but instead, I was allowed to discover a new country, new people, a new language while keeping on learning about physics. That time in Sendai also showed me how one could appreciate research in material Science.

Dr. Jean-François Moulin and his team at REFSANS in 2016 accompanied me thoughout my bachelor thesis. I would not have come back to Munich if I did not appreciate my time in their company.

Finally, I would like to thank Kim, Ulrike and Josef for spending time and sharing lunch with me in TUM. I would also like to thank my roommates in Munich, especially Brittany and Hsu with whom I had a great time in Germany.

In general, I would like to thank the whole MaMaSELF team, especially Christiane, Karin and Phillipe for making this adventure possible, along with the respective teams of Rennes, Montpellier, Torino and München where I had some of the best experiences in my life.
The last words are of course for my parents without whom it would not have been possible to do any of the above. Thank you Lucas for being a great brother and for pushing myself by also being a great scientist.

Contents

List of Figures

List of Tables

Chapter 1

Crystal structures, neutron diffraction, and experimental methods

The purpose of this thesis is to give a global understanding of a neutron diffraction experiment, from theory to data collection, correction and analysis, resulting in a precise understanding of how one can analyze and understand the ordering mechanism of the $C1_b$-$L2_1$ phase transition in the $Ni_{2-x}MnSb$ system. This first chapter will introduce the crystal structures of interest, the fundamentals of neutron diffraction and will as well give some insights into the instrumental setups that were used to provide the data.

1.1 Crystal structures

1.1.1 Heusler alloys

Our compounds belong to the family of Heusler alloys, named after the German engineer Friedrich Heusler who in 1903 discovered that some systems showed ferromagnetic properties despite having non-magnetic constituents (Heusler 1903; Heusler 1904).

There are two main different Heusler structures, full-Heusler alloys with the stochiometry 2:1:1 and half-Heusler alloys with the stochiometry 1:1:1. Half-Heusler alloys are typically written in the form XYZ, ranked by putting the most electropositive element first and the most electronegative element last. However, since we will use the X_2YZ configuration in the full-Heusler structure, the NiMnSb order is chosen where the element that is used twice in the full-Heusler configuration is put first and the most electronegative element is put at the end.

It has been shown that full-Heusler alloys of the formula Ni_2MnSb crystallize in the cubic $L2_1$ structure (Castelliz 1951; Szytuła et al. 1972) whereas half-Heusler NiMnSb alloys crystallize in the non-centrosymmetric cubic $C1_b$ structure (Ritchie et al. 2003; G. E. Bacon and Plant 1971). We could also have inverse Heuslers such as $NiMn_2Sb$ in which the Mn occupies the vacancy sublattice in the half-Heusler structure with the same $C1_b$ symmetry, this structure is however not relevant in the following discussions.

Half-Heusler alloys

The $C1_b$ structure has been defined as the space group 216 $F\bar{4}3m$ and can be understood as four interpenetrating FCC lattices centered on the Wickoff positions 4a, 4b, 4c and 4d respectively in (0, 0, 0), (1/2, 1/2, 1/2), (1/4, 1/4, 1/4) and (3/4, 3/4, 3/4) (Hahn 2006; G. E. Bacon and Plant 1971).

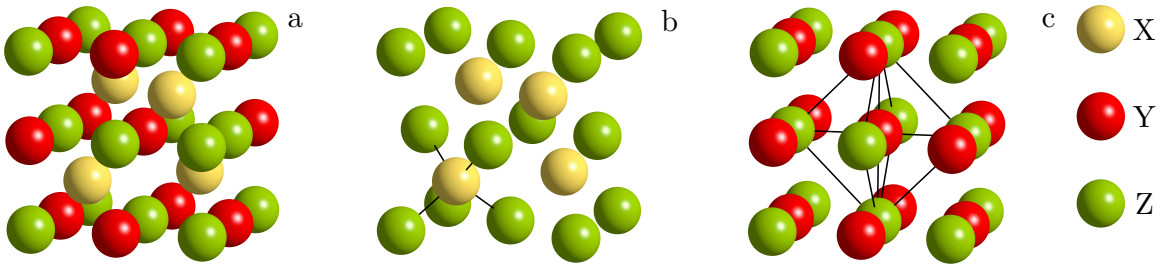

Figure 1.1: Half-Heusler structure (a) and its relation to the zinc blende structure (b) and to the rock salt structure(c).

The half-Heusler structure is commonly pictured as the sum of a covalent and an ionic part. For NiMnSb, Ni and Mn atoms have a distinct cationic character, whereas Sb can be seen as the anionic counterpart (Graf, Felser, and Parkin 2011). One can see in the figure 1.1 that a ZnS zinc blende sublattice occupying the Wyckoff positions 4a and 4c with its octahedral sites occupied (4b) leads to the structure of a half-Heusler alloy. This structure underlines the covalent bond that is determinant regarding the electronic properties the alloy (Webster 1968). Moreover, one can also notice a NaCl ordering on the position 4a and 4b. This salt structure emphasizes the ionic interaction between two elements who show respectively a cationic and anionic character. In the case of NiMnSb, Mn and Sb will build the NaCl rock salt structure whereas the Zinc blende structure is assumed by Ni and anionic Sb with Sb, Mn, Ni and vacancies respectively on the 4a, 4b, 4c and 4d Wyckoff sites.

Full-Heusler alloys

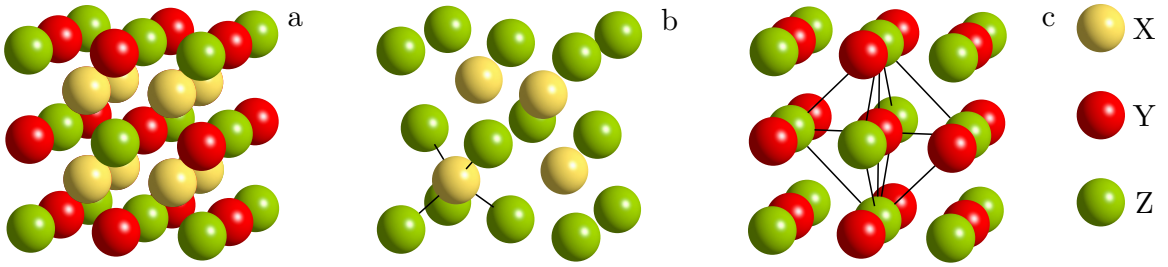

Figure 1.2: Full-Heusler structure (a) and its relation to the zinc blende structure (b) and to the rock salt structure(c).

Similar to the $C1_b$ structure, a rock salt-type lattice is formed by the least and most electropositive element (Mn and Sb). Due to the ionic character of their interaction, these elements are coordinated octahedrally. On the other hand, all hexahedral holes are filled by Ni with respect to the salt chloride structure. As seen in the figure 1.2 This structure can also be understood as a zinc blende-type sublattice, build up by

one Ni and Sb, the second Ni occupies the remaining tetrahedral holes, whereas Mn is located in the octahedral holes (Graf, Felser, and Parkin 2011).

The $L2_1$ structure has been defined as the space group 225 $Fm\bar{3}m$ with the Wickoff positions 4a (0, 0, 0), 4b (1/2, 1/2, 1/2) and 8c (1/4, 1/4, 1/4), (3/4, 3/4, 3/4) by Hahn (2006) also described with four interpenetrating FCC lattices centered in (0, 0, 0), (1/2, 1/2, 1/2), (1/4, 1/4, 1/4) and (3/4 3/4, 3/4). The Ni atoms are placed on the Wyckoff positions 8c, while the Y and the Z atoms are located at 4a and 4b, respectively.

1.1.2 $Ni_{2-x}MnSb$

In the frame of this thesis, we consider the full-Heusler Ni_2MnSb system and the half-Heusler NiMnSb as being quaternary Heusler alloys with the elements Ni, Ni or vacancies, Mn and Sb in terms of four interpenetrating FCC sub-lattices situated on the Wyckoff sites 4a, 4b, 4c and 4d with origins respectively at (0, 0, 0), (1/2, 1/2, 1/2), (1/4, 1/4, 1/4) and (3/4, 3/4, 3/4). This structure, as seen in figure 1.3 gives with the FCC translations 16 sites per unit cell, when Ni_2MnSb contains 16 atom per unit cell, NiMnSb contains only 12.

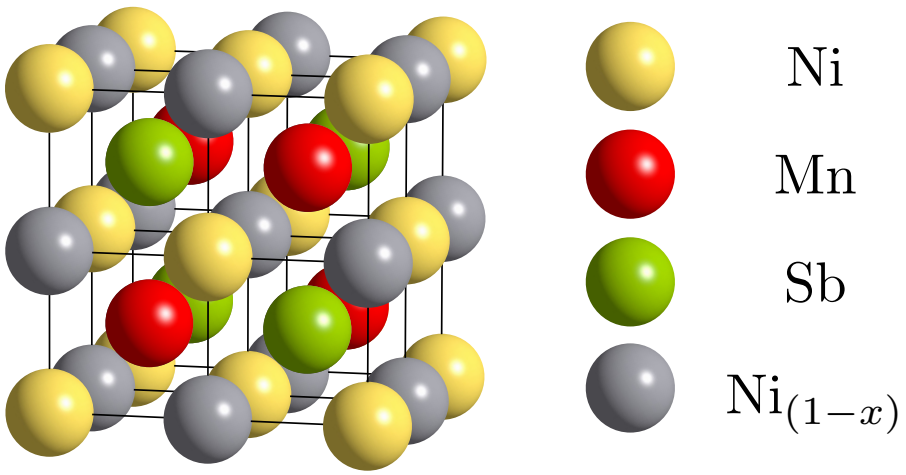

Figure 1.3: The $L2_1$ and $C1_b$ structure in $Ni_{2-x}MnSb$ depicted as four interpenetrating FCC lattices on the A (0,0,0), B(3/4, 3/4, 3/4), C(1/2, 1/2, 1/2) and D(1/4, 1/4, 1/4) as given by Webster (1984).

Additional structures are given in the figure 1.4, the use of brackets indicating a state of disorder. BCC A2, space group 229 ($Im\bar{3}m$) corresponds to a state of full disorder where Ni, Ni_{1-x}, Mn and Sb each randomly occupy one of the four FCC lattices in the ($NiNi_{1-x}MnSb$) system. B2, space group 221 ($Pm\bar{3}m$) corresponds to a structure derived from the A2 structure where ordering occurred on the 1a and 1b Wyckoff position, resulting in a ($NiNi_{1-x}$) (MnSb) system. The difference between B2 and $L2_1$ would then reside in an NaCl ordering of Mn and Sb where Ni and Ni(1-x) randomly occupy the 8c sites. The final transition to a $C1_b$ system would be the result of a breaking of symmetry leading to a phase transition where the vacancy would go from an equal distribution between the 4a and 4b sites to exclusively occupying the 4b site. The A2 structure is not observed but will be used during the refinement (Chapter 3) for normalisation purposes.

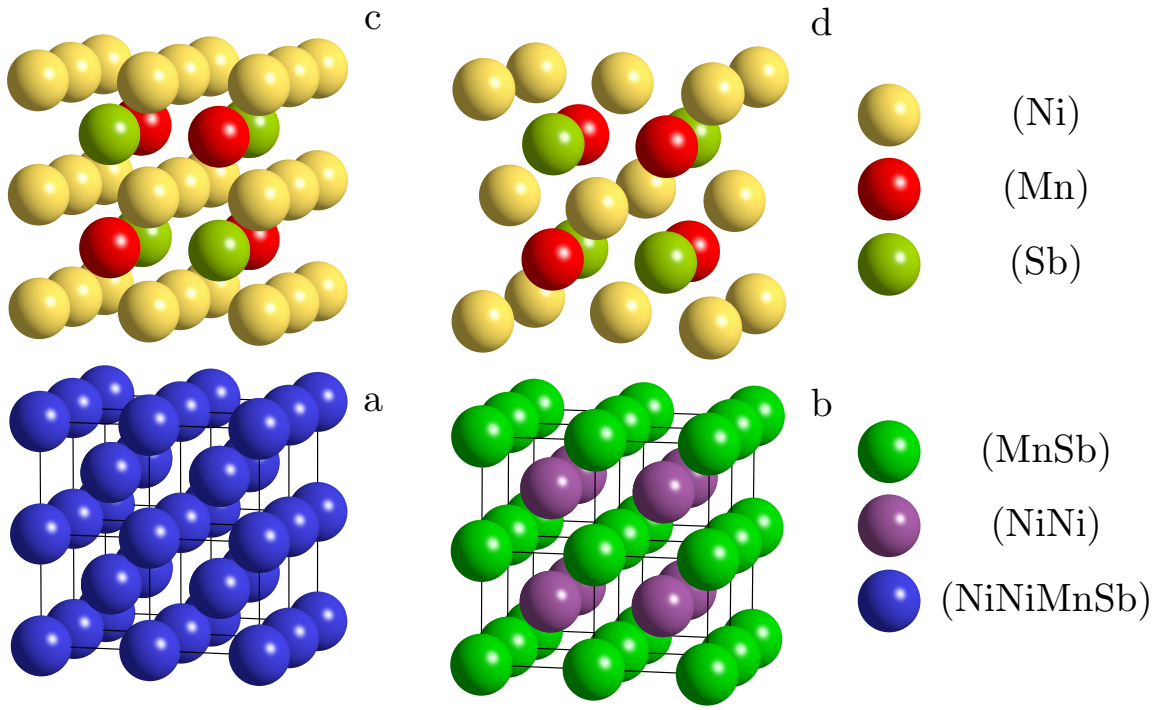

Figure 1.4: The A2 (a), B2 (b), full-Heusler $L2_1$ (c) and half-Heusler $C1_b$ (d) structures. NiMnSb and Ni_2MnSb here illustrate both full-Heusler and half-Heusler crystal structures. One can see that a C1b structure can transfer into a L21 structure via accommodating the Ni atoms equally on the 4a and 4b Wyckoff sites.

1.2 Neutron diffraction

The method that was chosen to extract information about the crystalline system is neutron powder diffraction, the following section will discuss the properties of the neutron in details and its interaction with matter.

Basic properties of the neutron

In the following paragraphs, the major physical concepts that are needed to understand neutron scattering will be introduced. Neutrons are subatomic particles of neutral charge. They were discovered in the year 1932 by James Chadwick when he bombarded boron with alpha particles.

Neutrons can be produced either by nuclear fission or by spallation. Nuclear fission is accompanied by the emission of neutrons; it provides a constant neutron flux from nuclear reactors as in FRMII, Munich, where the nuclear fission of uranium is used.

Spallation, however, uses an accelerated proton beam that, by hitting a heavy metal target, expels neutrons that are then used by the instruments. Shortly, spallation is more expensive but more flexible than nuclear fission, allowing for pulsed beams to be used easily. The Institut Laue Langevin (ILL) is an example of a fission reactor in Grenoble, where highly-enriched ^{235}U is used to produce neutrons. To counter the heat that is permanently produced by the reactions inside the reactor, heavy water (D_2O) is used as a moderator. It is preferred to H_2O since it has a low neutron absorption cross section compared to light water. A radiation shield is also provided by light water surrounding the reactor.

The neutrons are then collected in a moderator where they scatter inelastically. The scattering being a statistical process, the energy of the neutrons will satisfy a Maxwellian flux distribution defined by:

$$\phi(v) \propto v^3 \exp\left\{\frac{-mv^2}{2k_BT}\right\} \tag{1.1}$$

with $\phi(v)dv$ is the number of neutrons through unit area per second with velocities between v and dv, m is the mass of the neutron, and k_B is the Boltzmann constant. The maximum of the Maxwellian flux distribution is given for:

$$v = \left(\frac{3k_BT}{m}\right)^{1/2} \tag{1.2}$$

We can then write the mean energy of neutrons:

$$E = \frac{3}{2}k_BT = \frac{1}{2}mv^2 \tag{1.3}$$

that is conventionally approximated as:

$$E = k_BT \tag{1.4}$$

Neutrons can not only be seen as particle but also as waves, whose wavelength is defined by the De Broglie wavelength:

$$\lambda = \frac{h}{mv} = \frac{h}{\sqrt{2mE}} \tag{1.5}$$

with h being the Planck constant, p the momentum of the neutron and k the wavevector defined as:

$$p = \hbar k \tag{1.6}$$

$$k = \frac{2\pi}{\lambda} \tag{1.7}$$

To give an order of magnitude, a temperature of 293 K would give a mean wavelength of about 1.8 Angström and an energy of about 25 meV (of the order of molecular/ lattice excitations).

Sometimes, it is preferable to use neutrons of higher or lower energy to have a better flux of neutrons at a selected wavelength. Inside the laboratoire Léon Brillouin (LLB), Saclay, France, as in most of the modern neutron facilities, moderators of different temperatures are used to modify the Maxwell distribution and to produce hot or cold neutrons (figure 1.5). For the cold sources, liquid hydrogen insures the role of moderator whereas for the hot source, the moderator consists of a cylinder of graphite heated by the γ rays of the reactors (The reactor and the neutron sources 2003). Moderation is also done by the water surrounding the core, necessary to convert the MeV-neutrons after fission to useable energies.

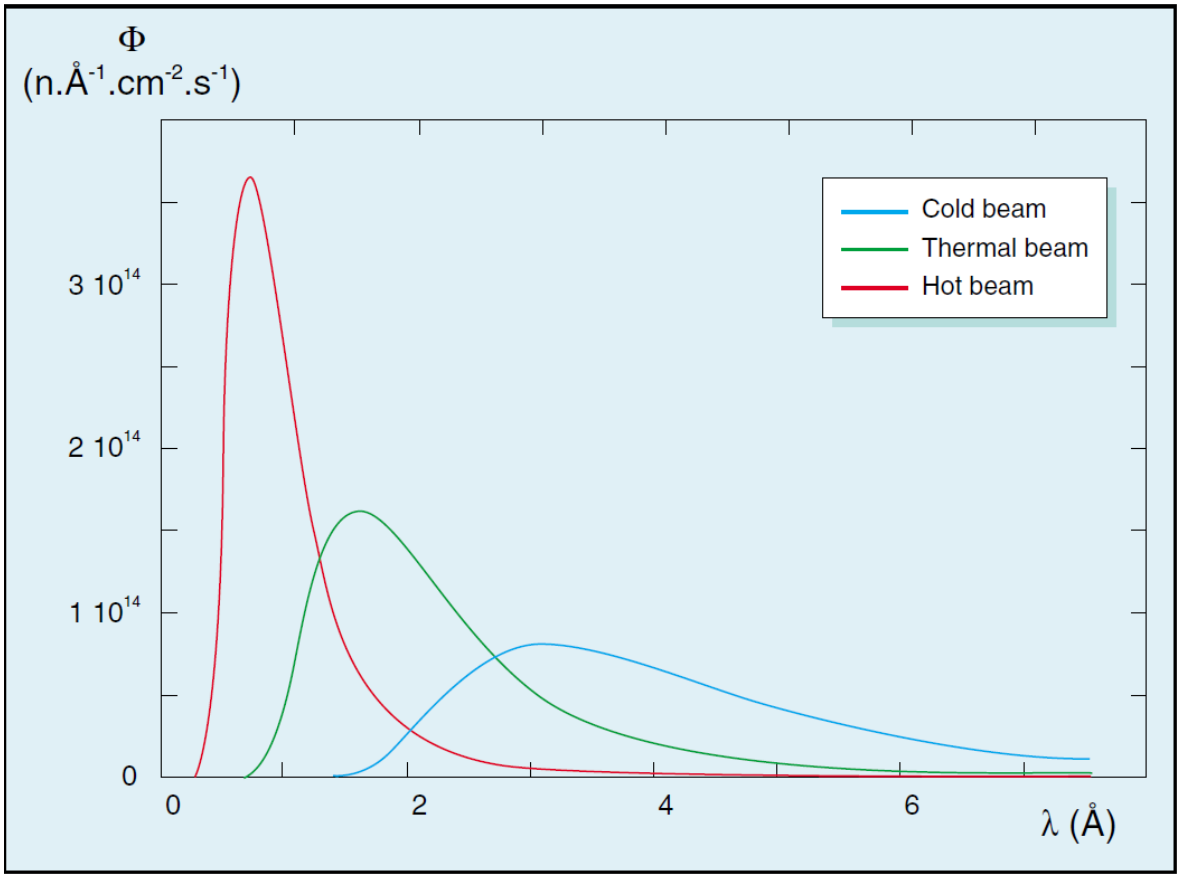

Figure 1.5: The evolution of the flux of neutrons versus the wavelength (hence the energy) of the neutrons depending on the moderator (The reactor and the neutron sources 2003).

For cold neutrons but also sometimes for hot neutrons (e.g. SPODI at FRM2, Garching bei Munchen), the neutrons are guided towards the instrument following the optical principle of total reflection for which, under a certain incident angle θ_c, the neutron wave will not be able to go through the reflective medium and will be totally reflected. Neutron guides offer the possibility to further tune the neutron flux by creating constructive interference between the reflected waves or by cutting the flux of neutrons possessing a wavelength inferior to the cut-off wavelength λ_c (The reactor and the neutron sources 2003).

1.2.1 Neutrons as a probe

Neutrons have some unique properties that allow us to probe matter. If we consider the previously calculated wavelength and energy, we can see the energy of neutrons is not only tune-able but also in the range of different dynamic phenomena in solids or fluids, perfect for the study of structures at the atomic scale or for dynamic analysis, when neutrons will be inelastically scattered by a phonon for example, the phonon energy can be directly extracted from the energy of the phonons providing insight into the atomic forces at play.

Neutrons are neutral, non-destructive, making them the perfect probe for the study of membranes or proteins. Due to their absence of electrical charge, they can penetrate deeply inside materials, possessing a low absorption coefficient with regards to most elements, making it possible to study bulk materials or materials that would be too

absorbent for X-Ray. Since neutrons interact with matter via the strong nuclear force, their interaction with matter is different than how X-Rays interacts with matter. Thus, they can be sensitive to elements that are invisible to X-Ray, e.g. Hydrogen.

Neutrons possess spins and magnetic moments and also interact with the unpaired electrons in magnetic atoms. Neutrons are therefore sensitive to magnetic structures and neutron scattering can yield information such as the density distribution of unpaired electrons.

Activation and low flux are the main drawbacks of neutrons. It can be complicated to work with some metals that could activate (Cobalt for example).

Neutrons cross-sections

Let us consider a monochromatic beam of neutrons, of energy E, scattering from a sample that could be solid, crystalline or liquid (figure 1.6). We count the amount of neutrons scattered by the sample with a detector in the directions (θ, ϕ), the detector is assumed to be far from the sample. We define Φ as the flux of incident neutrons, i.e. the amount of neutrons per unit area per second, the area is perpendicular to the direction θ, ϕ of the neutron beam. The result of the measurement of neutrons that have interacted with the scattering system can be translated via three different cross-section, cross-sections are given in barn units (1 barn = 10^{-24} cm^2).

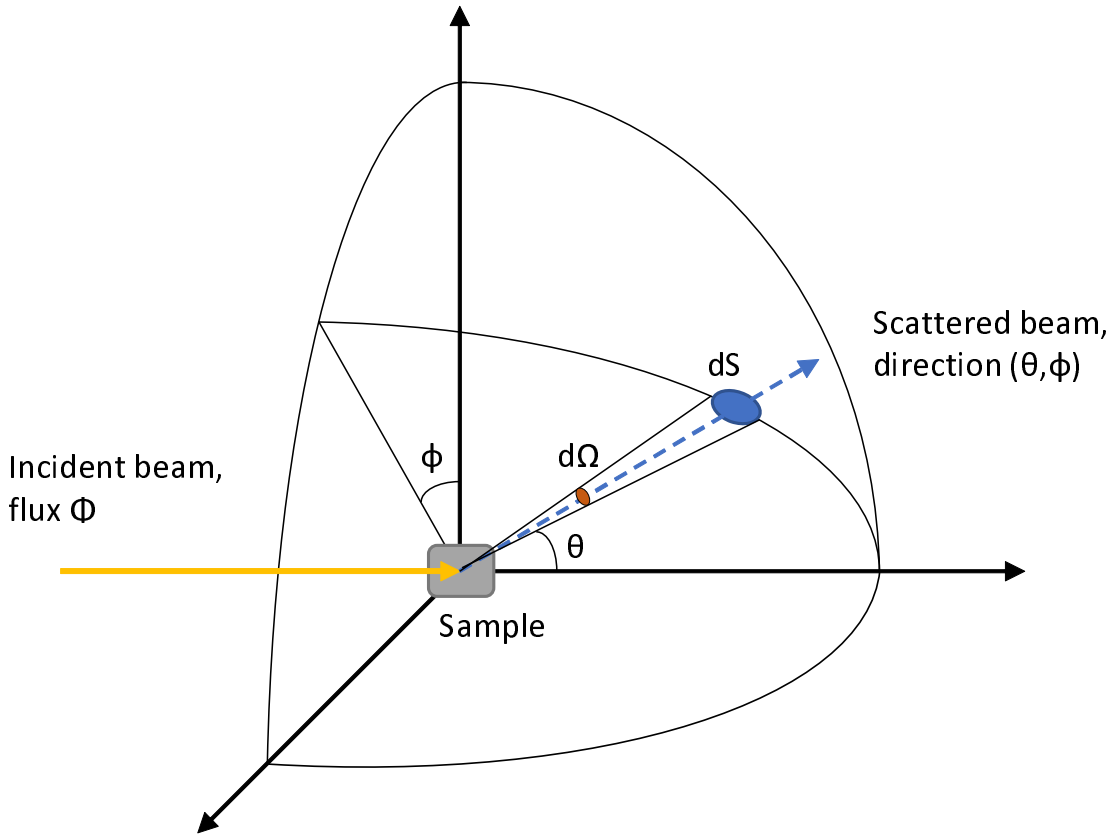

Figure 1.6: Geometry of a scattering experiment, in polar coordinates.

The *differential cross-section* defined as:

$$\frac{d\sigma}{d\Omega} = (\text{number of neutrons scattered per second into d}\Omega \text{ in the direction } \theta, \phi)/\Phi \, d\Omega \tag{1.8}$$

The *double differential cross-section*, defined as:

$$\frac{d^2\sigma}{d\Omega dE'} = \begin{array}{l}\text{(number of neutrons scattered per second into a small solid}\\ \text{angle d}\Omega \text{ in the direction } \theta, \phi \text{ with their final energy between}\\ E' \text{ and } E' + dE') \ / \ \Phi \, d\Omega \, dE'\end{array} \tag{1.9}$$

The *total scattering cross-section* defined as:

$$\sigma_{tot} = \begin{array}{l}\text{(total number of neutrons scattered in all directions per}\\ \text{second)}/\Phi.\end{array} \tag{1.10}$$

If one follows the logic behind the definitions of the cross-sections, one can derive the following equations :

$$\frac{d\sigma}{d\Omega} = \int_{-\infty}^{\infty} \left(\frac{d^2\sigma}{d\Omega dE'}\right) dE', \tag{1.11}$$

$$\sigma_{tot} = \int_{all\ directions} \left(\frac{d\sigma}{d\Omega}\right) d\Omega \tag{1.12}$$

The cross-sections are the physical quantities that are directly measured from the experiment, that consist in counting the neutrons received per counting time in a direction that is defined by the characteristics of the instrument and that can be chosen by the user. If the differential cross section (1.8) depends only on an angle θ, one can write :

$$\sigma_{tot} = \int_0^{\pi} \frac{d\sigma}{d\Omega} 2\pi \sin\theta d\theta \tag{1.13}$$

The experimental cross-section defined as above are valid for a single atom and do not take account of the initial and final spin states of the neutron. It is now to the scientist to link the output of the experience to the physical theories behind neutron scattering.

1.2.2 Neutron scattering

Let us first consider a simple approach to neutron scattering with a system consisting of a single nucleus, one can write the nucleus-neutrons interaction potential for a single nucleus as $V(\vec{r})$.

We can then derive the Schrödinger equation as follows:

$$\left[\frac{-p^2}{2m} + V(r)\right]\psi(r) = E\psi \tag{1.14}$$

where the first term corresponds to the kinetic energy and the second to the potential energy, i.e. the nucleus-neutrons potential $V(\vec{r})$. $\psi(r)$ is the eigenfunction of the neutron. The general solution to the Schrodinger equation is given in the Born Approximation (DWBA).The incoming wave is assumed plane:

$$\phi_i(r, w) = \exp\left(-i(kx - \omega t)\right) \tag{1.15}$$

and the resulting wave is the sum of a plane wave and a spherical wave. The final particle scatters in all directions in the form of a spherical wave.

$$\phi_f(r,w) = \exp\left(-i(kx-\omega t)\right) + f(\theta)\frac{\exp\left(-i(kx-\omega t)\right)}{r} \tag{1.16}$$

The interaction potential is called the Fermi pseudo-potential given by Fermi to quantify the bond between a nucleus and a neutron (Squires 1997):

$$V(r) = \frac{2\pi\hbar^2}{m} b\delta(r) \tag{1.17}$$

$f(\theta)$ is the scattering amplitude and depends directly on the momentum transfer q. It is defined as the Fourier transformation of the interaction potential V. One can see that repulsive potentials result in positive scattering lengths.

$$f(\theta) = \frac{m_n}{2\pi\hbar^2}\int d\vec{r'} \exp -i(\vec{Q}\vec{r'})V(\vec{r'}) = -b \tag{1.18}$$

The scattering length b has been determined experimentally for each element and can be found on the National Institute of Standards and Technology (NIST) website ("Neutron News" 1992) and quantifies the scattering power of each element. Its values depend directly on the spin state on the nucleus and on the isotopes. In contrast with the scattering factor for X-Ray, the scattering length of neutrons does not behave proportionally to Z but observes an unpredictable behavior.

It is interesting to know that the scattering length can be complex and that its value can depend on the energy of the neutron. The imaginary part of the scattering length quantifies absorption and for some elements with important imaginary scattering length, the scattering of a neutron lead to the formation of a compound nucleus with an energy close to the energy of an excited state. However we are mainly concerned with elements whose scattering length is almost purely real and independent of the neutron's energy.

Following figure 1.6, the scattering energy is distributed over the surface of a sphere of area $4\pi r^2$.

We must then neglect the following points: absorption, primary and secondary attenuation of the beam due to multiple scattering.

For the scattering of a neutron of velocity v from a single nucleus, the number of neutrons scattered from the sample that go through an area dS as defined in the figure 1.6 from (1.16):

$$v dS|\psi_f|^2 = v dS\frac{b^2}{r^2} = v b^2 d\Omega \tag{1.19}$$

Likewise, from (1.15), we have the flux of incoming neutrons:

$$\Phi = v|\psi_i|^2 = v \tag{1.20}$$

And from the definition of the final cross-section (1.10) we have :

$$\frac{d\sigma}{d\Omega} = \frac{v b^2 d\Omega}{\Phi d\Omega} = b^2 \tag{1.21}$$

Finally, from (1.13), integrating over the angle θ gives:

$$\sigma_{tot} = 4\pi b^2 \tag{1.22}$$

To resume :

$$\sigma_{tot} = \int \sigma_s = \int_0^{4\pi} \frac{\partial\sigma}{\partial\Omega}\partial\Omega = 4\pi b^2 \tag{1.23}$$

Simple approach to coherent and incoherent scattering

Let us consider a system that is constituted of one element with N nuclei, each nucleus has a scattering length b, because of isotopes and/or nuclear spins, b varies randomly from one nucleus to another. We have a system with i different values b_i that each occur f_i times, so that the average scattering length of the system is:

$$\bar{b} = \sum_i f_i b_i \tag{1.24}$$

and the average square of the scattering length is:

$$\bar{b^2} = \sum_i f_i b_i^2 \tag{1.25}$$

We assume that our system is one of many systems that share the same amount of total b_i, as well as the same positions and momentum of the nuclei. The only difference between these systems is the distribution of the b values, meaning that if nucleus j has the value b_i in one system, he will have the value $b_{i'}$ in another system. Now, if we have a very large number of nuclei, we can assume that the scattering length component of the cross-section:

$$\sum_{ii'} b_{i'} b_i \tag{1.26}$$

is equal to the average over all the systems:

$$\sum_{ii'} \overline{b_{i'} b_i} \tag{1.27}$$

Assuming that there are no correlation between any values of b_i, one can write:

$$\overline{b_{i'} b_i} = (\bar{b})^2, \quad j' \neq j, \tag{1.28}$$

$$\overline{b_{i'} b_i} = \bar{b^2}, \quad j' = j, \tag{1.29}$$

Without going into the details of the differential cross-section, one can develop for the scattering length:

$$\sum_{ii'} \overline{b_{i'} b_i} \;=\; \sum_{\substack{ii' \\ i\neq i'}} (\bar{b})^2 + \sum_i \bar{b^2} \;=\; \sum_{ii'} (\bar{b})^2 + \sum_i (\bar{b^2} - (\bar{b})^2) \tag{1.30}$$

Thereby defining the coherent and incoherent scattering cross-section:

$$\sigma_{coh} = 4\pi(\bar{b})^2, \qquad \sigma_{inc} = 4\pi(\bar{b^2} - (\bar{b})^2) \tag{1.31}$$

From the equations above, we can see that coherent scattering gives rise to interference due to correlations between the same nucleus (i=i') and between different nuclei (i=i') . It allows us to access the relative position of these atoms. Furthermore, we have information on packets of atoms, dispersion relation of phonons or Bragg reflections.

Incoherent scattering is characterized by the absence of interference. There is no relation between different atoms in the scattered waves; we track the self-motion or self-dynamic of an atom.

Bragg's Law

In the frame of this thesis, where the all the information will be extracted from the analysis of Bragg peaks, it is mandatory to explain the physics behind Bragg peaks.

The lattice of our crystal is defined by three vectors $\vec{a}$, $\vec{b}$, $\vec{c}$. Any vector $\vec{v}$ of the unit cell can then be created by a linear combination of these three vectors:

$$\vec{v} = n_1\vec{a} + n_2\vec{b} + n_3\vec{c}, \quad with\ (n_1, n_2, n_3) \in \mathbb{Z}^3 \tag{1.32}$$

the volume of the unit cell is:

$$V = \vec{a}.(\vec{b} \times \vec{c}) \tag{1.33}$$

An important tool of crystallography is the *reciprocal space* of dimension m^{-1}, defined by the three vectors $\vec{a*}$, $\vec{b*}$, $\vec{c*}$:

$$\vec{a^*} = \frac{2\pi}{V}(\vec{b} \times \vec{c}), \qquad \vec{b^*} = \frac{2\pi}{V}(\vec{c} \times \vec{a}), \qquad \vec{c^*} = \frac{2\pi}{V}(\vec{a} \times \vec{b}) \tag{1.34}$$

From the De Broglie wavelength (1.5), it is possible to define the wavevector k of neutrons (1.7). We can then define the momentum transfer $\vec{Q}$ as the difference between the wavevector of the incoming neutron $\vec{k}$ and the wavevector of the scattered neutron $\vec{k'}$:

$$\vec{Q} = \vec{k} - \vec{k'} \tag{1.35}$$

The figure 1.7 leads to (1.36) and illustrates the particular case of a Bragg peak. If the momentum transfer $\vec{Q}$ can be expressed as a linear combination of reciprocal vectors, here graphically verified, a Bragg peak occurs for this value of Q.

$$\vec{Q_{hkl}} = 2k\sin\theta = \frac{4\pi}{\lambda}\sin\theta \tag{1.36}$$

$\vec{Q}$ can be written as a linear combination of the reciprocal length between planes.

$$\vec{Q} = n\frac{2\pi}{d_{hkl}}, \qquad with\ n \in \mathbb{Z} \tag{1.37}$$

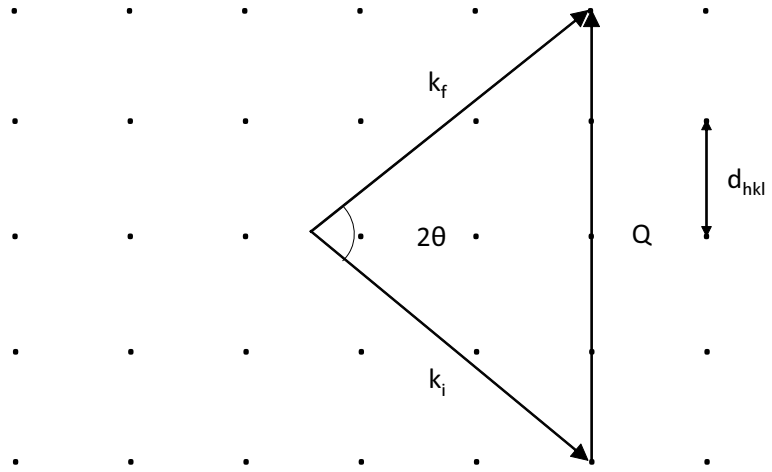

Figure 1.7: Geometry of the momentum transfer $\vec{Q}$ in reciprocal space, 2θ is the scattering angle.

Combining (1.36) and (1.37), we fall back on the most famous equation of crystallography, Bragg law:

$$n\lambda = 2d_{hkl}\sin\theta \tag{1.38}$$

To summarize, a Bragg peak result from the constructive interference between coherently scattered waves at discrete values of the incident angle 2θ or of the momentum transfer $\vec{Q}$ on a specific set of crystalline planes. $\vec{Q}$ and 2θ are linked through (1.36). The condition to have constructive interference is known as Bragg law and is given by (1.38).

From (1.37), one can define the general reciprocal-space metric tensor for any crystalline system:

$$\frac{(2\pi)^2}{d_{hkl}^2} = h^2\,(\vec{a^*}.\vec{a^*}) + k^2\,(\vec{b^*}.\vec{b^*}) + l^2\,(\vec{c^*}.\vec{c^*}) + 2hk\,(\vec{a^*}.\vec{b^*}) + 2hl\,(\vec{a^*}.\vec{c^*}) + 2kl\,(\vec{b^*}.\vec{c^*}) \tag{1.39}$$

$$\frac{(2\pi)^2}{d_{hkl}^2} = h^2\,a^{*2} + k^2\,b^{*2} + l^2\,c^{*2} + 2hk\,a^*.b^*\cos\gamma^* + 2hl\,a^*.c^*\cos\beta^* + 2kl\,b^*.c^*\cos\alpha^* \tag{1.40}$$

$$\frac{(2\pi)^2}{d_{hkl}^2} = Ah^2 + Bk^2 + Cl^2 + Dhk + Ehl + Fkl \tag{1.41}$$

Equation (1.39) can be simplified as (1.42) for a simple cubic system, defining the interplanar spacing between the crystalline planes:

$$d_{hkl} = \frac{2\pi}{|\vec{a^*}|\sqrt{h^2+k^2+l^2}} = \frac{|\vec{a}|}{\sqrt{h^2+k^2+l^2}} \tag{1.42}$$

Moreover, for each peak, indexed by its *hkl* miller indices that specify the orientation of the crystalline planes, the momentum transfer can be written as a linear combination of reciprocal space vectors, for a cubic lattice:

$$\vec{Q_{hkl}} = h\vec{a*} + l\vec{b*} + k\vec{c*} \tag{1.43}$$

Inelastic scattering

One can also write for the momentum transfer:

$$\omega = \frac{\hbar k_f^2}{2m} - \frac{\hbar k_i^2}{2m} \tag{1.44}$$

We have elastic scattering if $|\vec{Q}| = 0$, energy is not transferred (to or from the material) in this case, we lose all dynamical information about the sample and study the structural information alone.

For inelastic scattering, when $|\vec{Q}| \neq 0$, energy is transferred, given or received from the sample. In that case we measure neutrons as a function of both energy and momentum transfer. It can lead to a dispersion relation giving more insight in the geometry of the phenomena that lead to the loss or gain of energy.

1.2.3 Intensity of a nuclear Bragg peak

Neglecting absorption, very weak for most of the elements, and considering only a non-magnetic structure factor; the intensity of a Bragg peak I_{nuc} as a function of its miller indices *hkl* and of 2θ can be written as:

$$I_{nuc} = A \times |F_{hkl}|^2 \times j_{hkl} \times L(2\theta) \times \exp(-2W) \tag{1.45}$$

where A is an instrument constant.

Structure factor

F_{hkl} is known as the structure factor, it is given by:

$$F_{hkl} = \sum_{j=0}^{n} b_j \exp(-2\pi i \vec{Q}.\vec{r_{j0}}) \tag{1.46}$$

The structure factor is the summation of the contribution to the scattering energy of each atoms at the position $\vec{r_{j0}}$ of scattering length b_j in our unit cell for a given $\vec{Q}$. The position of the atom $\vec{r_{j0}}$ is given by:

$$\vec{r_{j0}} = x_j\vec{a} + y_j\vec{b} + z_j\vec{c} \tag{1.47}$$

Debye-Waller factor

The position $\vec{r_j}$ of the atom j is not static but should be rather understood as the instantaneous position of the atom. In a crystal, atoms vibrate around their equilibrium position $\vec{r_{j0}}$, we have:

$$\vec{r_j}(t) = \vec{r_{j0}} + \vec{u}(t) \tag{1.48}$$

$\vec{u} = \vec{u}(t)$ is the thermal displacement, accounting for thermal vibrations in the crystal. These oscillations around the equilibrium position can be understood following the model of a harmonic oscillator at low temperature, with discrete frequencies of vibrations. The frequency of the vibrations, that increase with temperature, are linked to quasi-particles named *phonons*. Another contribution to the thermal displacement is the zero-point displacement, if one could lower the temperature of the crystal in a perfect vacuum down to absolute zero, one would have expected the system to not show any motion. However, quantum physics tells us that even at absolute zero there is a probability for the atom to not be in at its equilibrium position, called zero-point displacement. Moreover, the Debye-Waller factor also takes into account the static displacement in the lattice that is linked to disorder. This will be discusses further in chapter 2.

The exponential in (1.46) can be rewritten as:

$$\exp\left(-2\pi i\vec{Q}.\vec{r_j}\right) = \exp\left(\ -2\pi i\vec{Q}.(\vec{r_{j0}} + \vec{u})\ \right) \tag{1.49}$$

The average of this equation is given by:

$$\langle \exp\left(-2\pi i\vec{Q}.\vec{r_j}\right)\rangle = \exp\left(-2\pi i\vec{Q}.\vec{r_{j0}}\right) \times \langle \exp\left(\ -2\pi i\vec{Q}.\vec{u}\right)\ \rangle \tag{1.50}$$

The second term of this expression can be expanded as the second order Taylor series for $\exp x_0$ with $x_0 = -2\pi i\vec{Q}.\vec{u}$ at zero, we loose the (2π) for clarity:

$$\langle \exp\left(-i\vec{Q}.\vec{u}\right)\rangle = 1 - \langle\ i\vec{Q}.\vec{u}\ \rangle - \frac{1}{2}\langle\ (\vec{Q}.\vec{u})^2\ \rangle + o\ (\ \langle\ (\vec{Q}.\vec{u})^2\ \rangle\ ) \tag{1.51}$$

Since the displacement are random, the average of $i\vec{Q}.\vec{u}$ is equal to zero. However the average of the square of $\vec{Q}.\vec{u}$ is non zero and can be further developed as:

$$\langle\ (\vec{Q}.\vec{u})^2\ \rangle = Q^2\ \langle\ u^2\ \rangle\ \langle\ \cos\theta^2\ \rangle = \frac{1}{3}\ Q^2\ \langle\ u^2\ \rangle \tag{1.52}$$

which leads to:

$$\langle \exp\left(-i\vec{Q}.\vec{u}\right)\rangle = 1 - \frac{1}{6}\ Q^2\ \langle\ u^2\ \rangle \tag{1.53}$$

that corresponds to the first order Taylor series for $\exp x_0$ with $x_0 = \frac{1}{6}\ q^2\ \langle\ u^2\ \rangle$ at zero, we can write:

$$1 - \frac{1}{6}\ Q^2\ \langle\ u^2\ \rangle = \exp\left(\frac{1}{6}\ Q^2\ \langle\ u^2\ \rangle\ \right) \tag{1.54}$$

The final intensity contribution of the Debye Waller factor is the square of (1.54) given by:

$$\exp\left(\frac{1}{3}\ Q^2\ \langle\ u^2\ \rangle\ \right) \tag{1.55}$$

The last two terms of (1.45), respectively j_{hkl} and $L(2\theta)$ are the multiplicity of a Bragg peak and the Lorentz factor. They will be studied in a section covering the

instrument used for powder diffraction for they both relate more to the collection of the data than to the theoretical intensity of a Bragg peak.

1.3 Magnetic neutron scattering

A bit of the standard model

The nucleons, i.e. the proton and the neutron are hadrons, composite particles that are not elementary particles unlike the electron or the photon. More specifically, the nucleons are baryons, hadrons composed of three quarks. The neutron is formed by 2 quarks down and one up quark and its final properties can be assumed to be approximately the properties of its quarks. The charge of the up quark is $\frac{2}{3}$ and the charge of the down quark is $-\frac{1}{3}$. The summation of these charges for the neutron is zero and is the reason behind its name.

The force that is responsible for the cohesion of the nucleons is the strong interaction force whose gauge boson is the gluon. Its range is of the fentometer, the size of an atomic radius. Therefore, the strong interaction affects only the nucleus and confines it together, being 137 times more important than the electromagnetic force on this scale. The mass of the neutron is mostly due to the energy of the gluons.

The spin of both quarks is $\frac{1}{2}\hbar$ resulting in a half-integer $\frac{1}{2}\hbar$ spin for nucleons that classifies them as fermions, obeying the Fermi-Dirac statistics. The Fermi-Dirac statistics gives the distribution of the number of particles over the energy states in a system in thermodynamic equilibrium. A famous result of this rule is the Pauli exclusion principle that states that two fermions cannot occupy the same energy state (first written for electrons by Pauli in 1925 then extended to all the fermions).

The spin of a neutron is represented by a vector whose norm can take two values, $+\frac{1}{2}\hbar$ called spin up and $-\frac{1}{2}\hbar$ called spin down. It is a purely quantum concept, commonly understood as an intrinsic angular momentum and associated to a spin magnetic moment.

1.3.1 Magnetic moments

The magnetic moment of the neutron

The interaction of the neutron with matter is not only due to the nuclear force giving rise to nuclear neutron scattering (1.45), magnetic neutron scattering originates from the interaction between the neutron's spin with the magnetic moment of the unpaired electrons in the sample, which can have an orbital contribution and/or a spin contribution.

For a particle of charge q, mass m and spin angular momentum $\vec{S}$, the spin magnetic moment is given by:

$$\vec{\mu_n} = g\frac{q}{2m}\vec{S} = \gamma\vec{S} \tag{1.56}$$

where γ is the gyromagnetic ratio, ratio between the observed frequency of the Larmor precession of a neutron under an external magnetic field and the strength of the magnetic field, it is also the ratio between the spin and the magnetic moment.g is the g-factor, dimensionless, that depends on the particle.

For neutrons, that have a zero charge, the magnetic moment results from the quarks and is given by $g = -3.826$. One can also write:

$$\vec{\mu_n} = \frac{g\mu_N}{\hbar}\vec{S} = \pm\frac{g}{2}\mu_N = \pm -1.913\mu_N \tag{1.57}$$

where μ_N is the nuclear magneton:

$$\vec{\mu_n} = \frac{e\hbar}{2m_p} \tag{1.58}$$

The magnetic moment of the electron

We define a total angular momentum $\vec{J}$ for the electron, due to two different types of rotation. The intrinsic spin angular momentum $\vec{S}$ is seen as a contribution from the rotation of the electron around its own axis that was first deduced from experimental results. The orbital angular momentum $\vec{L}$ results from the cross product of the quantum position operator $\vec{r}$ and quantum momentum operator $\vec{p}$ for and electron in motion in its orbital, we have :

$$\vec{L} = \vec{r} \times \vec{p} = \hbar\sqrt{l(l+1)}, \tag{1.59}$$
$$\vec{S} = \hbar\sqrt{s(s+1)}, \tag{1.60}$$
$$\vec{J} = \hbar\sqrt{j(j+1)} \tag{1.61}$$

with the spin quantum number $\vec{s}$ and azimuthal quantum number $\vec{l}$.

As seen in classical mechanics, a rotating charge creates a magnetic dipole. The different angular momentum of the electron give rise to spin magnetic moment and an orbital magnetic moment. The magnetic moment of the electron can then be defined similarly to (1.56):

$$\vec{\mu_L} = -g_L\frac{e}{2m_e}\vec{L} = \gamma\vec{L}, \tag{1.62}$$
$$\vec{\mu_S} = -g_S\frac{e}{2m_e}\vec{S} = \gamma\vec{S}, \tag{1.63}$$
$$\vec{\mu_J} = -g_J\frac{e}{2m_e}\vec{J} = \gamma\vec{J} \tag{1.64}$$

or in terms of the Bohr magneton $\mu_B = \frac{e\hbar}{2m_e}$, with $g_L = 1$, $g_s = 2.0023 \approx 2$ and g_J the Landé factor:

$$\vec{\mu_L} = -\mu_B\sqrt{l(l+1)}, \tag{1.65}$$
$$\vec{\mu_S} = -2\mu_B\sqrt{s(s+1)}, \tag{1.66}$$
$$\vec{\mu_j} = -g_J\mu_B\sqrt{j(j+1)} \tag{1.67}$$

1.3.2 Magnetism in 3d transition metals and Heusler alloys

In our NiMnSb system, the magnetic moments is mostly on the Mn sites and also slightly on the Ni sites (J Brown et al. 2010). The magnetic moment of each ion can be first understood by discussing the formation of ions for transition metals. The Mn^{2+} ions have a tendency to form octahedral complexes in which the energy of the orbitals are no longer degenerate but split into two sub-orbitals resulting from the interactions between the ligand field and the orbitals of the metal center. The direct contact between the ligand field and the $d_{x^2-y^2}$ and d_{z^2} orbitals leads to electron-electron repulsion and results in these orbitals, forming the e_g subset, having higher energy. The lower t_{2g} subset is then constituted by the d_{xy}, d_{xz}, d_{yz} orbitals that suffer less electron-electron repulsion. The energy of the crystal is split by a value Δ between two energy sub-levels: t_{2g} and e_g. These orbitals are not spherically symmetric Moreover, we talk about high-spin/low-spin depending on the strength of the ligand field. Low spin occurs for a strong Δ, the electrons will first occupy the lower energy t_{2g} orbitals, with a minimal amount of unpaired electrons. At high spin, the splitting energy is weak and the system follows the behaviour of a degenerated free ion.

The contribution to the magnetic moments from orbital angular and spin momentum can be written as the following with S the spin quantum number, $\frac{1}{2}$ for each unpaired electron:

$$\mu_{S+L} = \sqrt{4S(S+1) + L(L+1)} \tag{1.68}$$

For high-spin Mn^{2+} with an electronic configuration $[Ar]4s^0 3d^5$, the t_{2g} sub-level is filled first, with 3 electrons followed by the 2 electrons on the e_g, giving a configuration: $t_{2g}^3 e_g^2$.

For electrons to have an orbital angular momentum contribution to magnetism, its orbital must be able to transform into an exactly identical orbital of the same energy by a simple rotation since the magnetic moment is directly linked to the angular momentum by (1.62).

In an octahedral complex, we should have a triply degenerated ground term, i.e. a T state or precisely the t_{2g} set of orbitals (d_{xz}, d_{yx}, d_{yz}) that can be interconverted by a 90° rotation. However, since the orbital shape in the e_g subset are different, it is impossible to convert by rotation an electron from one state to the other. Hence, an electron in the e_g subset set does not contribute to the orbital angular momentum and is said to be quenched. In the free ion case the electrons can be transformed between any of the orbitals as they are all degenerate, but there will still be partial orbital quenching as the orbitals are not identical. Moreover, electrons in the T set do not contribute to the orbital angular moment in special cases. In the case of Mn^{2+}, we have a t_{2g} sub-shell filled with 3 electrons, an electron in the d_{xy} orbital cannot by rotation be placed in the d_{yz} orbital as the orbital already has an electron of the same spin. This process is also called quenching.

To resume, in Mn^{2+}, we only have a spin contribution to the magnetic moment due crystal splitting induced by the octahedral formation of manganese. This moment is easily computer by simplifying (1.68), taken for L=0 and S=$\frac{5}{2}$ as a prefactor of the Bohr Magneton:

$$\mu_{S,Mn^{2+}} = \sqrt{4S(S+1)} = \sqrt{35} = 5.92\mu_B \tag{1.69}$$

For Ni^{2+}, we have the electronic configuration $[Ar]4s^0 3d^8$, or t^6e^2 since Ni occupies the tetrahedral holes of the system and a spin-only magnetic moment due to a quenched t subset:

$$\mu_{S,Ni^{2+}} = \sqrt{4S(S+1)} = \sqrt{8} = 2.83\mu_B \tag{1.70}$$

When it comes to Heusler alloys of the family Ni−2MnSb, magnetism is primarily understood via the Bethe-Slater curve (Lázpita et al. 2011; Cardias et al. 2017) that describes the difference in exchange energy in transition metals as a function of the overlap between the d orbitals. One can understand the interactions of the transition metals by a Heisenberg Hamiltonian model (1.71) (Baxter 1982) where J_{ij} is the exchange interaction between two Mn sites and s_i the unit vector pointing in the direction of the magnetic moment at a site i (I. Galanakis and Şaşıoğlu 2011). In the case of small overlaps of the d orbitals, ferromagnetic interactions tend to result whereas in the case of large overlaps, anti-ferromagnetic ones will result. For very large overlaps, the d orbitals will delocalize and a nonmagnet will result. Mn as an elementary system is antiferromagnetic. However, in the well-ordered $L2_1$ structure, the distance between two Mn is so large that they barely link directly. It is the interaction with the adjacent Ni atoms that leads to an effective ferromagnetic interaction between the Mn spins. But if a Mn sits on Z then there is a fairly strong antiferromagnetic interaction between this Mn and the regular Mn neighbors on Y. This direct antiferromagnetic interaction opposes the indirect ferromagnetic so that the effective couplings are weaker, and hence the magnetic transition temperatures lowers.

$$H_{eff} = -\sum_{i \neq j} J_{ij} s_i s_j \tag{1.71}$$

1.3.3 Intensity of a magnetic Bragg peak

Magnetic form factor

A simple approach to the magnetic form factor is to understand it in a similar way to the atomic form factors for X-Ray scattering. The scatterer are however not all the electrons but only the unpaired electrons that contribute to magnetism. In the dipole approximation (small q), for a unique magnetization direction, it is written as the Fourier transform of the magnetization distribution for a single atom (Brown 2003).

$$M \int m(r) e^{iq.r} dr = M f(q) \tag{1.72}$$

M is the vector form factor and gives the magnitude and direction of the moment, m(r) is normalized over the volume of the atom and gives the value of the magnetization at a point designed by r. In our case, the magnetization arises from electrons in a single open d shell, the magnetic form factor can be calculated from the radial distribution of the electrons in that shell.

In the dipole approximation, we can write the magnetic form factor as the following with $\langle j_0(s) \rangle$ and $\langle j_2(s) \rangle$ functions of q, describing the radial distribution of spin and of current densities:

$$f(q) = 2S\ \langle j_0(q)\rangle\ +\ L\ \left(\langle j_0(q)\rangle\ +\ \langle j_2(q)\rangle\right) \tag{1.73}$$

For 3d electrons in ions, an analytic approximation of $\langle j_0(s)\rangle$ and $\langle j_0(s)\rangle$ integrals is given by Brown (2003):

$$\langle j_0(s)\rangle = A\ \exp(-as^2) + B\ \exp(-bs^2) + C\ \exp(-cs^2) + D, \tag{1.74}$$

$$\langle j_2(s)\rangle = \left(A\ \exp(-as^2) + B\ \exp(-bs^2) + C\ \exp(-cs^2) + D\right)\ s^2, \tag{1.75}$$

$$with \quad s = \frac{q}{4\pi} = \frac{\sin q}{\lambda}\ in\ \text{Å} \tag{1.76}$$

The coefficient have been determined and are given on the ILL website. A detailed model for our system has been given by G. E. Bacon and Plant (1971) in which the magnetization distribution is given by the sum of the atomic magnetization over the magnetic atoms:

$$f_i(q) = \mu_i[\langle j_0(q)\rangle_i b_i \langle j_2(q)\rangle_i + a_i A(q)\langle j_4(q)\rangle_i] \tag{1.77}$$

where $\langle j_0(q)\rangle_i$, $\langle j_2(q)\rangle_i$ and $\langle j_4(q)\rangle_i$ are the free atom form factors for i = Ni or Mn, μ_i is the magnetic moment associated with the atom i and b_i the fraction of the moment due to orbital motion in the dipole approximation. The g-factor $g_i = 2/(1 + b_i)$. The coefficient a_i measures the deviation of the distribution from spherical symmetry, we have $\gamma = \frac{5}{2}(a_i + 1)$, the fraction of magnetic electrons in the e_g orbitals. Finally :

$$A(hkl) = \frac{(h^4 + k^4 + l^4) - 3(h^2k^2 + k^2l^2 + l^2h^2)}{(h^2 + k^2 + l^2)^2} \tag{1.78}$$

It was found in the same work that the contribution of orbital motion to the magnetic moment of Mn in NiMnSb was very small and that the moment on Ni is too small to determine an orbital content. Therefore, in the frame of this thesis, it is sufficient to have a simpler approach in which we assume the orbital moment to be quenched due to the energy of the crystal field, we consider spin-only scattering:

$$f(q) = 2S\ \langle j_0(q)\rangle, \tag{1.79}$$

$$with \quad S = \frac{1}{2} \tag{1.80}$$

The variation of $f(q)^2$ as a function of the momentum transfer q are given by (1.8).

Comparison with nuclear neutron scattering

To resume, the neutron is a spin $\frac{1}{2}$ particle that carries a magnetic dipole moment of 1.913 nuclear magnetons. Magnetic neutron scattering originates from the interaction between the neutron's spin and the unpaired electrons in the sample (the interaction between the neutron's spin and the nucleus' spin is neglected). We have two contribution to the sample's unpaired electrons' magnetic dipole: the intrinsic spin dipole

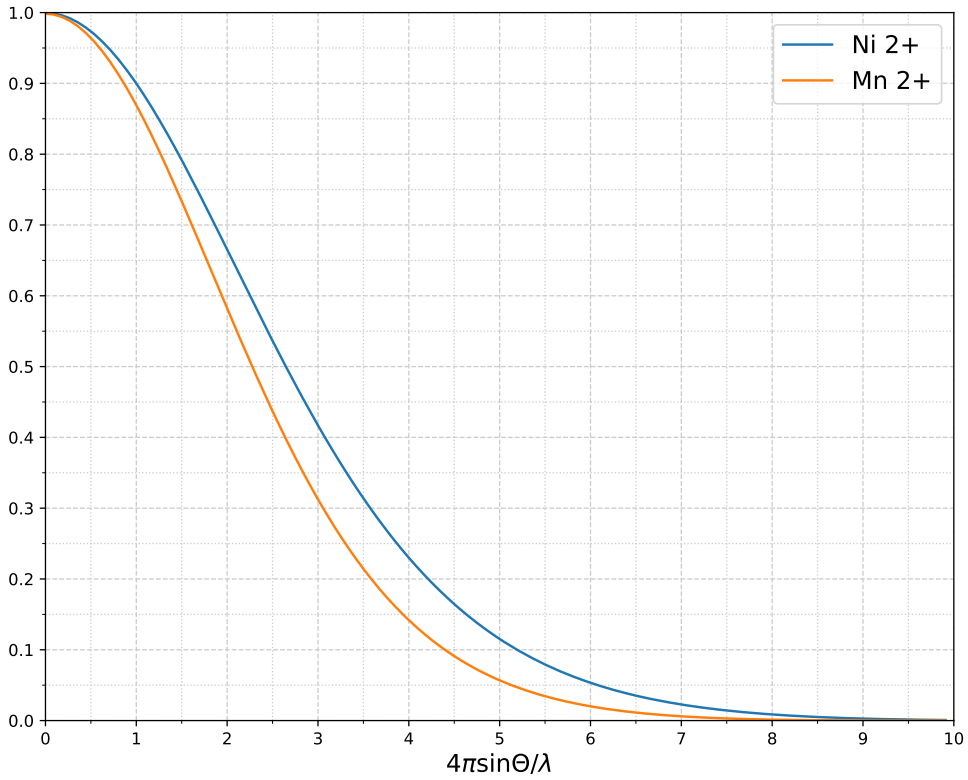

Figure 1.8: The squared magnetic form factor for Mn^{2+} and Ni^{2+} in the dipole approximation.

moment and the orbital magnetic dipole of the electron. The strength of this magnetic dipole–dipole interaction is comparable to the neutron–nuclear interaction which allows us to see the effect of magnetism with the same neutrons that are used to study the structure and dynamics of materials by having both a nuclear cross-section and a magnetic cross-sections (for magnetic atoms only).

To continue the analogy, the intensity of a magnetic peak must also be corrected for the Debye-Waller factor, the Lorentz factor and, for powder diffraction, the multiplicity of the peak. The intensity of a magnetic Bragg peak I_{mag} for a momentum transfer q is given by G. Bacon (1975):

$$I_{mag}(q) = A\left(\frac{\gamma e^2}{2mc^2}\right)^2 |F_{mag}(q)|^2 \times j_{hkl} \times L(2\theta) \times \exp\left(-2W\right) \tag{1.81}$$

where A is the same instrument constant as in (1.45), contributing to both the nuclear and the magnetic intensity of a Bragg peak. The value between the parenthesis is the electron neutron coupling constant equal to -0.27×10^{12}cm (Lynn 2012). The magnetic structure factor $|F_{mag}(q)|^2$ is generally given by:

$$F_{mag}(q) = \sum_{j=1}^{N} \eta_j e^{iq.r_j} \hat{q} \times \big[M_j(q) \times \hat{q}\big], \tag{1.82}$$

$$with\ \hat{q} = \frac{\vec{q}}{|\vec{q}|} \tag{1.83}$$

$M_j(q)$ is the vector form factor of the jth ion located at the position r_j in the unit cell. We have a triple cross-product due to the vector nature of the dipole–dipole interaction between the unpaired electron and the neutrons.

Often, the atomic spin density is collinear, for each point in the electron's probability distribution, the direction of the atomic magnetization density is the same. In this case, the direction of the vector form factor does not depend on q, and the form factor is written with f(q), Fourier transform of the magnetization density as seen before in (1.72). If one was to compare (1.8) with the dependence of the atomic form factor for X-Ray, one would notice that the magnetic form factor decreases faster than the atomic form factor, this is due to the unpaired electrons being further from the atom than the other electrons. Hence, the neutron magnetic intensity of a magnetic Bragg peak is only noticeable at low q, whereas the neutron nuclear intensity is constant with q (the scattering length not depending on q). In our system the magnetic structure is collinear, the moments in the ordered state pointing along a unique direction $\hat{\eta}$ in the structure, we consider that the magnetic moments are only from Mn^{2+} with $\mu_{Mn^{2+}}$ the average value of the moment in the thermodynamical equilibrium, we can write:

$$|F_{mag}(q)|^2 = \langle\ 1 - (\vec{q}.\vec{\eta})^2\ \rangle \langle \mu_{Mn^{2+}} \rangle^2 f^2_{Mn^{2+}}(q) \left| \sum_{j=1}^{N} \eta_j e^{iq.r_j} \right|^2 \tag{1.84}$$

the sum is over all the magnetic atoms in the unit cell (here Mn^{2+}), η_j quantifies the sign of the magnetic moment of the atom j (± 1). In the absence of an applied field and for a cubic system, we can write the average of the orientation factor $\langle\ 1 - (\vec{q}.\vec{\eta})^2\ \rangle$ over all domains as $\frac{2}{3}$. Finally, we have:

$$|F_{mag}(q)|^2 = \frac{2}{3} \langle \mu_{Mn^{2+}} \rangle^2 f^2_{Mn^{2+}}(q) \left| \sum_{j=1}^{N} \eta_j e^{iq.r_j} \right|^2 \tag{1.85}$$

Above the magnetic ordering temperature T_C, the intensity of the peaks is purely due to nuclear scattering. However, for temperatures below the ordering temperature; wee see both magnetic and nuclear neutron scattering. For unpolarized neutrons, the nuclear and magnetic intensities simply add.

For a ferromagnetic regime, the Bragg peaks for magnetic and nuclear scattering are at the same position since no magnetic superlattice arises. Well above T_C, in a paramagnetic regime, the magnetic scattering does no simply disappear but rather contributes to the background as diffuse scattering. This intensity has been derived by G. Bacon 1975:

$$I_{para,diffuse}(q) = \frac{2}{3} A \left(\frac{\gamma e^2}{2mc^2} \right)^2 \mu^2_{eff} f(q)^2 \tag{1.86}$$

For temperatures in the vicinity of T_C, we still have short-range magnetic order in the lattice and a magnetic contribution to the Bragg peaks.

1.4 Powder diffraction

Powder diffraction can be done by X-Ray or neutrons, and allows a quick obtention of neutron diffractograms. We will focus on how to guide and detect neutrons. Both instruments that have been used to provide the data have recorded powder diffractograms by using a similar geometry. Nevertheless, differences exist with for example the absence in 3T2 of the long neutron guide used in SPODI (figure 1.9), allowing large take-off angles that result in finer peak widths. First neutrons are guided from the reactor towards the sample via neutrons guides. The neutrons are guided by total reflection, i.e. if the incident angle is lower than a known angle θ_c, the beam is totally reflected. In the Institute Laue Langevin (ILL) in Grenoble, France, the guides are made in nickel-coated glass, utilizing the isotope ^{58}Ni of high scattering length. The guide also eliminates some of the gamma radiation from the reactor thanks that travel straight and go through them, into heavy concrete shielding. Moreover, not all the neutrons successfully travel through the guide since for neutrons, the reflectivity n depends on the wavelength on the neutron, allowing one to select specific wavelengths. Before arriving onto the sample, the neutron beam goes through a first collimator (divergence α_1), focusing the beam on a monochromator. Choosing a specific angle of incidence between a single crystal and the incident beam by rotating the single crystal provides a monochromatic beam, understood by Bragg's law (1.38). The wavelength can be modified by choosing a specific set of Miller indices (table 1.1). A filter can be used additionally to prevent shorter wavelength such as $\frac{\lambda}{2}$ or $\frac{\lambda}{3}$ that can be generated since they are multiple of λ to hit the sample. The neutron beam then goes through a second collimator (divergence α_2) before hitting the powder sample. The scattered neutrons are finally collected by a detector array, usually constituted of ^{3}He tubes with fixed collimators (divergence α_3) so that the neutron beam is collimated and then counted. For both instruments, the multidetector rotates to cover a wider range of q.

The collimators are Soller slits, widely used for both X-rays and neutrons. Soller slits are a set of straight slits that absorbs the misdirected radiation, they are characterized by their number of blades and their heights (Bewer 2012).

Monochromator	Collimators	Detector array
Take-off angle: 155°	$\alpha_1 = 20'$	80 position-sensitive He^3 tubes
Ge(551) : 1.548 Å	$\alpha_2 = 25'$	angular range $2\theta = 160°$
Mosaicity : $\beta = 20'$	$\alpha_3 = 10'$	effective height: 300 mm

Table 1.1: SPODI technical data (Hoelzel, Senyshyn, and Dolotko 2015).

The powder sample are constituted of crystallites,i.e. very small crystals. Powder diffraction is preferred to single crystal diffraction when a single crystal is unavailable. Many materials are studied via powder diffraction; drugs are a common example in

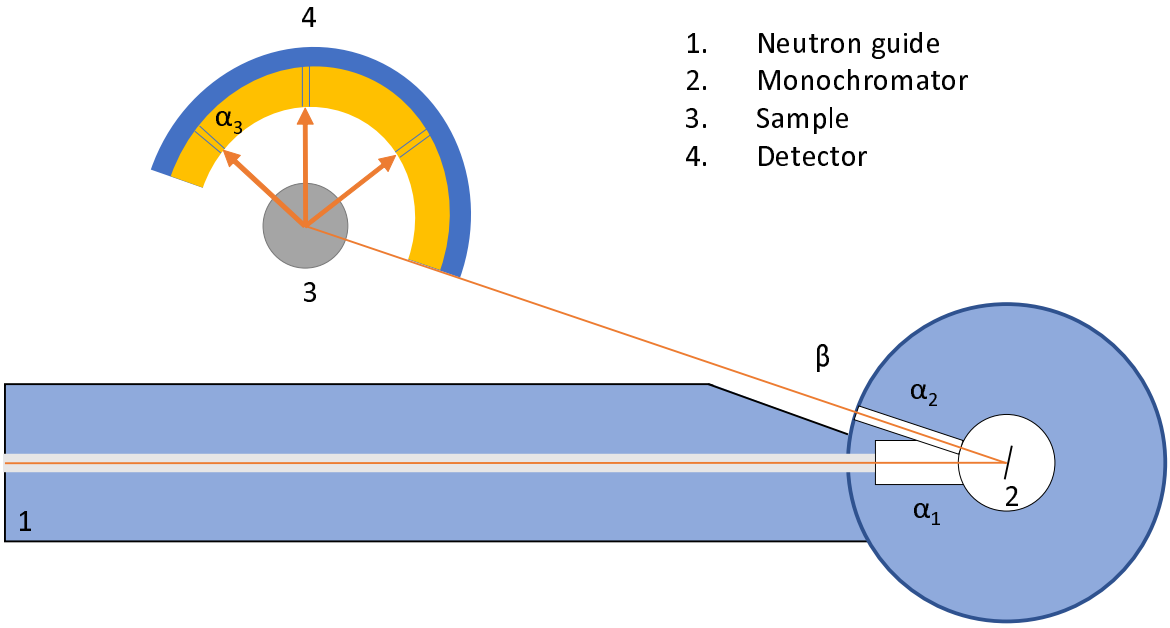

Figure 1.9: Scheme of the instrumental setup used for neutron diffraction in SPODI, with three soller slits collimators, a single crystal monochromator and a multidetector.

which the crystallites can be in the form of a pellet. A good sample must be composed of randomly oriented crystallites to represent all the possible orientations (otherwise, preferred orientations will occur and affect the quality of the data), and have a size between 1 and 10 µm.

Due to their neutral charge, and to the fact that neutrons are non-ionizing, the most common way to detect neutrons is through its reaction with another element present in the detector. Gas-detectors work with ionization chambers, condensers with the space between two metallic plates filled by He^3, which follows the reaction:

$$^3\mathrm{He} + {}^1\mathrm{n} \longrightarrow {}^3\mathrm{H} + \mathrm{p} + 0.77 \ \ \mathrm{MeV} \tag{1.87}$$

The emitted particles are slowed down by the gas and produce electron-ion pairs. the charges are then collected on the metallic plates and the current can be measured (Oed 2003). However if one works with X-rays, one must shield the detector from the photons that do not result from this reaction but rather are a product of the reactor or else to avoid noise and high background. It is possible to discriminate between the energy of the photons and the neutrons that differ from several order of magnitude. Multi-detectors are filled with a quenching gas such as a mixture of xenon (Xe) and methane (CH_4).

Multiplicities

For powder diffraction, where crystallites are randomly oriented, all the symmetry-equivalent reflections that have the exact same interplanar spacing d scatter with the same angle θ resulting in a diffraction pattern in the form of Debye-Scherrer rings (figure 1.10). To obtain the final diffractogram, one must only integrate along the diffraction angle. It is not possible to measure the intensity of each hkl peak individually.

The multiplicity of a peak is the number of equivalent reflections due to symmetry elements for an hkl peak, it must always be taken into account. Its value differ

between low and high symmetry reflections, for example in a cubic crystal lattice, the multiplicity of a peak can be up to 48 and the multiplicity of the (111) peak in a cubic system is $2^3 = 8$, where each miller indices can take the value 1 or -1.

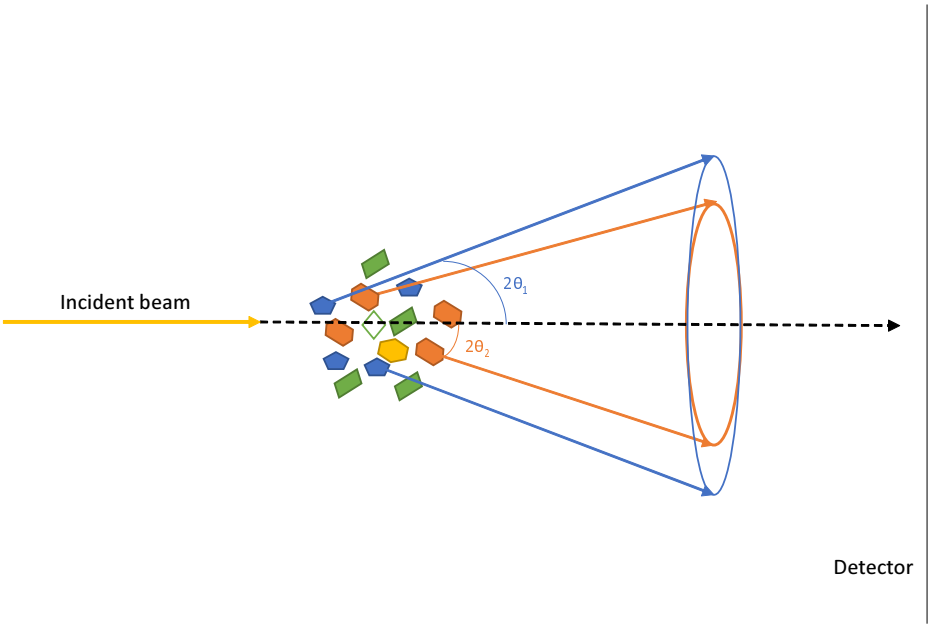

Figure 1.10: Debye Scherrer Rings

Lorentz factor

The Lorentz factor normalizes the amount of reflections that are counted as a function of the scattering angle, it is derived from the experimental setup and is independent of the sample. It results from three different phenomena.

First, a factor of $\frac{1}{\sin 2\theta}$ is due to the rocking scans necessary to entirely cover the surface of a node of the reciprocal lattice that have a width and cannot be seen as zero dimensional points. As seen in figure 1.10, in powder diffraction, the Debye-Scherrer rings that result from the orientation of the crystallites being equally likely, for a specific d_{hkl}, will cover more of the detector's surface for high and low angles than for angles approaching 90°. Thus, the probability of the crystallites to have a plane in the correct orientation for Bragg scattering is proportional to $\cos\theta$. Moreover, for a distance R between the sample and the detector, we have $R\sin 2\theta$ the radius of the Debye-Scherrer rings at the position θ. Hence, the portion of the diffraction cones that will be measured by the 2D detector is dependant on $\frac{1}{\sin 2\theta}$.

The full derivation of (1.88) can be found in Als-Nielsen and McMorrow 2011, the final equation is given by:

$$L(\theta) = \frac{\cos\theta}{\sin 2\theta \sin 2\theta} \approx \frac{1}{\sin\theta \sin 2\theta} \tag{1.88}$$

X-Ray diffraction

Laboratory X-Ray powder diffractometers commonly use Cu-Kα radiation and a Bragg-Brentano geometry for which the incoming beam diverges onto the sample and the diffracted beams is focused on the detector, both beams are at a fixed radius from the

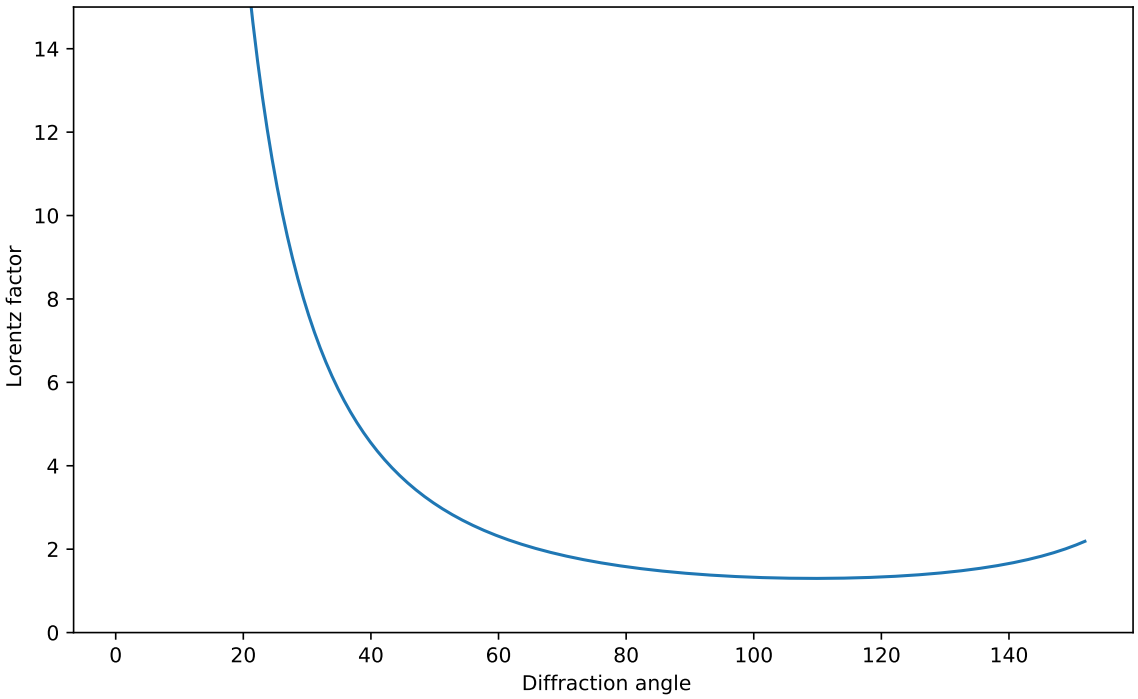

Figure 1.11: Lorentz factor in the angular range of SPODI.

sample position. Focussing the diffracted beam leads to better resolution. It is then possible to either fix the source and move the sample and detector by respectively θ and 2θ or to fix the sample and move the source by respectively $-\theta$ and θ. This second configuration is more adapted to liquid sample for example.

The advantages of using neutrons over X-ray in general are summarized in the table 1.2. For powder diffraction, the main differences hold in the scatterer, in the necessity to account more thoroughly for absorption and in the creation of polarization corrections while using X-ray (which is only possible for the spin in the case of neutrons, no polarization factor for neutrons) at a synchrotron (due to how the X-Rays are emitted). Laboratory sources are unpolarized and in the case of a Bragg-Brentano geometry where the incident beam constantly covers the entire sample the absorption correction is also negligible. The structure factor dependence on q can be seen in the atomic form factor that measures the scattering power of an isolated atom:

$$f(\vec{q}) = r_0 \int \rho(\vec{r}) \exp\left(-i\vec{q}.\vec{r}\right) d^3\vec{r}, \tag{1.89}$$

$$\text{with} \quad r_0 = \frac{e^2}{mc^2} \tag{1.90}$$

with r_0 the Thomson scattering length, e the charge of the electron, m the mass of the electron and c the speed of light. Magnetic neutron scattering depends also on q but the intensity falls off faster than for X-ray for which we do not consider only the unpaired electrons but the whole electronic cloud around an atom of atomic number Z. The structure factor is therefore also proportional to Z. Finally, the angular resolution of X-ray diffraction is higher than for neutron diffraction.

	Neutrons	X-rays
Dependence on q	Constant with q	Decreases for high q
Sample size	Huge, cm^3	Small, between 0.1 and 1 mm
Availability	Only at nuclear facilities	Lab and synchrotrons
Ability to discriminate neighbouring elements	Yes, depending on b	No
Ability to discriminate isotopes	Yes	No
Ability to "see" light elements	Yes	No
Radiation damage	No, but activation	Yes, but no activation
Possibility to investigate magnetic structures	Yes	Yes, in development
Acquisition time	Long due to low flux and low efficiencies	Fast, possibly ultrafast (sub second resolution)
Resolution	Low $\Delta\theta$ resolution	Moderate $\Delta\theta$ resolution

Table 1.2: Summary of the main perks and disadvantages of using neutrons or X-ray for diffraction (Borfecchia et al. 2013).

Chapter 2

Data correction in neutron diffractometers

Introduction

Prior to data analysis, the data must be collected perfectly. For a diffraction experiment, the first step is to find which radiation to use; neutrons or X-Ray. Then, according to the sample (bulk or powder), to the geometry of the diffractometer and to the results one expects from the experiment; the parameters of the instrument (incident wavelength if tunable, counting time, ...) must be chosen. If the quality of the samples is not good enough, if a parameter is not well defined, wrong or if the instrument was not well setup before the collection of the data; it is possible for the quality of the final data to be affected.

During previous attempts to solve the ordering mechanism in the $Ni_{2-x}MnSb$ system (Neibecker 2018), problems linked to the diffractometer arised and no satisfactory conclusion could be drawn from the analysis due to the imprecision of our measurements.

It has been shown that it is possible to fit each or multiple Bragg peaks of a neutron diffractogram by a model (Rietveld 1969). In our case, the novelty is that this model is first used to determine new corrections for the diffractograms obtained by Neibecker before the refinement and the extraction of information such as the lattice parameter or the thermal displacement from the resulting curve. Information that should finally lead to an understanding of the ordering process in our system.

This chapter is first concerned with how the data was obtained and then with how one might be able to apply different types of correction to tackle the diffractograms' problems without further damaging their quality; along with a short presentation of our samples. The sample preparation and data collection were performed by a former PhD student (Neibecker 2018) and this thesis is a continuation of his work.

2.1 Data overview

2.1.1 Sample preparation

As seen in Neibecker (2018), the samples were prepared by induction melting and tilt or suction casting of high-purity elements under Argon atmosphere. After casting, all samples were subject to a solution annealing treatment at 1173–1273K for 48–72 h

depending on the alloy system in order to remove segregation effects from casting. All additional heat treatments and sample preparation procedures were performed on the solution annealed and quenched bulk ingots.

All ingots have been checked for their actual composition using Wavelength-Dispersive X-Ray Spectroscopy (WDS) or Energy-Dispersive X-Ray Spectroscopy (EDS). WDS measurements were performed in collaboration with the group of Ryosuke Kainuma at Tohoku University, Japan. EDS measurements have been performed at the Staatliche Materialprüfamt für den Maschinenbau at Technische Universität München, Germany. For EDS and WDS analysis, thin plates have been cut from the solution annealed ingots that have been mirror-polished in order to provide an adequate surface quality for the measurements. The measured compositions for all samples prepared and used in this thesis is given in the table 2.1.

Compound	Ni (at. %)	Mn (at. %)	Sb (at. %)
Ni1.05MnSb	34.02(25)	33.62(19)	32.36(27)
Ni1.25MnSb	38.15(27)	31.70(11)	30.15(25)
Ni1.50MnSb	42.53(23)	29.19(18)	28.29(18)
Ni1.60MnSb	44.16(19)	27.93(11)	27.91(14)
Ni1.75MnSb	46.50(57)	27.01(50)	26.50(21)

Table 2.1: Sample compositions as determined by WDS/EDS, taken from Neibecker (2018).

The values given are averaged over 8 randomly selected measurements points on the sample in the case of WDS analysis and 5 randomly selected measurements points in the case of EDS analysis. Additionally, all samples have been checked for homogeneity, i.e. the absence of phase decomposition, using Scanning Electron Microscopy.

2.1.2 Objective discussion of data quality

Throughout this thesis, we used distinct sets of data that originated from the characterization of our samples in two different neutron diffractometers. Prior to neutron diffraction, X-Ray diffraction (XRD) was performed to pre-characterize the samples and thereby assert their purity and quality. After having performed XRD and confirmed the quality of the sample, the next step was to apply for a beamtime in a large scale facility such as the Laboratoire Léon Brillouin (LLB) in Paris or the Forschungs-Neutronenquelle Heinz Maier-Leibnitz (FRM II) in Garching bei Munchen. For neutrons, one must go to a reactor simply because there exist no such thing as a laboratory neutron diffractometer. The demand being high, it is mandatory to have a project with a clear purpose and carrying innovation in its field.

Neutron powder diffraction

To clarify the mechanism of the $C1_b$-$L2_1$ phase transition, in-situ Neutron Powder Diffraction (NPD) was performed at various temperatures in Paris at the 3T2 diffractometer at Laboratoire Léon Brillouin (LLB). After the 3T2 data-sets revealed the need to be corrected, room temperature high resolution diffraction was performed at SPODI, a diffractometer at the FRM II reactor, in Garching bei Munchen. Hence, this

second set of data provides us with an optimal spectra for room temperature analysis, that can be used to correct the 3T2 diffractograms by comparing with the room temperature diffractograms.

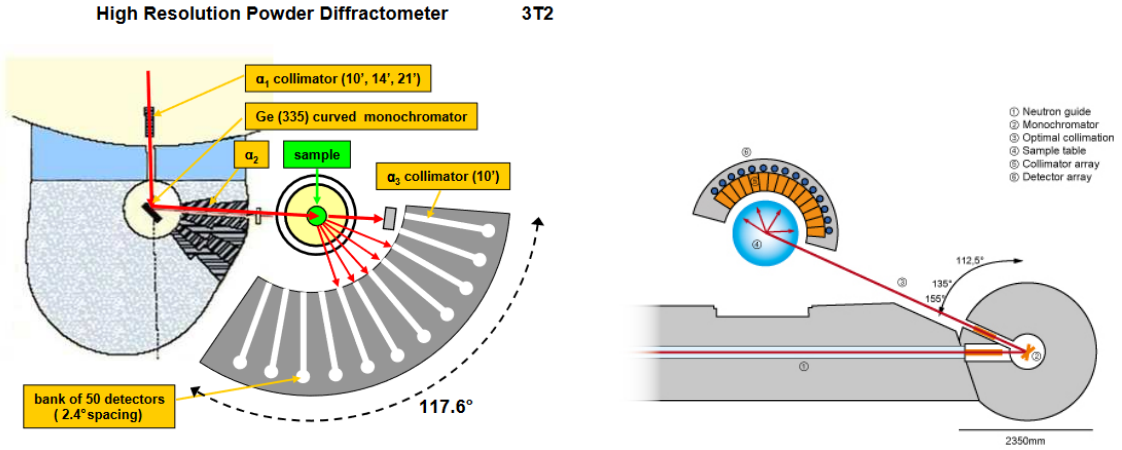

(a) 3T2 *(b) SPODI*

Figure 2.1: The geometry of the 3T2 instrument (figure 2.1a) is similar to the geometry of SPODI (figure 2.1b) both using three soller collimators and a single crystal monochromator with a large take-off angle.

For the in-situ temperature dependent measurements performed at 3T2, the instrument operates with a multidetector (figure 2.1a). The multidetector, composed of individual detector each one preceded by soller slits rotates to cover a wider angular range. For 3T2, the multidetector consists of 52 single detectors tubes each covering a span of 5.4° and separated by 2.4°. Each detector then produces a short diffractogram covering 5.4°. The final diffractogram can then be drawn by summing the intensity of each detector on their individual θ range. At SPODI the multidetector covers a range of 160°, they are 80 individual detectors each covering a range of $160/80 = 2°$. The step width can be change depending on the experiment but in this case SPODI operated with a step width of 0.05° by performing 40 steps. 3T2 also operated with a step width of 0.05° by performing 108 steps. Each detector is also characterized by an efficiency coefficient and a shift coefficient that are both computed by the instrument responsible after calibration, they aim to have a perfect overlap between the neighbouring detectors. These coefficients will be discussed in the next chapters, since they can allow one to correct the efficiencies and positions of the detectors if a problem arise.

If both instruments are part of state of the art facilities, one can clearly notice a difference in the quality of the data between SPODI (figure 2.2) and 3T2 (figure 2.3). This could partly be due to the instrument, SPODI purposely designed for high-resolution data collection for Rietveld refinement using a very large monochromator take-off angle of 155°, a 5 m monochromator–sample distance and Soller collimators, resulting in narrow peaks at high q. Moreover, the width defining the domain of integration for the intensity of the raw data along the Debye–Scherrer lines uses a 2θ dependent variable width accounting for vertical beam divergence effects to avoid asymmetric broadening at low and high scattering angles, while still utilizing the full width of the detector at medium scattering angles (Hoelzel, Senyshyn, and Dolotko 2015).

Two main problems arised from the analysis of the diffractograms. There is a clear

intensity divergence from SPODI (illustrated in figure 2.2 and figure 2.3), too important for middle q. Moreover, the overlap between the neighboring detectors is wrong for 3T2 (figure 2.4 and figure 2.5). The experiment at LLB using 3T2, which is also a high-resolution diffractometer, might have been subject to calibration problems, explaining why it seems that the intensity is too intense in the middle of the diffractograms for medium q. Thus resulting in wrong overlaps between neighboring detectors. The SPODI data was collected to correct the 3T2 data., correcting the intensity problems at medium q and the overlap of the neighbouring detectors that needs to be equal.

The 3T2 data must be corrected to not only be qualitative but quantitative and relevant in a scientific analysis. It is important to be aware of the quality of the data and to proceed to corrections that can be theoretically justified.

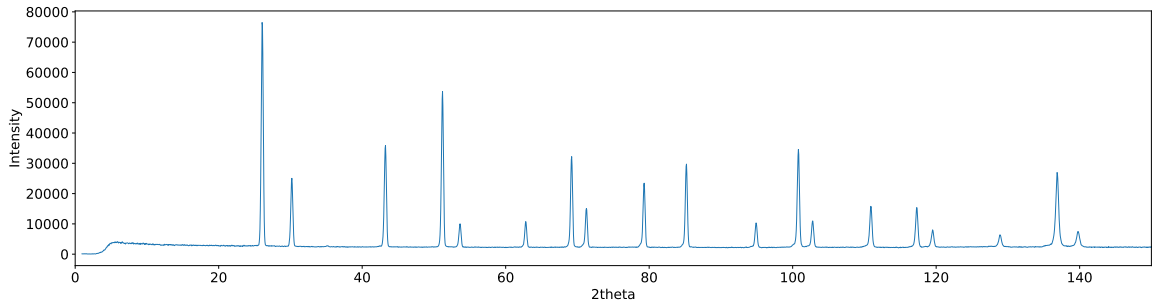

Figure 2.2: SPODI data at room temperature for $Ni_{1.05}MnSb$ as a function of the scattering angle 2θ.

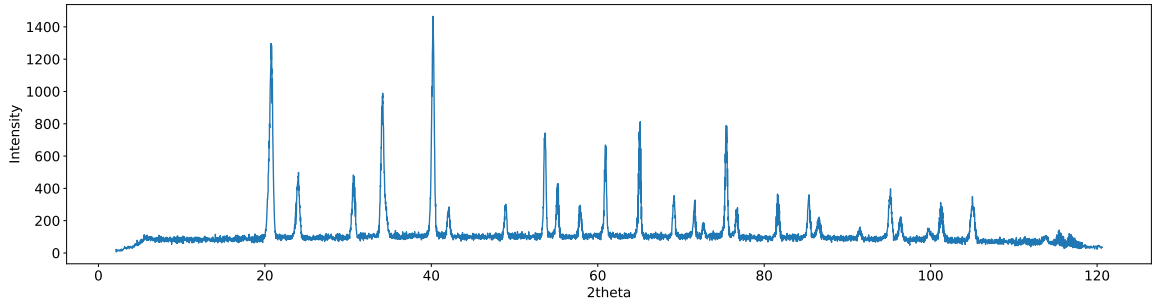

Figure 2.3: LLB data at room temperature for $Ni_{1.05}MnSb$ as a function of the scattering angle 2θ.

2.2 Models and refinement methods for neutron diffraction

For each diagram, the data was drawn for each one of the 52 detectors and plotted along the others (figure 2.4) instead of plotted together (figure 2.2 and figure 2.3). The intensities and the position of the peaks seemed also to differ between the neighboring detectors (figure 2.5), even after having applied the corrections given by the instrument scientists that clearly did not suffice in our case. It was decided to correct the data by using least squares method (LSM) on the diagrams, assuring us with good statistics and allowing us then to directly extract information such as the lattice parameter, the individual structure factor for each (hkl) peak and the Debye-Waller factor from the resulting models.

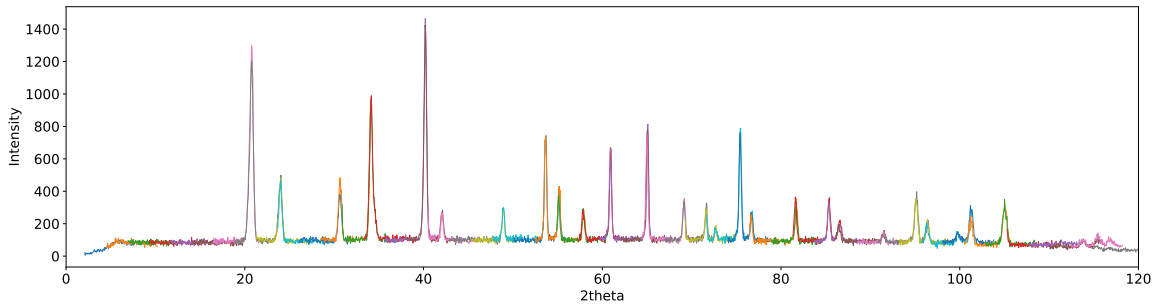

Figure 2.4: LLB data at room temperature for $Ni_{1.05}MnSb$ as a function of the scattering angle 2θ, drawn for each detector.

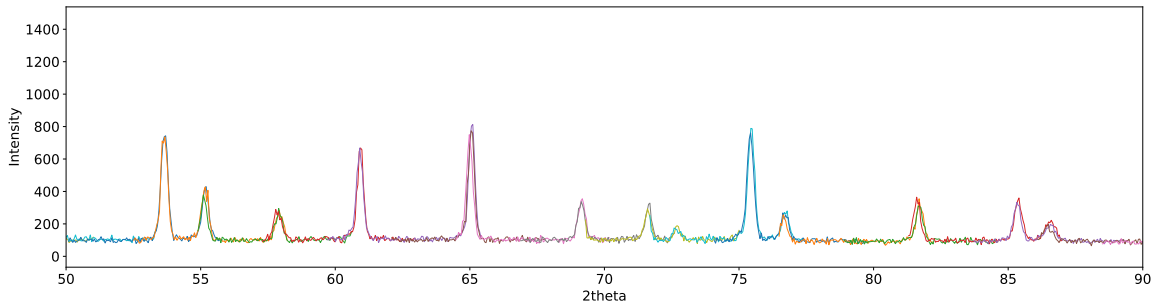

Figure 2.5: LLB data at room temperature for $Ni_{1.05}MnSb$ as a function of the scattering angle 2θ, drawn for each detector. The difference when neighbouring overlap can be clearly seen in this region of medium q.

As mentioned before, two main problems had to be covered, the intensity divergence from SPODI (illustrated in figure 2.2 and figure 2.3), too important for middle q, and the false overlap between the neighboring detectors. But first, we had to define a model for the peaks that could be applied to all the peaks in each diagram. Creating a single model that could then be applied to each diagram with different parameters (taking into account for example that the lattice parameter is different at high temperature than at low temperature) allows one to compare all the diagram in a single programs and thereby finding corrections with the high statistics. To compute precise models throughout the thesis, it was necessary to dive into programming and into regression analysis. In this section, we will first discuss the programming language that was used and then the validity of the different models.

2.2.1 Python, a modern language adapted to science

Since the first publication by Rietveld (1969) that gave its name to the method known as Rietveld refinement; model fitting and data refinement have proven to be powerful scientific tools now commonly used in the crystallographic world. Programs have been developed by the main actors of material science to first help users of large scale facilities but also to provide detailed data analysis software such as the FullProf suite, developed for Rietveld refinement of both neutron and X-Ray powder diffraction by scientists from the Institut Laue Langevin (ILL) in Grenoble, France (Juan Rodriguez-Carvajal 1998).

During this work, an emphasis was put on understanding exactly how process modeling and model refinement worked and on creating a program that could provide the information sought by the author rather than using existing software such as FullProf. This proved to be at first time-consuming but mostly enriching and could not be

avoided since models had to be created to correct the diffractograms in the first place before utilizing the same model fitting routine to draw fitted curved that then provided us information crucial to further satisfactory analysis. Furthermore, it is important to be able to develop non-standard programs for non-standard problems.

Other famous programming languages used in physics could have been used such as MATLAB and Octave. However, due to a previous experience in data fitting using Python (Wolff et al. 2019) and to a desire of the author to develop computer skills in this language, Python 3.7.4 was used for this project.

Terminology and structure

Python is a powerful, object-oriented, programming language receiving increasing attention in science due to its many excellent libraries applicable to mathematics such as NumPy (Van der Walt, Colbert, and Varoquaux 2011), SciPy (Jones, Oliphant, Peterson, et al. 2001), Matplotlib (Hunter 2007); to data analysis with Pandas (McKinney 2010) and Seaborn (Waskom et al. 2014) or to the creation of graphic user interfaces with TKinter. Python is a language that is object-oriented, meaning that one can easily create flexible tools adapted to his own field of work. Moreover, the community is very active and new libraries are constantly being created, sometimes even by instrument scientists of large scale facilities (Nelson and Prescott 2019; Wolff et al. 2019) that also inspired this work.

The language was installed using the anaconda distribution that also contains the main Python libraries for data analysis (NumPy, SciPy, Pandas) as well as JupyterLab, a rich, web-based development environment allowing a flexible use of Jupyter notebooks, images, data-sets, etc... (figure 2.6). The interface is clean and customizable: one can create its own environment and rapidly switch between different Jupyter notebooks. Each notebook is divided in cells and works with a Kernel stocking the notebook's namespace and turning busy when a program is running. One of the best feature of Jupyter is that one can create many different cells leading to dynamic workflow for scientific computing (Nelson and Prescott 2019). An extensive documentation of this software can be found here.

Python has a very specific way of organizing its content that must be followed if one wants to create his own Python library, one must understand the terminology used in Python.

A module is a single file of python code that is meant to be imported in the main script via the `import` function. It is a class with many different objects such as methods (functions specific to an object) or attributes that can then be called from this module.

A package is a collection of python modules under a common namespace. In practice one is created by placing multiple python modules in a directory with a special `__init__.py` module.

A script, if using Jupyter, can be understood as a single notebook that is divided in two parts. First the necessary modules are imported from different packages with their own methods and attributes, then some python code leads to direct results. A complex script can also be seen as an application.

A class defines an object and contains methods (function acting on an object) and attributes that are specific to the object.

A published package can then be called a library if its purpose is to be shared and used by many applications. It provides some generic functionality that can be used by

specific applications. A library can contain multiple packages or even only one module.

A package called `Diffraction` was created to structure the different programs that were used and to give tools that will hopefully be reused in the future. This package can be found in a repository on the GitHub of the author, a `README.md` contains the description of the different modules. Parallel to the thesis, the author followed an online programming course for Python that can be found here (in french) in a desire to learn how to properly organize python scripts, modules, classes, how to describe and define every variable or object according to standards. It is mandatory for a scientist to be up to date in the newest scientific methods and this includes programming languages as well.

Programs

The different modules that were written allow us to proceed to the fitting and refinement of the neutron powder diffractograms from both 3T2 and SPODI. Each diffractogram is then stored as an object defined by a class, the methods working on this class provide us with the respective (hkl) indices and intensities of the Bragg peaks after background substraction, the thermal displacement, the density of states (DOS) of phonons, the lattice parameter, the theoretical magnetic and nuclear structure factor computation depending on the ordering of the structure and more that will be detailed in the next chapter. Before extracting these information, the first purpose of the program is to provide corrections for the 3T2 diffractograms.

The modules are to be applied to this project alone and would need modifications for any extended use but could possibly be extrapolated to other data-sets. Some limitations are of course the lack of data for materials other than cubic Heusler alloys, it could be possible to create a database and to further develop the package but free programs available online such as FullProf are more developed and much more designed for a larger public use. However, it is important to underline that self-written programs will always be needed for problems that are too specific such as the one encountered in this thesis and that in a world that keeps on developing its computer tools and is mandatory to have a good understanding of their working process.

2.2.2 Whole pattern refinement in neutron powder diffraction

Refinement in crystallography and here specifically in Neutron powder diffraction is the process of fitting a curve to a diffractogram. A model is first defined based on the understanding of the material by the crystallographer, it is then refined by tweaking the numerical value of each parameters to improve the resulting curve drawn according to the model and fitting the observed curve (here a diffractogram). Is it mandatory for the crystallographer to have a good understanding of both the parameters of the model and the system at the origin of the observed results to assess the theory behind the model and to make sure that it is as accurate as possible. It is usually possible to fit a model by using many parameters but one should not use more parameters than needed, be able to give a scientific explanation of the origin of each parameter and explain why it has been used in his work.

As mentioned before, refinement for neutron powder diffraction was first derived by Rietveld (1969) and turned out to be a unavoidable tool for materials science in the decades following the publication with publication describing the process for neutron

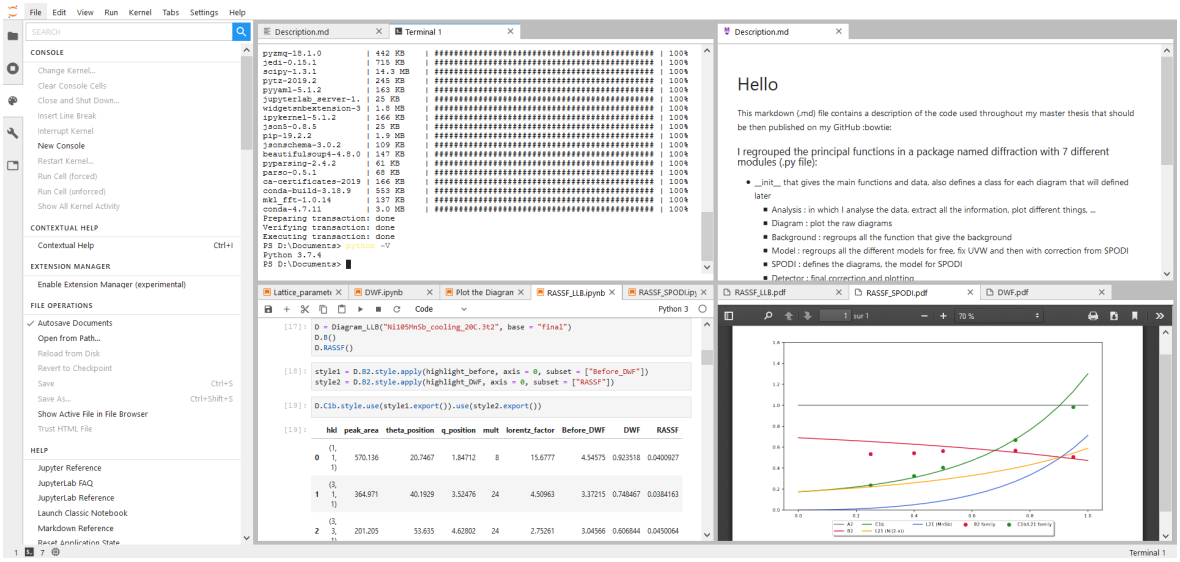

Figure 2.6: JupyterLab allows one to combine raw Python code, Jupyter notebooks, images, windows terminal, Markdowns(.md) and notebook text files (.txt) within a customizable interface.

powder diffraction (Van Laar and Yelon 1984) and X-ray powder diffraction (McCusker et al. 1999). It is important to differentiate refinement and structure solving. Indeed Rietveld refinement works for fitting powder diffraction profiles combined with a solution of the crystalline structure, but it is the crystallographer than first needs to solve the structure and that then needs to work with the output of the refinement, i.e. the refined parameters, to extract information from the curve such as the Debye-Waller factor or the occupancies. This can be done with programs as well, some even combine structure solving and refinement. We will first give insight into the model that was used for the fitting of the 3T2 and SPODI diffractograms and then for refinement. A model in NPD is defined by many parameters that follow either empirical results or thoroughly defined parameters (e.g. the peak width). The different parameters that were used to create valid models will now be explained in details. Then, some insight will be given into the different statistical methods that can be used for the fitting routine such as least squares method.

Peak shape and peak width

The first step in determining which model to use is to know which peak shape one wants to use to model the Bragg peaks and the reasons behind peak broadening. The intensity of a Bragg peak has been derived before (1.45). Theoretically, a Bragg peak indexed by three Miller indices (h,k,l) for a perfectly ordered, pure crystalline system should have the form of a Dirac delta function infinitely thin and nonzero only for its Q value equal to the norm of a reciprocal space vector defined by (1.43). However, both the crystal structure and the instrument affects the distribution of the intensity around the peak position. It is thereby possible and of interest to extract information on the crystal structure from the peak shape.

The shape of a diffraction peak on a diffractogram was first accepted to be that of a Gaussian (Rietveld 1969; Van Laar and Yelon 1984) of position μ, full width at half maximum (FWHM) H, deviation σ and peak area A. The peak area, i.e. the integrated area under a peak is constant regardless of the peak shape and is proportional to the

intensity defined in (1.45). Today, different peak shape are utilized; Lorentzian, Voigt and pseudo Voigt are the most popular examples.

The following table gives the equations at the source of these peak shape. The Gaussian function is probably the most famous. The Lorentzian function is also commonly seen in statistics. Both functions are describe a symmetrical distribution but the Lorentzian is slightly larger at the tail than the Gaussian. It is possible to derive the convolution of the two functions, i.e. the Voigt function that can be approximated by the summation of a Lorentzian and a Gaussian: a pseudo-Voigt.

Gaussian	$A \times \frac{1}{\sigma\sqrt{2\pi}} \times \exp\left[-\frac{(2\theta-2\theta_0)^2}{2\sigma^2} \right]$
Lorentzian	$A \times \frac{1}{\pi} \frac{w}{w^2+(2\theta-2\theta_0)^2}$
Pseudo-Voigt	$A \times \left[a\,L\,(2\theta - 2\theta_0) + (1-a)\,G\,(2\theta - 2\theta_0) \right]$

Table 2.2: The three peak shapes commonly used in powder diffraction and the equations ruling their distributions.

During this work, a Gaussian peak shape is used for it describes more accurately the observed distribution of the peak intensity, more centered than for a Lorentzian. The peak shape is the result of the convolution of the neutron distribution, the monochromator mosaic distribution, the transmission functions of the Soller slits collimators, and the sample shape and crystallinity. If these distributions do not all follow a Gaussian distribution (e.g. the collimation functions are triangles), it is a result of the central limit theorem that their convolution product follows a Gaussian distribution (Rietveld 1969) as shown in figure 2.11. This result in valid for neutrons due to low resolution that does not allow one to see inherent peak shapes, more visible with X-Rays for which the resolution is superior.

A Voigt or pseudo-Voigt function could have been used but since the Gaussian approach did not show limitations at high angles in our project and since the pseudo-Voigt is harder to compute, the Gaussian profile was kept.

The diffractograms issued from 3T2 and SPODI both cover a wide range of theta. q_{max} being inversely proportional to the incident wavelength, since $\lambda_{SPODI} = 1.548\,\text{Å}$ and $\lambda_{3T2} = 1.225\,\text{Å}$, the diffractograms of 3T2 will exhibit more peaks than the ones from SPODI. It is assumed that each peak can be approximated by the Gaussian function defined in table 2.2 with an individual peak area, FWHH and peak position. If one does not see any anisotropic broadening of peaks, i.e. if the width of the peaks attributed to different peak family seem to exhibit the same behaviour; one can define the FWHH thanks to (2.1). By doing so, it is possible to counter the overlapping of neighbouring peaks (more encountered in organic materials than in metallic crystalline structure, not in our case). A θ dependant FWHH will also ease the refining and take into account the position of these peaks into the derivation of the peak width. According to Caglioti (1958), the full width at half-height can then be defined according to the following equation:

$$H^2 = U\tan^2\theta + V\tan\theta + W, \tag{2.1}$$

$$H = 2\sqrt{2\ln(2)}\,\sigma \tag{2.2}$$

with H the FWHH, σ the standard deviation and U, V, W instrument specific parameters.

Caglioti (1958) also proved that for neutron diffractometers working with three soller collimators and a crystal monochromator; U, V and W can be determined if one knows accurately the horizontal angular divergence of each collimator α_i, the take-off angle of the beam θ_m and the mosaicity of the monochromator β. We define α_1, α_2 and α_3 respectively as the horizontal beam divergence between source and monochromator, the horizontal beam divergence between monochromator and sample and the horizontal beam divergence between sample and detector. This geometry has been explained before in chapter 1. For SPODI (table 1.1), we have $\alpha_1 = 20'$, $\alpha_2 = 25'$, $\alpha_3 = 10'$, $2\theta_m = 155$ and $\beta = 20'$. The equations defining U, V and W are given by:

$$U = \frac{4\,(\alpha_1^2\alpha_2^2 + \alpha_1^2\beta^2 + \alpha_2^2\beta^2)}{\tan^2\theta_m\,(\alpha_1^2 + \alpha_2^2 + 4\beta^2)}, \tag{2.3}$$

$$V = -\frac{4\,\alpha_2^2(\alpha_1^2 + 2\beta^2)}{\tan\theta_m\,(\alpha_1^2 + \alpha_2^2 + 4\beta^2)}, \tag{2.4}$$

$$W = \frac{\alpha_1^2\alpha_2^2 + \alpha_1^2\alpha_3^2 + \alpha_2^2\alpha_3^2 + 4\beta^2\,(\alpha_2^2 + \alpha_3^2)}{\alpha_1^2 + \alpha_2^2 + 4\beta^2} \tag{2.5}$$

The computation for SPODI can be found in figure 2.7. For 3T2, due to the necessity of determining new corrections, the parameters given by the instrument where not used but rather determined by whole-pattern fitting. One can either directly use U, V and W in the parameters or simply extract their values from the FWHH. A common set of U, V and W values were first determined and then used as fixed values for all the diffractograms for further analysis. Due to the large freedom on the FWHH, it is necessary to have many peaks to fit, at least 3. One can also see in the case of SPODI that the evolution of the FWHH is quantitative only for high angles and that high angle peak are determinant in the evaluation of U, V and W. This is actually the goal of the high resolution powder diffractometer, to keep a constant and low FWHH at low diffraction angles.

Peak broadening

As said before, the peak width that was defined by Caglioti (1958) is only sufficient if there is no anisotropic contribution to the peaks. It is then possible to fit all the peaks width with a single function. However, some sources of peak broadening might sometimes affect only some directions in the lattice, due to e.g. strain in one direction of the lattice.

Peak broadening is due to both the instrument and the sample that deviate from an assumed perfect model. For example, the wavelength of the instrument is not entirely monochromatic and the sample can have impurities. The final peak broadening can

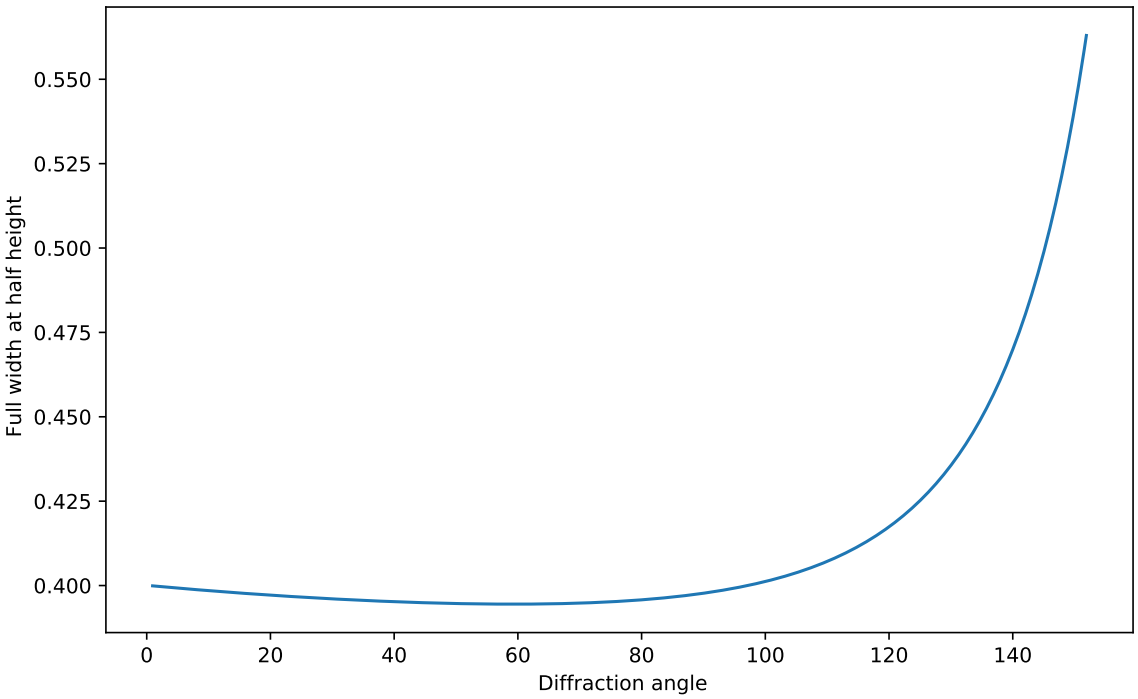

Figure 2.7: The FWHH computed for SPODI given by (2.1) for $U = 0.0137, V = -0.0156$ and $W = 0.160$.

be computed by the convolution of the peak broadening due to the instrument and the peak broadening due to the sample; for example the intensity contribution from an impurity inside the sample is also subject to peak broadening effects from the instrumental setup, both effects are inter-dependant. The substraction of one type of broadening from the other depends on the peak shape (Lorentzian, Gaussian or pseudo-Voigt) and varies from the sum of the squares of each contribution (Gaussian)n the sum of each contribution (Lorentzian) to a complex deconvolution (pseudo-Voigt).

Instrumental contribution	**Sample contribution**
Radiation source has a finite size	Size of the diffracted domain
Incident beam not perfectly monochromatic	Strain due to dislocations and concentration gradients
Possible misalignment of the instrument	Deviation from the perfect crystalline structure
Possible axial divergence between incident/diffracted beams	(impurities, stacking faults; ...)
Configuration of the soller slits (2.1)	
Can be measured by using a sample with very low sample broadening (nearly perfect sample)	Subtract the instrumental contribution after use of a nearly perfect sample

Table 2.3: Peak broadening in neutron powder diffraction. The main contributions are either due to the sample or to the instrumental setup. Instrumental corrections are always in place.

One can notice that the FWHH defined earlier does not directly depend on the sample and can not possible take into account stress, strain or preferred orientations. The instrumental contribution to peak broadening results in a slow increase of the peak width at very low angles and in a rapid increase for high angles.

The sample contribution to peak broadening can be used to determine the size of the domain in a specific direction. A formula linking crystallite size and peak width was derived by Scherrer in 1918:

$$\Gamma = \frac{K\lambda}{\beta \cos\theta} \tag{2.6}$$

where Γ is the mean size of the ordered crystalline domains, K is a dimensionless shape factor (constant, depends on the sample) usually taken as equal to 0.9 and β is the FWHH after substraction of instrumental broadening and other sample contribution to broadening (e.g. strain). For example, if we notice that the FWHH is higher for the peaks of the (100) family in a cubic sample, we can deduce that the crystallites or the domain of diffraction is smaller in this direction.

To understand the contribution of inhomogeneous strain to the peak broadening, one can visualize the (hkl) planes separated by a distance d_{hkl} (1.42). If the lattice is subject to homogeneous tensile or compressive stress perpendicular to the planes, the result will just be an evolution of the interplanar distance and a shifting of the position of the associated Bragg peak. However, if we have inhomogeneous strain due to structural defects (impurities, vacancies, dislocations, ...) the distance between the neighbouring planes will evolve in space, which could result in a distribution of the shifts in the peak position i.e. peak broadening. The following equation, derived from Bragg's law, relates the mean inhomogeneous strain ϵ to the resulting peak broadening β_ϵ:

$$\beta_\epsilon = C\epsilon \tan\theta \tag{2.7}$$

where C is a constant depending on the type of strain in the sample.

Peak asymmetry

Due to axial divergence in terms of finite sample and detector sizes, asymmetric peaks can be seen in the diffractograms at low theta. The functions used for peak asymmetry are semi-empirical. The integrated peak area is not affected but the peak position might be shifted which would cause errors in the refinement. We can use the simple equation described in Rietveld (1969) to correct the distribution of the peak:

$$y_i = I_k \left(1 - P(2\theta_i - 2\theta_k)^2 \times s/\tan\theta_k \right. \tag{2.8}$$

Where P is the asymmetry parameter, $s = +1, 0, -1$ depending on relative position of the point to its mean position. I_k is the intensity before the asymmetry correction.

Peak indexing

It is quite straightforward to determine the positions of the Bragg peak in a powder diffractogram by simply taking the mean value of the Gaussian after asymmetry corrections. One can then extract quantitative information about the crystal structure solely from the indexing of the Bragg peaks. The final value of the lattice parameters are given by the refining of the interplanar spacing through the Bragg (1.38) and the reciprocal space metric tensor. Since we work with a cubic system, the computations are relatively simple. The dependence of d_{hkl} on the lattice parameter has been derived before for a cubic system (1.42) given again here with Bragg's law:

$$d_{hkl}\frac{|\vec{a}|}{\sqrt{h^2+k^2+l^2}}, \tag{2.9}$$

$$\lambda = 2d_{hkl}\sin\theta \tag{2.10}$$

There are two ways to extract the value of the lattice parameter during the refinement. First, one can let the minimization routine find the Bragg peak positions and then use this set of values to determine the lattice parameter via (2.11). The second possibility that was chosen here is to force the positions of the peaks to be directly determined via the lattice parameter and the Miller indices. This method needed some preliminary indexing that can be done theoretically if one knows the crystalline structure or by analyzing the diffractogram but allowed us to directly refine the lattice parameter while being sure that the peaks were not misindexed.

$$2\theta = 2\arcsin\frac{\lambda}{2d_{hkl}} \tag{2.11}$$

With a simple python function that returns the position of the peak (figure 2.8).

```
def peak_index_theta_SPODI(a, h, k, l):
    """Peak index in function of lattice parameter,
    with the wavelength from SPODI"""
    dhkl = a/ np.sqrt(h**2 + k**2 + l**2)
    q=(2*pi/dhkl)
    return      np.degrees(np.arcsin((q*10**(10))*
        (wavelength_SPODI/(4*pi)))*2)
```

Figure 2.8: Python function computing the position of the peaks from the lattice parameter and the Miller indices.

The minimization routine was always performed through a least squares method, a method that will be described in details in the following paragraphs. To determine the exact lattice parameter, one must also take into account the instrumental zero-shift in the refinement that could lead to misinterpretations if excluded. The positions of the peaks are all shifted from a constant value due to a slight difference between the 180° position of the instrument and the real position of the incident beam.

The wavelength of the instrument being directly used in the determination of the lattice parameter from the peak positions, one must be assured that the value given by the instrument is correct, otherwise it is possible to refine the wavelength using a simple system where the crystal structure is known to confirm the value of λ following the same method.

One can see in table 2.4 that some peaks will even overlap for high symmetry structures such as cubic, in our case (511) and (333) or (442) and (600). One can then simply add both multiplicities during the refinement process to take the peak overlap into account.

$C1_b$	Miller indices	(111)	(311)	(331)	(511)	(333)	(531)	(533)	(551)
	$h^2+k^2+l^2$	3	11	19	27	27	35	43	51
B2	Miller indices	(200)	(222)	(420)	(440)	(620)	(444)	(642)	
	$h^2+k^2+l^2$	4	12	20	32	40	48	56	
A2	Miller indices	(220)	(400)	(422)	(442)	(600)	(622)	(640)	(820)
	$h^2+k^2+l^2$	8	16	24	36	36	44	52	68

Table 2.4: First Miller indices for each peak family, the value computed by $h^2+k^2+l^2$ is then proportional to the peak positions through (2.11).

Background modelling

If a neutron does not contribute to the intensity of a Bragg peaks through coherent scattering, diffuse elastic coherent scattering or inelastic coherent scattering, it can contribute to the background. This is due to several different physical phenomena. First, we have the incoherent scattering from the incoherent cross-sections as defined in (1.31). It is due to deviations of the scattering length from the mean value b_i. The deviations result from the system that is no more assumed to be be constituted of the same nuclei without a nuclear spin but of isotopes with different scattering lengths distributed around b_i and with a nonzero nuclear spin I.

By simply looking at the evolution of the background and the Bragg peaks with temperature, one can see that some intensity is transferred from the Bragg peaks to the background as the temperature increases. The increase in diffuse scattering (neutrons scattered at many angles rather than at a specific angle) with temperature is due to both the Debye-Waller factor that increases with the temperature and to the magnetic intensity, directly linked to the order in our system. The contribution from magnetism has been derived before (1.86) and is constant well above the transition temperature T_c where the system switches from a ferromagnetic regime to a paramagnetic regime and does not show magnetic short-range order. The Debye-Waller contribution known as thermal diffuse scattering (TDS) increases with temperature, following the evolution of the isotropic thermal displacement $u(\vec{t})$.

Besides the dynamic displacement of atoms, the lattice is also subject to static displacement, i.e. point defect such as site substitution, impurities in the lattice, vacancies or any kind of disorder and deviations from the assumed crystalline model also contribute to the background by affecting the long-range order of the crystal structure. The repercussion of a single defect are important for they induce short-range order in the lattice; the displacement decreases slowly and a very large amount of neighbouring atoms can be affected.

The point defects could be due to errors in the composition (evaporation during melting, starting with excess for one element). In our case, the sample composition (table 2.1) has very low deviations from the theoretical compositions. These defects have been classified (first and second kind of Krivoglaz defects) depending on how they contribute to the diffuse scattering.

The background contribution are either constant with q (diffuse scattering) or increase with q (e.g. DWF). However, a background decreasing for high q values was observed, confirming our theory that the incoming intensity was too high for medium

q. To fit the observed data to a model, one can include a function describing the background in the model if the background is of interest, so that it is also possible to refine this function returning an accurate description of the background. In this case, the background was first computed by linear interpolation. The peak positions were first graphically determined and the points y_i that were inside the peak were assigned a value by interpolation. A polynomial curve of degree 5 (2.13) was then fitted through least squares method and assigned to the background of the curve (figure 2.9). A degree 5 was chosen to accurately describe the variations of the intensity (impossible at low degrees) while also avoiding polynomial wiggle more pronounced with higher-degree polynomial. At higher temperatures, the background proved to be difficult to fit though a polynomial equation, not just decreasing with q anymore but showing strong contributions from coherent inelastic scattering near the Bragg peaks.

$$B(x, \vec{a}) = \sum_{i=0}^{5} a_i \times x^i + \epsilon \tag{2.12}$$

$$B(x, \vec{a}) = a_0 + a_1 x + a_2 x^2 + a_3 x^3 + a_4 x^4 + \epsilon \tag{2.13}$$

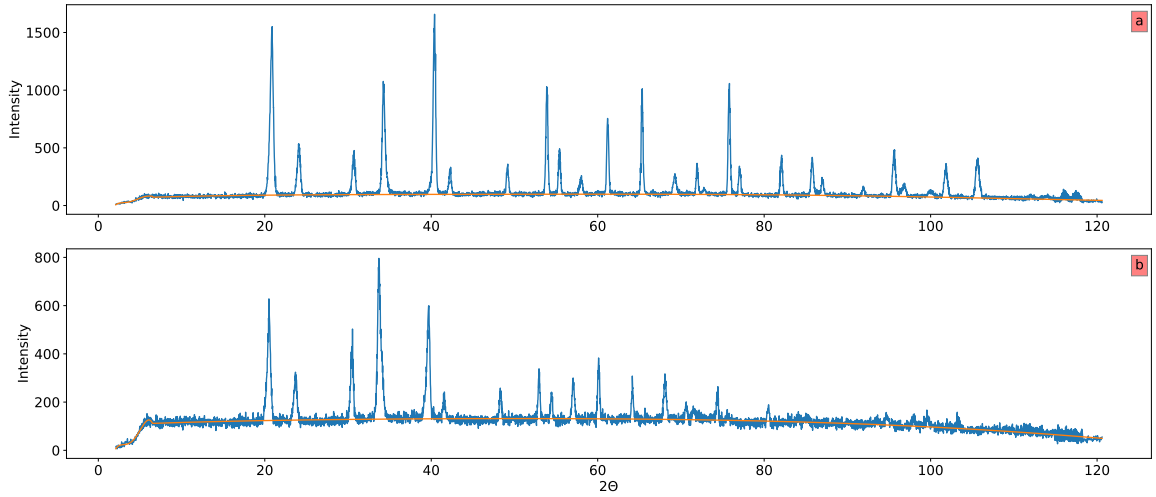

Figure 2.9: Background curves fitted through a classical polynomial approach plotted in orange for $Ni_{1.05}MnSb$ at 45 °C (top) and 790°C (bottom) for 3T2.

It proved to be easier to use weighed least square methods to fit the diagram by (2.14) with first kind Chebyshev polynomials T_n, especially for high temperatures (figure 2.10). The weights as well as the degree N of the equation were found empirically. The weights taken during the weighed least squares regression were simply taken as the square of the variance of the counting statistics. More information about the variance is provided later. The background is then given by:

$$f(x, \vec{a}) = \sum_{n=0}^{N} a_n T_n(x) \; + \; \epsilon \tag{2.14}$$

with a_n the $N + 1$ coefficients determined by the weighed least square regression.

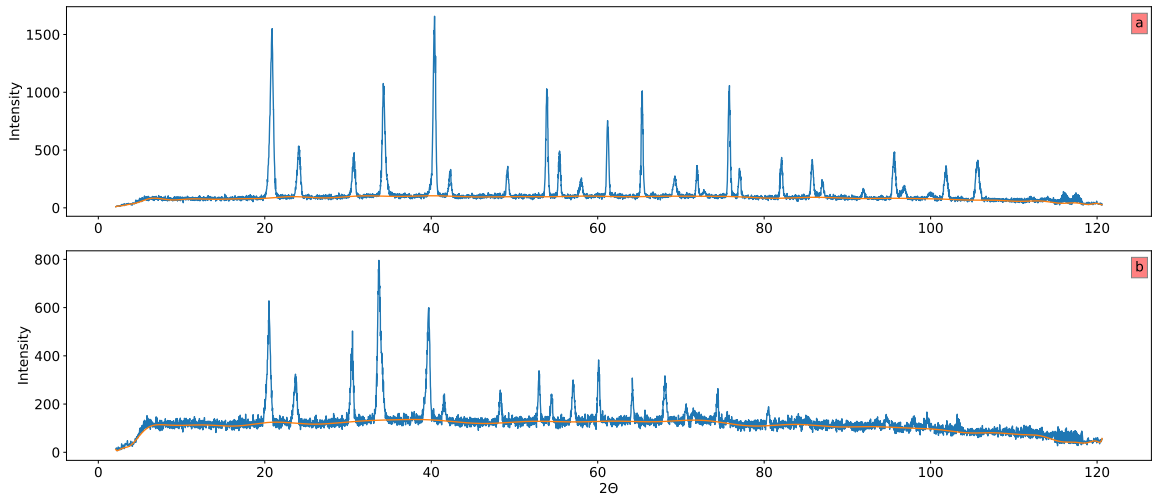

Figure 2.10: Background curves fitted through a Chebyshev polynomial approach plotted in orange for $Ni_{1.05}MnSb$ at 45 °C (top) and 790°C (bottom) for 3T2. The background curves follows the evolution of the background much better than in a classical polynomial approach.

Final model

After having listed the parameters in play, one can derive the final intensity collected by the instrument and create a model that is used inside the fitting routine. It is necessary to understand the role of each parameter since the goal of this discussion is to provide a model that can be used for both the fitting of the diffractograms and a subsequent refinement of the parameters that can then be used to understand the ordering process in $Ni_{2-x}MnSb$. It would be possible to fit the models by a summation of ordinary Gaussian peak but it would then be impossible to extract information from the diffractograms.

The peak areas are given by (1.45), defined in the previous chapter, in which are included both the structural parameters and the instrumental parameters such as the multiplicity for powder diffraction. Equations (2.15) and (2.16) have been used during our refinements to describe the intensity received by a point y_i after substraction of a background B_i following $y_i = Y_i - B_i$. Y_i is the total intensity received by the detector binned to θ_i. Since the peaks look symmetric, the asymmetry of the peaks was neglected in a first approach.

$$y_i = \sum_k^{N_p} f_k(2\theta_i, \vec{\beta}) + B(\theta_i, \vec{\beta'}) + \epsilon \tag{2.15}$$

$$f_k(2\theta_i, \hat{\vec{\beta}}) = C \times A \times j_k \times L(2\theta_i) \times \exp(-2W) \times \frac{1}{\sigma_k\sqrt{2\pi}} \times \exp\left[-\frac{(2\theta_i - 2\theta_k)^2}{2\sigma_k^2}\right], \tag{2.16}$$

$$\hat{\vec{\beta}} = (C,\ A,\ j_k,\ W,\ \sigma_k,\ \theta_k) \tag{2.17}$$

The subscript k designs variables taking a single value per peak when the subscript i designs variables that change for each $(\theta_i,\ y_i)$ bin of the detector. A is an instrumental constant that differs between 3T2 and SPODI. j_k is the multiplicity of the peak, L_k the Lorentz factor defined for each peak by taking the peak position $2\theta_k$ and finally

$\exp(-2W)$ is the Debye-Waller factor. The peak follows a Gaussian distribution with σ_k the standard deviation and $2\theta_k$ the position of the Bragg peak defined by (2.11). The intensity of the peak has also been normalized by the maximum intensity of a Gaussian ($\sigma_k\sqrt{2\pi}$). Finally, ϵ is the error associated to each bin.

The structure factor F_k is not used in the model but rather modelled by a constant C, the peak area, normalized and corrected by the Lorentz factor , the multiplicities and the Debye-Waller factor so that one can extract in the future the structure factor from the refinement. It is theoretically possible to compute the structure factor beforehand and to include it in the refinement (Rietveld 1969) but this would impinge on our idea of analyzing the data by using different structure factors, explained in Chapter 3. The method describes in this chapter was first published by Pawley (1981).

The final number of counts received by the detector for Bragg peaks can be modelled as a summation of the $f_k(2\theta_i, \vec{\beta})$ function over the number of peaks N_k. Multiple peaks could overlap if their positions were relatively close but this phenomena was not seen on our diffractogram, at least for Bragg peaks. The common definition of the FWHH by (2.1) is still useful to discriminate additional peaks due to the sample's environment in the instrument. According to the previous equation, one can easily include the theta dependant FWHH by substituting the standard deviation by H (see (2.2) and (2.1)).

It is important to subtract the background $B(\theta_i, \vec{\beta}')$ before or to model it outside $f_k(2\theta_i, \vec{\beta})$ if one wants to only fit the peaks for otherwise the background would be seen as a contribution shared by all the peaks which is physically wrong and very complicated to fit. Refining the function with both the background and the function describing the peak intensity results in better statistics.Fmulti A first approach to our model is drawn in the figure 2.11, for the intensity given from a single detector and in figure 2.12 for the model of a diffractogram by whole pattern fitting.

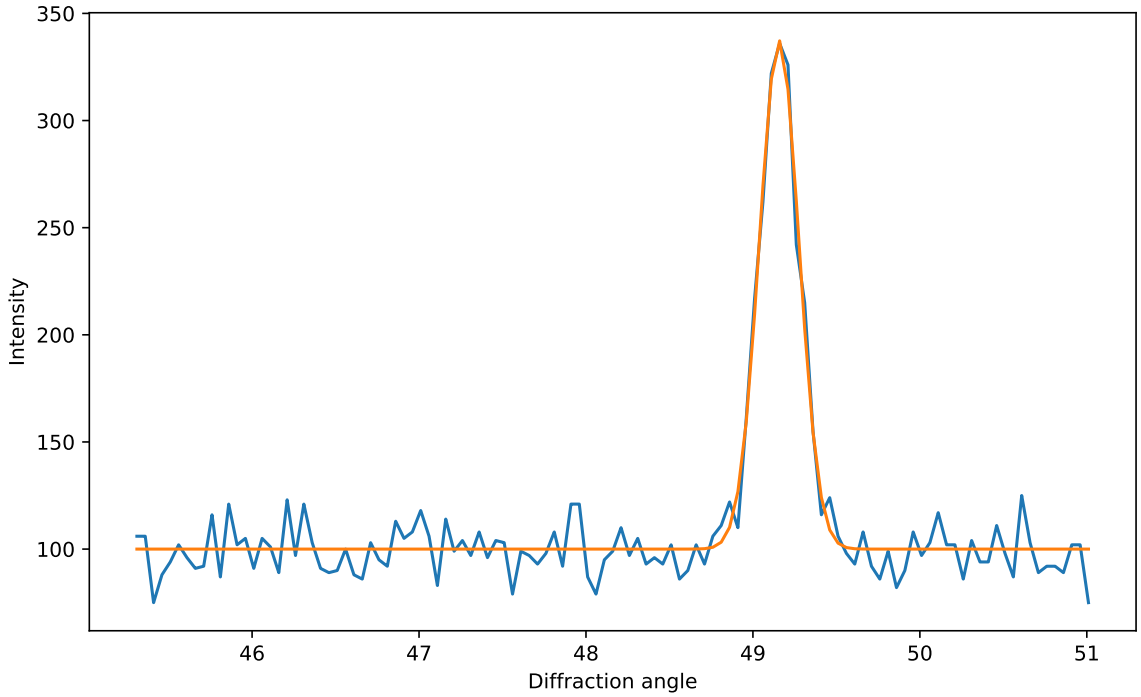

Figure 2.11: A Gaussian model fitted through least squares method on a single detector with $A = 70.36, \mu = 49.16$ *and* $\sigma = 0.12$.

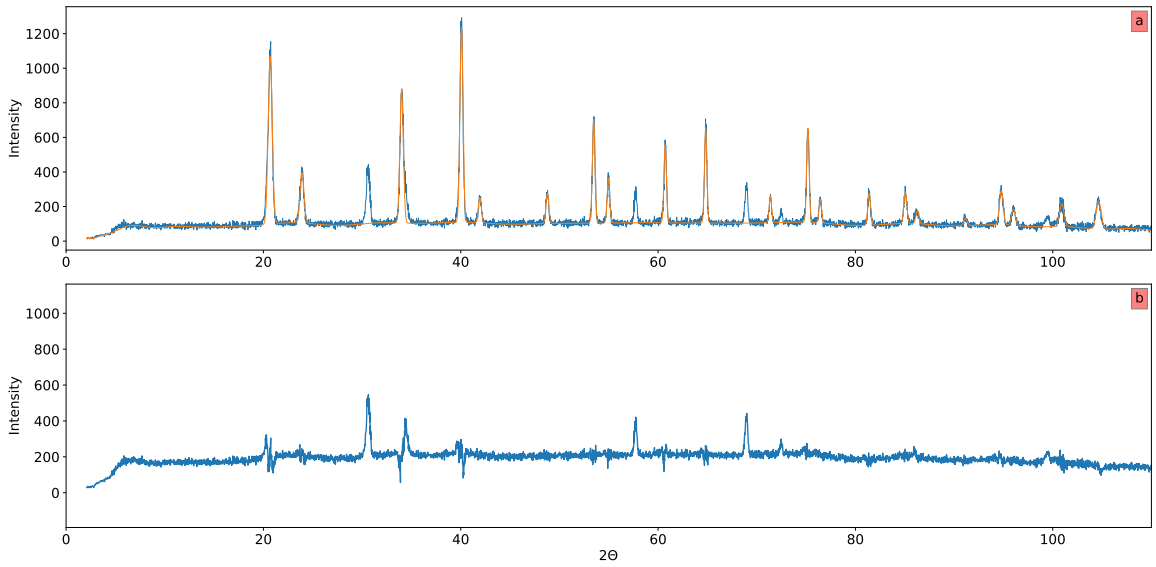

Figure 2.12: A 3T2 diffractogram for $Ni_{1.05}MnSb$ at 200°C, model fitted through least squares method(a) and residues (b).

2.2.3 Least squares method

Process modelling

Process modelling is defined as the description of a **response variable** y by the summation of a deterministic component given by a **mathematical function** $f(\vec{x}, \vec{\beta})$ plus a random ϵ that follows its own probability distribution (see the engineering statistics handbook published by the National Institute of Standards and Technology NIST/SEMATECH 2012). We have:

$$y = f(\vec{x}; \vec{\beta}) + \epsilon \tag{2.18}$$

Since the model cannot be solely equaled to the data by the deterministic mathematical function f, we talk of statistical model that are only relevant for the average of a set of points y. Each response variable $\vec{y_i}$ defined by the model is binned to a predictor variable $\vec{x_i}$ which are inputs to the mathematical function. $\vec{\beta}$ is the set of parameters that will be used and refined during the modelling process. In general we have:

$$\vec{x} \equiv (x_1, x_2, ..., x_N), \quad \vec{y} \equiv (y_1, y_2, ..., y_N), \quad \vec{\beta} \equiv (\beta_1, \beta_2, ..., \beta_M) \tag{2.19}$$

It is important to differentiate between errors and residuals, if one works with a sample of a population and evaluates the deviation between one element of the sample and the average value in the sample, we talk of residuals. However, the error is the deviation between the value of this element and the the average on the whole population, the true value that is unobservable. For least squares method, the residuals will be evaluated, difference between the observed value and the mathematical function.

The value of the parameters is usually unknown before modelling unless for simulation experiments where one uses a model with a predetermined set of parameters to evaluate its outcome. For refinement, the parameters can be first-guessed and approximated from literature (e.g. the lattice parameter) but it is the purpose of the refinement to lead to new and accurate parameters. The relation between the parameters and the predictor variables depends on the nature of our problem.

Linear least squares method

For a linear problem, a generic function produced by the summation and multiplication of the predictor variable by constants or the predictor variable is used, e.g. the polynomial model used in the determination of the background (2.13) or (2.20). In that case, one must use a linear least squares regression method, or simply named least squares method. We speak of linear models when they are linear in the parameters, so that in the end they consists of a system of linear equations solved by determining the value of $\vec{\beta}$.

$$f(\vec{x};\vec{\beta}) = \beta_0 + \beta_1 x_1 + \beta_2 x_2 + \ ... \tag{2.20}$$

The linear least squares method is now commonly used for many systems that are either inherently linear or well-approximated by linear models on subsets of their definition domains.

However, since this method is limited into the shapes that it can take by using linear parameters. There can be some difficulties to extrapolate for data sets that show sharp evolution over long range definition domains. For such data sets, it is possible to use different methods that are based on the understanding of linear least squares method.

Nonlinear least squares method

Nonlinear least squares method uses the basic equation (2.18) in which the functional part is not linear with respect to the parameters $\vec{\beta}$ and for which the value of the parameters is determined using least squares method. An example of a nonlinear model is the very model that is used throughout this thesis (2.16) which is nonlinear in the use of sinuses and exponential. A nonlinear least squares method allows one to fit more accurately complex systems that can be found in the nature (diffraction) or even in computer science, engineering, finance... If the model is defined over a large range, it is possible to think about extrapolation or applying the model to similar data sets. However, a nonlinear method must be done iteratively, with starting values or initial guesses as close as possible to the exact values. The concept of using iterative algorithm can be understood by working progressively, starting with the initial values $\hat{\beta}^0$ and using derivatives to find a global minimum with the parameters $\vec{\beta}$. It is then possible to iteratively solve local linear problems.

$$\beta_j \approx \hat{\beta_j^{k+1}} = \hat{\beta}_j^k + \Delta\hat{\beta}_j \tag{2.21}$$

where $\hat{\beta}_j^k$ is the estimated value of the parameter β_j at the k iteration, and in general $\hat{\vec{\beta}}$ is an estimation of the true parameters $\vec{\beta}$. A good understanding of the system is hence needed, otherwise the nonlinear method will either fail due to the impossibility to converge towards a good set of parameters or converge towards a local minimum instead of a global minimum.

Weighed least squares method

There is however a shared issue between standards linear and nonlinear least squares regression methods. Sometimes the response values can show strong variations over the range of the predictor values, this phenomena is known as heteroscedasticity. In that case, if one assumed the errors to be Gaussian following a normal distribution and

notices that having different errors would be more coherent, a weight can be introduced as a prefactor of the residual when minimizing the square of the residuals, i.e. the square of difference between the observed value and the mathematical function. This weight W_i will determine how much each residual is important into the determination of the final parameter.

In the case of the neutron powder diffractograms for which the intensity of the points is ruled by many different physics process, the use of weighed least squares is one way to improve the quality of the regression. For example, the intensity of a point belonging to a Bragg peak is much greater than for the points that only receive diffuse scattering and for which the background impinges on the peaks with increasing q due to factor such as the DWF; it is clear that each (θ_i, y_i) bin does not have the same error and should not have the same importance in the determination of the model. To counter this, one must give less importance to the points that were less precisely measured, i.e. by using weights determined individually before the fitting routine that quantify the precision of each point. A standard approach for a system in which the standard deviation of the errors is not constant, is to equal the weight of a point to the inverse of the variance for this point, yielding a most precise fit that adapts to the quality of the data and treats each point accordingly.

Of course one must know exactly the variance in order to apply this method, the weights must be determined precisely relative to one another otherwise this method will just add errors instead of relieving the model from them. If one does not know the weights exactly, one can estimate them from the experiment but only with high statistics to be certain that the weights are correctly estimated and do not lead to a wrong result. In our case, the weights are at first simply equalled to the variance of the counting statistics. For each point y_i created by subtracting a background B_i from the total intensity Y_i, we have a statistical weight W_i defined by (2.23), the variance of the background in unknown since the background is determined graphically, the variance of the total intensity Y_i is equal to itself in counting statistics Rietveld 1969. We have:

$$W_i = \frac{1}{\sigma^2(Y_i) + \sigma^2(B_i)} = \frac{1}{Y_i}, \tag{2.22}$$

$$with \quad y_i = Y_i - B_i \tag{2.23}$$

Minimization process

The "method of least squares" that is used to obtain parameter estimates was independently developed in the late 1700's and the early 1800's by the mathematicians Karl Friedrich Gauss, Adrien Marie Legendre and (possibly) Robert Adrain [Stigler (1978)] [Harter (1983)] [Stigler (1986)] working in Germany, France and America, respectively.

To find the value of the parameters in a linear or nonlinear least squares method, we use the weighed least squares method. The function $f(\vec{x}, \hat{\vec{\beta}})$ is fitted to the data y by minimizing the following criterion:

$$\chi^2 = \sum_i^N W_i \left\{ y_i - f(x_i; \hat{\vec{\beta}}) \right\}^2 = \sum_i^N W_i \, r_i^2 \tag{2.24}$$

with N the amount of (θ_i, y_i) bins in our experiment and r_i the residuals.

The sum of the square of the deviations between the data point y_i of the (θ_i, y_i) bin and the corresponding $f(\vec{x_i}; \hat{\vec{\beta}})$ in the model is minimized. For nonlinear models such

as ours, the computation must be done via iterative algorithms. The algorithm finds the solution of a system in which each of the partial derivative with respect to each parameter is zero, i.e. when the gradient is zero. For a system with M parameters β_s, we have M times the following equation:

$$\left(\frac{\partial D}{\partial \beta_s}\right)_k = \sum_{i=1}^{N}\left[2W_i\left(y_i - f(x_i;\hat{\vec{\beta}})\right)\left(\frac{\partial f(x_i;\hat{\vec{\beta}})}{\partial \beta_s}\right)_j\right] = 2\sum_{i=1}^{N} W_i r_i\left(\frac{\partial r_i}{\partial \beta_s}\right)_j = 0 \quad (2.25)$$

the subscript j stands for the other parameters different from β_s that are taken as constant in the partial derivative. One can apply the Taylor expansion to (2.25) by assuming that the true parameters $\vec{\beta}$ can be individually written as $\beta_j = \hat{\beta}_j^k + \Delta\hat{\beta}_j^k$ and that the term $\Delta\hat{\beta}_j^k$ tends to zero. We develop the Taylor series as follows for the k iteration:

$$f(x_i;\vec{\beta}) = f(x_i;\hat{\vec{\beta}^k} + \Delta\hat{\vec{\beta}^k}) \approx f(x_i;\hat{\beta}^k) + \sum_{j=1}^{M}\left(\frac{\partial f(x_i;\hat{\beta}_j^k)}{\partial \hat{\beta}_j}\right)_s (\Delta\hat{\beta}_j^k) + o\left(\Delta\hat{\beta}_j^k\right) \quad (2.26)$$

$$= f(x_i;\hat{\vec{\beta}^k}) + \sum_{j=1}^{M} J_{ij}\Delta\hat{\beta}_j^k + o\left(\Delta\hat{\beta}_j^k\right), \quad (2.27)$$

$$\text{with: } J_{ij} = \left(\frac{\partial f(x_i;\hat{\beta}_j^k)}{\partial \hat{\beta}_j}\right)_s \quad (2.28)$$

where J_{ij} is the Jacobian, computed at each iteration. The terms of order higher than 1 are ignored when $\Delta\hat{\beta}_j^k$ tends to zero. The residuals can be rewritten according to the previous equation as:

$$r_i = y_i - f(x_i;\hat{\vec{\beta}}) = y_i - f(x_i;\hat{\vec{\beta}^k}) + f(x_i;\hat{\vec{\beta}^k}) - f(x_i;\hat{\vec{\beta}}) \approx \Delta y_i - \sum_{j=1}^{M} J_{ij}\Delta\hat{\beta}_j^k, \quad (2.29)$$

$$\Delta y = y_i - f(x_i;\hat{\vec{\beta}^k}) \quad (2.30)$$

By rewriting (2.25) with another Jacobian and by replacing $f(x_i;\hat{\beta})$ by (2.26), we have:

$$\sum_{i=1}^{N}\left[2W_i\left(\Delta y_i - \sum_{j=1}^{M} J_{ij}\Delta\hat{\beta}_j^k\right)J_{is}\right] = 0 \quad (2.31)$$

$$\sum_{i=1}^{N}\sum_{j=1}^{M} W_i J_{ij}\, J_{is}\,\Delta\hat{\beta}_j^k = \sum_{i=1}^{N} W_i J_{is}\Delta y_i \quad (2.32)$$

It is possible to simplify the equation by using matrices:

$$(J^T W J)\Delta\beta = J^T W \Delta y \quad (2.33)$$

The matrix $(J^T W J)$ contains information from the mathematical model, it is the weighed sum of the product of the partial derivatives contained in the Jacobians. The

data is contained in the matrix Δy. To find the next shift $\Delta\beta$, the algorithm must invert the matrix $(J^T W J)$:

$$\Delta\beta = (J^T W J)^{-1} \times J^T W \Delta y \tag{2.34}$$

Therefore, if the inversion is impossible, the model is at fault. If the inversion is possible but the data is wrong, then the shifts will be wrong. This equation is the basis of the Gauss-Newton algorithm used to minimize the sum of the squares of the residuals between the data and the model output. By ignoring the elements of order higher than 1, we can write introduce the Hessian H and the gradient G that are then used inside the fitting routine:

$$H_{js} \approx 2\sum_{i=1}^{N} J_{ij} W_i J_{is}, \quad G = 2\sum_{i=1}^{N} J^T W_i \Delta y \beta^{k+1} = \beta^k - H^{-1} G \tag{2.35}$$

The least squares method were performed on Python using the SciPy package (Jones, Oliphant, Peterson, et al. 2001), it is important to understand the different steps taken by the programs to be able to play with the different algorithms proposed by SciPy for least squares. One can have many different approaches to a problem. For example, in the case of a simple problem such as the fitting of a background on a polynomial model, a simple polynomial fitting via *numpy.polyfit* (Van der Walt, Colbert, and Varoquaux 2011) that uses least square method was performed.

On the other hand, regarding the fitting of the entire model defined in (2.16) for the whole diffractogram, a cost function was first minimized through the *scipy.optimize.minimize* method to fit the model with the Broyden Fletcher Goldfarb Shanno (BFGS) algorithm. This algorithm belongs to Quasi-Newtonian methods for which the Hessian matrix is not entirely computed but approximated via gradient evaluation. Constraints or boundaries were not used throughout the refinement, otherwise other algorithms must be used. In that case, for the *scipy.optimize.minimize* method, sequential quadratic programming (SQP) is used for nonlinear constrained problems with the condition that the cost function and the constrains are twice differentiable, hence the quadratic term. The *scipy.curvefit* method was also used at early stages for it allows quick fitting procedure, also customizable through the many arguments that can be taken into account. It would also have been possible to compute the Jacobian directly but using SciPy certified methods is easier although less transparent.

The precision of the result increases with the number of bins that must in any case be superior to the number of parameters. Using a whole-pattern fitting model increases the statistics and yields a superior model, the overlapping of the detector also contributes to finer results.

Validation criteria

The criteria used to assert the fitting is the weighed R-factor, given by:

$$R_W = 100\,\% \left(\frac{\sum_{i=1}^{N} W_i \left\{ y_i - f(x_i; \hat{\vec{\beta}}) \right\}^2}{\sum_{i=1}^{N} W_i\, y_i^2} \right)^{1/2} \tag{2.36}$$

If one knows precisely the crystalline structure and thus the structure factor, one can also use another R-factor by summing (1.45) and (1.72) for single peaks:

$$R_{Int} = 100\,\% \left(\frac{\sum_{hkl} |I_{hkl}(obs) - I_{hkl}(comp)|}{\sum_{hkl} |I_{hkl}(obs)|} \right) \tag{2.37}$$

The R_{int}-factor is quite versatile since if one manages to extract the nuclear or magnetic intensity, one can choose to compare them by writing a nuclear R_N-factor or a magnetic R_M-factor instead of the total R_{int}-factor. Especially for an experiment where the peak overlap is very low and the extraction of $I_{hkl}(obs)$ is facilitated. While using algorithm that works with least squares method, the output of the fitting procedure also gives information on the quality of the fitting depending on criteria proper to the algorithm. During the refinement, the residuals defined as $y_i - f(x_i; \hat{\vec{\beta}})$ are plotted for each data point under the model. Graphically analyzing the residuals gives a good general idea on whether or not the fitting succeeded and will be the standard way of asserting the goodness of the fit for this thesis.

For a least-square regression, the standard deviation of the error term is assumed to be equal and estimated from least squares equation by:

$$\hat{\sigma} = \sqrt{\frac{\sum_{i=1}^{N} [y_i - f(x_i, \hat{\vec{\beta}})]^2}{n - m}} \tag{2.38}$$

However, since the weighed least squares method here maximizes the likelihood of the weighed non-linear regression model, the standard deviation of the Gaussian errors are not equal anymore. Moreover, the test statistics follows a χ^2 distribution, in our case a Poisson distribution, for which the errors depend on the parameters of the process i.e. on the model. The model being a statistical process computed by the parameters β instead of a random process, to insure the best statistics, the weights are then taken from the model. Proceeding to a χ^2 goodness of fit test comes then naturally as a way to assert the quality of the fitting. However, the author did not have time to perform such tests.

2.3 Correction coefficients

A large part of this thesis was first spent on learning Python, JupyterLab, neutron powder diffraction and the diverse regression analysis methods that could be applied to neutron diffraction. First, it was necessary to begin with the fitting of single peaks to test the quality of the model and of the minimization algorithm (figure 2.11). The model gradually improved from a simple Gaussian to a model that could take into account multiple peaks allowing for example the utilization of zero-shifts and the common determination of the peak by U,V and W (figure 2.12). After constructing and testing different models to produce a single one that could be used for the fitting of all diffractogram and creating low time complexity modules with functions that could be applied to different data sets, the following method finally lead to conclusive results.

Once the model and the methods were clearly defined and understood, the next step was the determination of the correction coefficients that would be applied to each detector belonging to the 3T2 multidetector to correct the overall high intensity for medium q of the 3T2 diffractograms. This was done by the mean of the SPODI diffractograms that did not show such behaviour at room temperature. To proceed, a model was first fitted onto the SPODI diffractograms through a weighed least squares regression. The

peak areas of each peak were extracted from the models and utilized along with the background in the creation of a new model for the 3T2 diffractograms. Since the data for SPODI is only available at room temperature, for samples that were previously used at 3T2, the correction was performed on the latest diffractogram after the heating and cooling cycle for the 3T2 diffractograms, i.e. the last diffractogram recorded on cooling. These corrections had to be done for the four data sets corresponding to each composition. This first set of corrections was named "Intensity correction coefficient" and is then applied to each of the 3T2 diffractograms.

Moreover, proceeding to a first-hand correction with SPODI, adds to the overall quality of the future overlap corrections regarding the overlap of the detectors of 3T2. Indeed, if we performed a correction of the overlap between the neighbouring detectors of the 3T2 multidetector, some efficiencies and positions could have converged towards local wrong minimum since only the neighbouring detectors can be taken into account. One way to avoid this issue would have been to reiterate the corrections, however this could have possibly lead to false values linked to the accumulation of errors. By using SPODI first, that works with a 5 detector overlap, a first step towards the real values is taken, the final efficiencies that mean to correct the wrong overlap of the 3T2 detectors will be determined after. The SPODI corrections can be classified as long-range corrections taking into account a global intensity reduction for medium q whereas the next correction set is meant to specifically correct the overlap between the neighbouring detector.

2.3.1 Intensity correction coefficient

In the following section, we will discuss the determination of the correction coefficients for the $Ni_{1.05}MnSb$ data set. The figure in this section present the result for the $Ni_{1.05}MnSb$ data sets, the general results for each composition are given in the annex. First, the SPODI diffractogram recorded at room temperature was fitted through least squares method. In order to fit the model, initial parameters has to be determined, this holds for each fitting routine that is discussed. The initial parameters were determined graphically for each composition at SPODI and at 3T2., for a total of 8 sets of initial parameters. It was tried to change the initial parameters as a function of the temperature but the fitting routine converged towards the same final parameters even if the same initial parameters were used. The zero shift was first guessed to be equal to zero. The half width parameters U, V and W were computed using (2.3), (2.4) and (2.5) for SPODI.

The position of the peaks were also used to give an initial guess for the lattice parameter, the peak positions in the model being solely determined though their Miller indices and the lattice parameter (table 2.4 and figure 2.8). Hence, graphically determining the position of the peaks resulted in a first guess of the lattice parameter a. The result of this procedure is presented in the figure 2.13.

The second step was to repeat the procedure for the diffractogram recorded on 3T2. However, since the calibration was subject to discussion, the U, V and W parameter had to be first guessed from a first fitting routine rather than computed. For $Ni_{1.05}MnSb$, 27 measurements were performed at different temperatures, ranging from 045 °C to 975°C, by progressive heating and then by progressive cooling. Hence, a first fitting via least squares was done for which U, V and W were set as free parameter, common to all the peaks in a spectra but different for each temperature. The full width at half

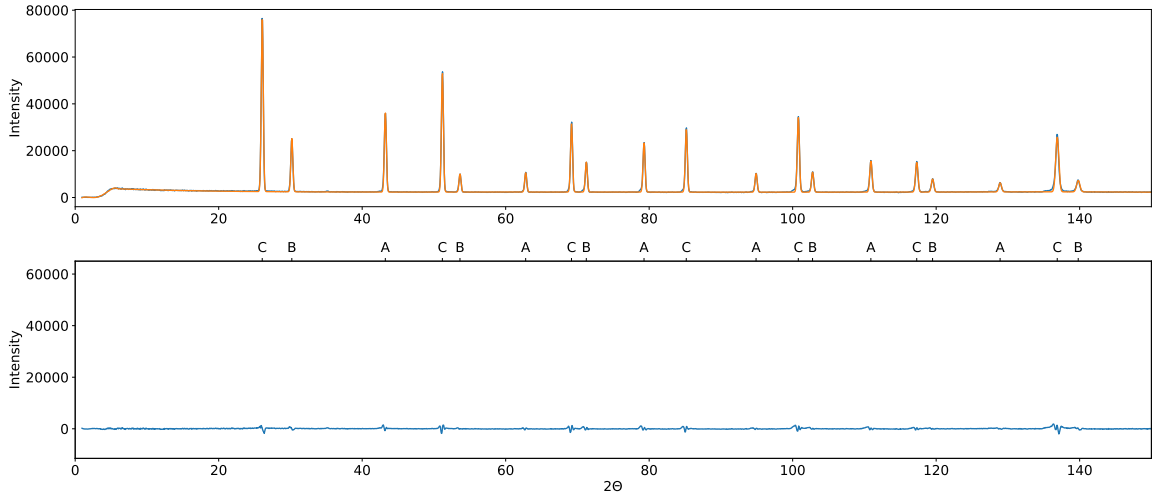

Figure 2.13: A SPODI diffractogram for $Ni_{1.05}MnSb$ at room temperature, model fitted through least squares methods with characteristics in annex. U V and W are fixed parameters.

height H was then computed from the resulting U, V and W at each temperature via (2.1). It can be seen that without using boundaries, the fitting is not conclusive for all the spectra (figure 2.14(a)). An average value of U, V and W was then taken over U, V, W values of the successful models (figure 2.14(b)) and then fixed for the following fitting routines.

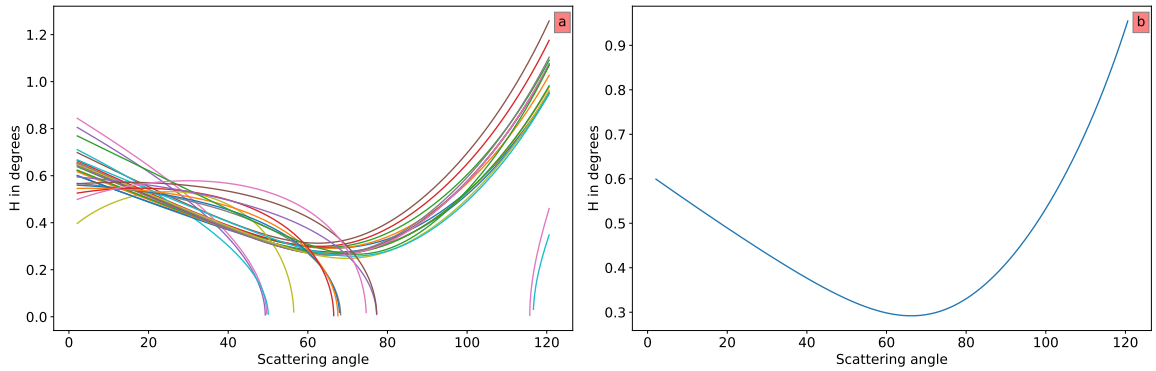

Figure 2.14: The full width at half height H computed via (2.1) for each temperature as a result of the first fitting routine (a) and the final values taken for the fitting of the 3T2 diffractograms (b).

The lattice parameter also determined graphically for 3T2 is slightly different since the measurement at SPODI was performed on the same sample as for 3T2 but after an entire heating and cooling cycle up to 975°C. A second fitting routine was then performed with the refined U, V and W values to produce models for each one of the 3T2 diffractograms (figure 2.15).

After creating a model for SPODI and a model for 3T2, a third model was created, that would allow the correction of the intensity of 3T2 based on SPODI. This model consists of a background function and a peak function (2.16), the background and the peak intensity were corrected separately since it is not certain that the neutrons contributing to the background in SPODI follow the same ratio than for the contribution to the Bragg peaks.

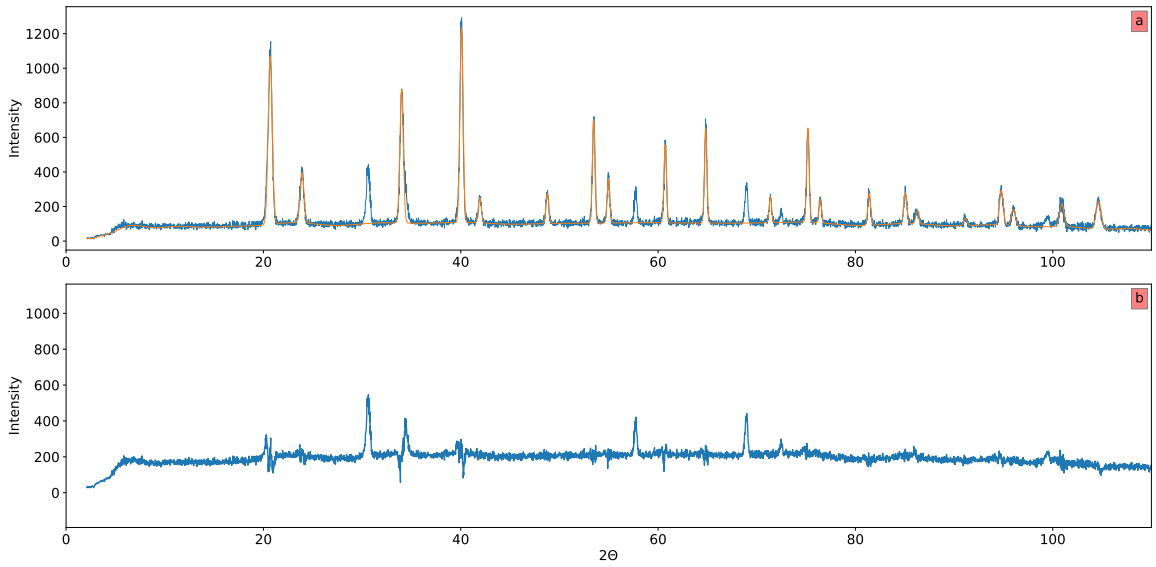

Figure 2.15: 3T2 diffractogram for $Ni_{1.05}MnSb$ at 200°C, model fitted through least squares methods with characteristics in annex. U V and W are fixed parameters.

First the peak intensity were corrected. The correction being performed on 3T2, the peak positions, the FWHH parameters (U,V,W) and the zero shift were kept from the model that was fitted on the 3T2 room temperature data set with fixed U,V,W values. One can notice by analysing the models of 3T2 and SPODI that since the incident wavelength λ is different between the two instruments, more peaks can be indexed on the 3T2 diffractometer. It was hence impossible to correct the intensity of the last peaks of 3T2 since they did not have a SPODI counterpart. The intensity of the SPODI peaks were then normalised to avoid the scale parameter linked to the instrument and divided by their respective Lorentz factor (2.15) and multiplied by a new Lorentz factor corresponding to their peaks on 3T2. The Lorentz factor differs due to its dependence on θ_k, the peak positions being different because of the different incident wavelengths. The intensities were then normalised again to take into account the 3T2 scale parameter. A small Debye-Waller factor was taken into account since the temperature are different between both experiments (200°c for 3T2, 20°C for SPODI), the multiplicities do not need to be corrected since they stay the same.

The background of SPODI was also utilized since the background of 3T2 suffered of the same calibration problems that resulted in higher intensities for medium q. Since SPODI and 3T2 do not have the same amount of points in the diffractograms (5200 for 3T2 versus 3910 for SPODI), the background of SPODI had to be plotted on a different domain and for a different amount of points. The background was also normalised for each point to take into account the different instrumental scale parameters. The final model is then shown in figure 2.16. One can notice that the background of the final model does not decrease with q nor increase for medium q. The intensity of the peak is also clearly too high for 3T2 especially around $2\theta = 40°$.

The peaks that are not fitted on any of the models are due to the sample's environment in 3T2 and cannot therefore be found on any of the SPODI diffractograms. They are hence absent from the models. Besides the peaks that can clearly be seen as not included in the model, there is a peak hidden behind the third peak of the model that explains the shape of this peak, larger at the bottom that any of the other peak.

These peaks can be seen for models fitted on other compositions, given in appendix. The satellite peaks were attributed to Vanadium or Niobium by a parallel refinement, the importance of using the U,V,W parameter is here underlined, allowing us to avoid any wrong peak broadening. Moreover, these peaks were problematic during the fitting since a comparison between the model and the diffractogram for a detector that does not show any Bragg peak related to the sample would only have background contribution from SPODI to the model but would still possibly have a Bragg peak related to e.g. Vanadium on the 3T2 diffractogram. This was taken into account during the refinement, by utilizing the fact that a general idea of the positions of our peaks was known, the other peaks were ignored during the fitting routine.

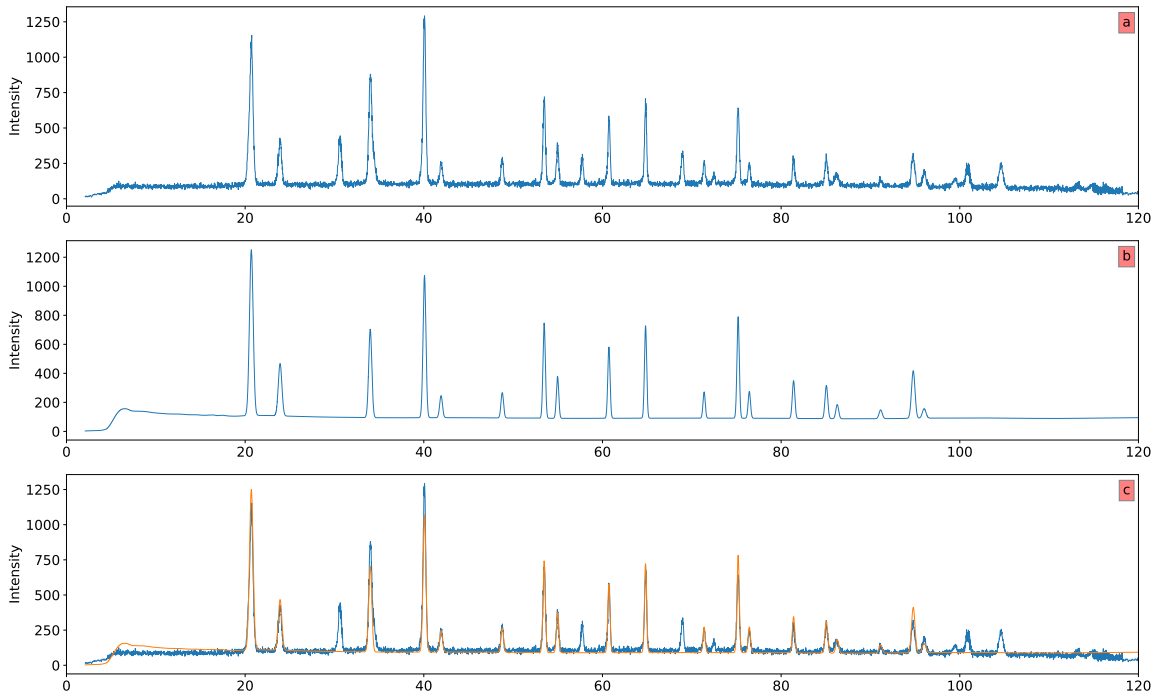

Figure 2.16: 3T2 data at 200°C for $Ni_{1.05}MnSb$ as a function of the scattering angle 2θ (a), model created by merging the SPODI and 3T2 models (b), Superposition of both curves underlining the intensity issues regarding the background and the peaks for 3T2 (c).

The intensity correction coefficients are obtained by utilizing the multidetector. Each detector is fitted to the model via least squares method in a reverse way by refining not the model but the original data to provide a first correction for the efficiencies of both the intensity of the peaks and the background. The correction coefficients are shown in figure 2.18. One can see that the corrections for the background follow a curve that first decreases up to medium q and then increases again, confirming that the background was too high for medium q. The evolution of the correction of the peak intensity follows what is seen in figure 2.16 with values superior to one when the the peak on the detector had higher intensities than in SPODI and inferior to one when the intensity on the detector was too weak compared to SPODI. The peaks are corrected by decreasing the intensity of the peaks around $2\theta = 40°$ and by increasing the intensity of the other peaks. Moreover, a detector can only see satellite peaks that do not exist on the SPODI diffractograms, it was not possible to correct the intensity of these peaks but leaving them as before would have impinged on the quality of the

diffractogram. The correction coefficients for these detectors was thus determined by interpolation using the neighbouring detectors.

A problem that arised during the correction is that since the shape of the background on SPODI (figure 2.16) is overall different from the shape of the 3T2 diffractogram at the beginning. One can notice that the background at the beginning is now slowly decreasing when it was stable before (stable for early q but decreasing at middle q). In the end, since we work with the peak areas to extract information about the crystalline structure, correcting the peak intensities so that they would resemble the SPODI peaks was prioritized, moreover this region of the background is not too important.

The final result is shown in figure 2.17 after correction using the product of both efficiency corrections. Again, one can see that the background is flat and that the intensities of the peaks now follow the evolution of the intensity on the SPODI diffractograms. We now have 3T2 diffractograms that have their intensity corrected for both the peaks and the background and that are in agreement with the data collected at SPODI. The difference between the 3T2 data before and after the correction is shown in the figure 2.19.

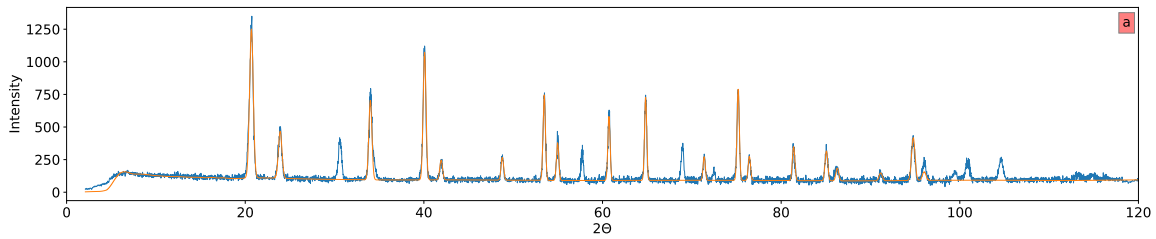

Figure 2.17: Superposition of both the corrected 3T2 data at 200°C for $Ni_{1.05}MnSb$ as a function of the scattering angle 2θ (blue) and the previous model that was created by merging the SPODI and 3T2 models (orange) (a).

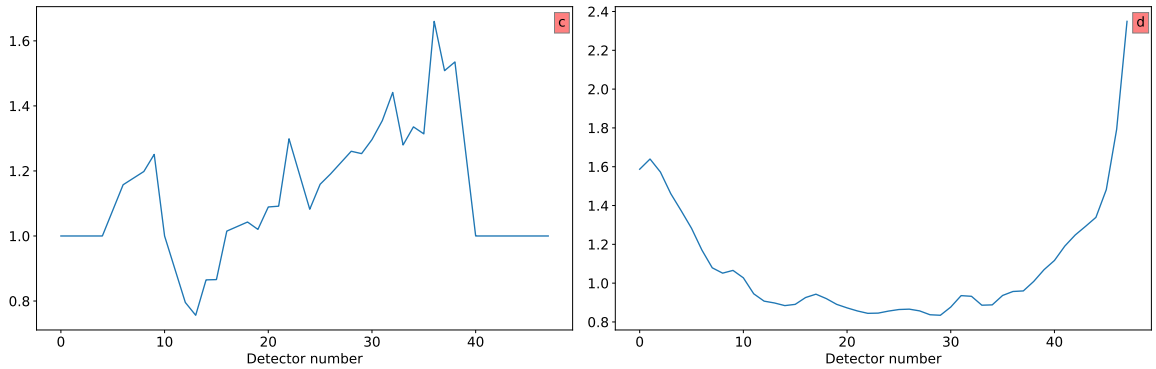

Figure 2.18: Intensity correction coefficients for the Bragg peaks, obtained by the means of the SPODI diffractograms and least square methods (b), intensity correction coefficients for the background, obtained by the means of the SPODI diffractograms and least square methods (b). Both correction coefficients are meant to correct the overall problems of intensity of the 3T2 diffractograms.

2.3.2 Overlap correction coefficient

The second set of correction coefficients is meant to correct the overlap between the neighbouring detectors. This set of coefficient is called "overlap correction coefficients"

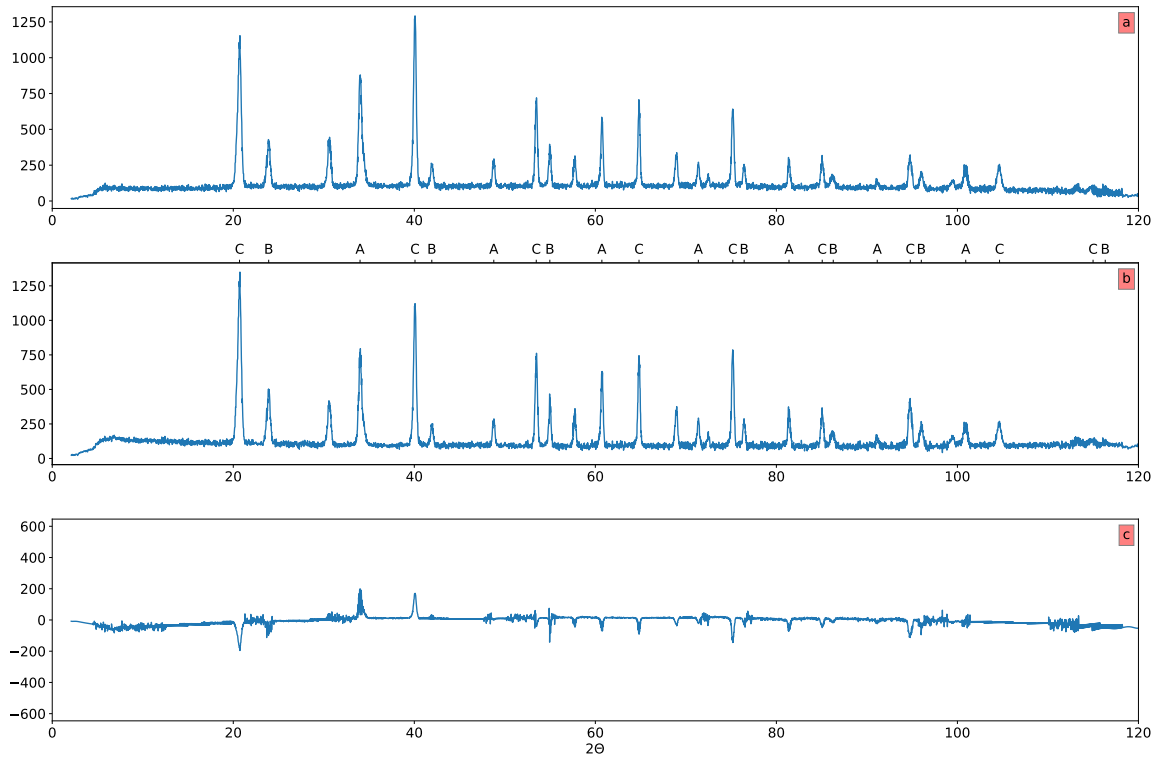

Figure 2.19: 3T2 diffractogram plotted at 200°C for $Ni_{1.05}MnSb$ without any corrections (a), 3T2 diffractogram plotted at 200°C for $Ni_{1.05}MnSb$ after each detector was corrected for its efficiency and position by the SPODI corrections (b), difference in the $(2\theta, y_i)$ bins (c).

and is obtained by creating new models via least squares method on the diffractograms that have already been corrected by the intensity correction coefficients. New models were produced (figure 2.20) for each diffractogram, for which the intensity of peaks and of the background clearly differs from the previous model (figure 2.15).

On one hand, for each one of the temperature dependant diffractograms corrected by the intensity correction coefficients, we have created a new model. This model if fitted through least square methods and uses the overlap between the neighbouring detectors to find the best value Y_i of a point linked to θ_i. For example if we have a (Y_i, θ_i) bin on the overlap between two detectors, ($Y_{i,L}$, $\theta_{i,L}$) the nearest bin given by the detector on the left and the ($Y_{i,D}$, $\theta_{i,D}$) the nearest bin given by the detector on the right. During the least square regression, the residues between the value computed by the model for $\theta_{i,L}$ and for $\theta_{i,D}$ are minimized (along with many other, taking into accounts their respective weights), thus the value given by the model for θ_i, is optimal and the regression analysis finds the best value for each point θ_i by taking into account the overlap of the detectors.

On the other hand, we still have the diffractograms with the wrong overlap between the neighbouring detectors but for which the true value of the efficiency and the shift of each detector can be estimated thanks to the models. The aim of the next procedure is to find the best values of the efficiency and shifts of each detector by comparing the models and the diffractograms. We thereby created a cost function with two parameters, efficiency and shift, that work on a single detector. We proceed via a least square regression minimizing the square of the difference between the value Y_i given by the detector over its range and the values of the model computed for each point θ_i on

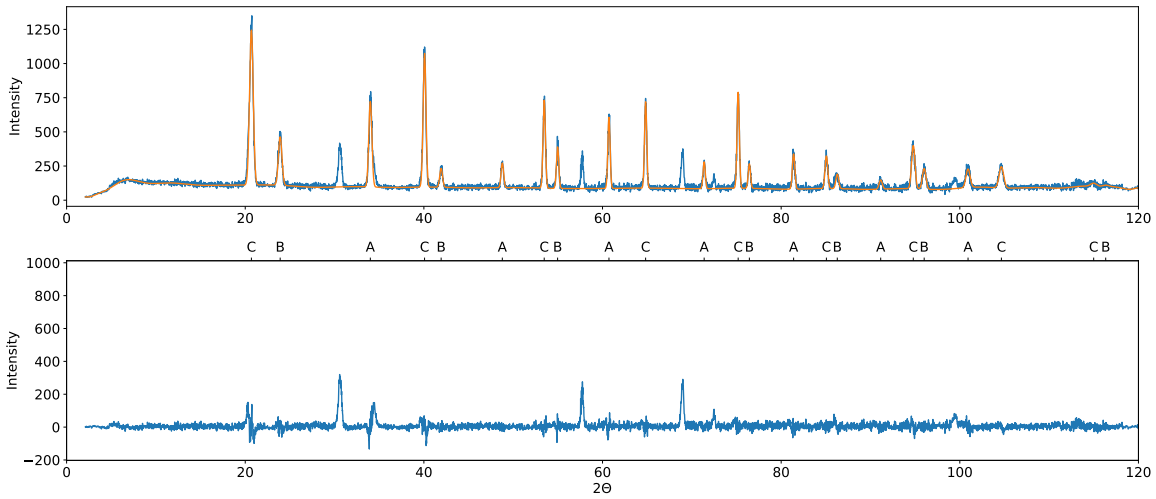

Figure 2.20: Model on corrected $Ni1.05MnSb$, 200°C diffractogram, fitted through LSM.

this range. This algorithm uses an efficiency e_D and shift s_D parameter, the optimal values of these parameters is given as an output and are then used as detector overlap correction coefficients. To maximize the statistics of this procedure, the cost function minimizes not only the residues for a single diffractogram but minimizes the residues for each temperature dependant diffractogram. For example if we have 27 temperature dependant diffractograms for $Ni_{1.05}MnSb$, the resulting efficiency and shift coefficients are the best taking into account each one of the diffractogram and not only for the room temperature which is mandatory since the coefficients must be constant over the experiment. The cost function is defined with pseudocode in (2.39).

$$cost_D(e_D,\, s_D) = \sum^{P} \left\{ \sum_{i}^{N} W_i \left\{ (y_i \times e_D) - f(x_i + s_D;\, \hat{\vec{\beta}}) \right\}^2 \right\}, \tag{2.39}$$

$$(e_{D,f},\, s_{D,f}) = minimize(cost, [1, 0]) \tag{2.40}$$

With P the amount of T-dependent diagram per composition, N the number of points that can be accessed by a detector D and $\vec{\beta}$ the parameters of the model that are defined beforehand during the fitting (figure 2.20). The initial guess taken for the efficiency and the shift is always respectively 1 and 0. After this procedure, the diffractograms are corrected for the overall increases of intensity at medium q by the intensity correction coefficients and for the overlap by the overlap correction coefficients. The efficiencies and shifts that constitute the overlap correction coefficients are shown in the figure 2.21.

One must be careful with the importance given to each diffractogram in the cost function, since the higher temperature diagram showed a much more erratic background curve, the value of the residue after the fitting of the model for a given $(\theta_i,\, y_i)$ bin was on average more important than the value for lower temperature diagram. The higher temperature diagram took then more importance inside the fitting routine than the lower temperature diagram, especially for the diagram recorded at temperatures higher than 800°C for which the Debye-Waller factor is so important that the second half of the diagram is mostly background, making it impossible to have a proper comparison between the models and the diagrams. This was countered by taking only the diagrams

up to 600°C into account. Another solution could have been to utilize the value of the Debye-Waller factor into creating new quotient for each diagram inside the fitting routine.

Regarding the evolution of the shift as a function of the number of the detector (figure 2.21), one can notice that the value tends to increases at first and to then decrease with θ, this could be due to an error in the lattice parameter or in the zero shift of the models, however the shift is very little and this should not have impinged on the final results. The high variations of the efficiency for the last detectors can also be explained by looking at the figure 2.22 where we can see that the last detector had an intensity output much lower than its neighbours. Overall the evolution of the efficiencies is not very important and each coefficient is close to one. This can at first be rather surprising but can be explained by the error of the points belonging to the peaks being higher because they receive more counts. Thus, the overlap is corrected but difficult to visualise.

One must keep in mind that some of the peaks due to the sample's environment were ignored during the procedure and that the overlap between the neighbouring detectors can still show some strong differences for these peaks. However, this phenomena should happen only for detectors that do not overlap with any other peak on the diffractogram and that cannot be corrected having thereby no effect on the final results.

Figure 2.21: The overlap correction coefficients for the shifts (a) and for the efficiencies (b).

2.3.3 Validity and discussion

This procedure has been repeated for each composition, leading to four different set of intensity correction and overlap correction coefficients. The reason behind this is that it is unsure that the calibration of the instrument was the same for each sample, the instrumental setup could have been changed between each experiment. Therefore, using separate coefficients is more careful. The results for each composition are shown in annex. If one wished to go through the algorithms used throughout the thesis, one can find the modules and functions on the GitHub of the author. The final values were given via scripts that are meant to be available in the future through a GUI.

The correction coefficients exist simply based on the assumption that the 3T2 data was wrongly calibrated. If it was not the case, there would have been no need to create a new set of coefficients, it could have been possible to simply use the coefficients given by the beamline scientists but the difference between SPODI and 3T2 was so obvious that it would have been wrong to interpret the data without performing some

corrections. It was our aim to produce the best corrections in the first part of this thesis, by tweaking the efficiencies and the shifts of the detectors, to obtain data sets onto which new models can be refined and used for the extraction of information on the crystalline structure.

Overall, fitting the diagram, even at high temperature was not the issue. It was more important to be certain that the final correction coefficient would not impinge on our analysis by being wrong or impossible to justify rather than helping by correcting the data. The difference between figure 2.22(a), figure 2.22(b) and figure 2.22(c) is quite obvious. The data does not exhibit the large intensity for medium q that was seen before, the overlap between the neighbouring detectors is also corrected and it is now possible to proceed to a satisfactory analysis of the data while being certain of the quality of the data.

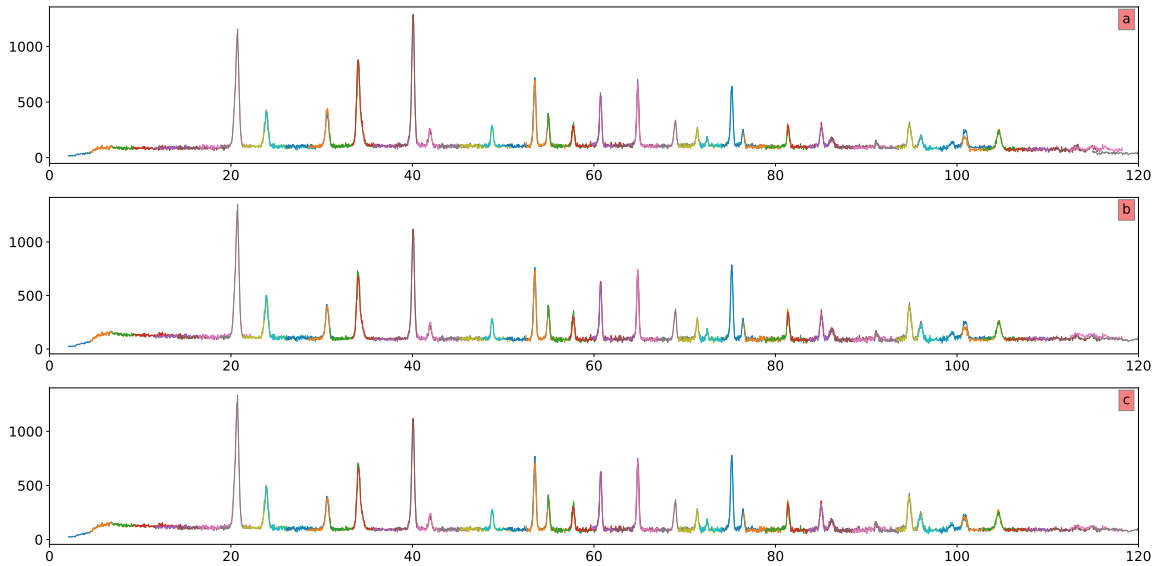

Figure 2.22: $Ni_{1.05}MnSb$, 200°C, 3T2 diffractogram plotted detector by detector without any corrections (a) with the first SPODI corrections (b) and with the final corrections (c).

Chapter 3

Understanding the ordering process in $Ni_{2-x}MnSb$

Introduction

This chapter is focused on the phase transition between a $L2_1$ structure to a $C1_b$ structure in Heusler alloys that exhibit both structures as a function of temperature and composition.

As presented in Chapter 1, full-Heusler alloys of the formula Ni_2MnSb crystallize in the cubic $L2_1$ structure (Castelliz 1951; Szytuła et al. 1972) whereas the half-Heusler NiMnSb alloys crystallize in the non-centrosymmetric cubic $C1_b$ structure (G. E. Bacon and Plant 1971; Ritchie et al. 2003). Furthermore, the $Ni_{2-x}MnSb$ system has proved to be a promising candidate for both ferromagnetic shape memory properties (Chatterjee et al. 2008) and magnetocaloric effects (Dubenko et al. 2009) near the off-stochiometric Ni_2MnSb full-Heusler structure due to antiferromagnetic properties and a transition towards a martensitic structure at lower temperature. On the other hand, NiMnSb is one of the first materials predicted to be a half-metallic ferromagnet (Groot et al. 1983) that showed attractive properties (Galanakis et al. 2006; J Brown et al. 2010) such as high Curie temperature that could be applied to spintronics as a half-Heusler (Wolf et al. 2001).

The degree of order in the lattice strongly influences the final properties of Heusler alloys, e.g. a film of NiMnSb shows a polarization of 58 % (Soulen et al. 1998) where it was expected to be fully spin-polarized (Groot et al. 1983). This result has been linked to atomic disorder and deviations from the perfect structure after first-principles calculation for NiMnSb (Orgassa et al. 1999) extended to other half-Heusler alloys (Zhu, Cheng, and Schwingenschlögl 2011). The importance of understanding the ordering process is still of utmost importance and has been subject to investigations in other half-Heusler such as NiMnGa (Lázpita et al. 2011) or recently in NiCrGa (Baral et al. 2019) with some element of answers, e.g. the introduction of an extending Slater-Pauling rule for systems with defects (Galanakis et al. 2006). The ordering in excess off-stochiometric Ni_2MnSb alloys is proven to have a direct impact on the stability of the martensitic phase (Sheuly Ghosh and Subhradip Ghosh 2019) that is fundamental for ferromagnetic shape memory alloys, the ordering process between B2 and $L2_1$ being printed on the martensitic phase during the transition from a high temperature austenite into a low temperature martensite via a diffusionless phase transition.

The $Ni_{2-x}MnSb$ system shows magnetic transitions as well as structural transitions

which have been studied by room temperature X-ray and neutron powder diffraction (Webster and Mankikar 1984); differential scanning calorimetry (DSC) (Nagasako et al. 2015; Hollender 2016), and diffusion triple method (Miyamoto, Nagasako, and Kainuma 2018). However, a half to full Heusler transition has never been studied precisely in terms of long-range ordering as a function of temperature, i.e. by scattering. Moreover, the kinetics of ordering and the origin of the phase transition are still unknown.

The determination of the atomic order in Heusler alloys can be determined via neutron powder diffraction experiments (Sánchez-Alarcos et al. 2013, room temperature measurements). In-situ temperature dependent neutron powder diffraction (NPD) has been performed by Neibecker (2018) on samples with different concentrations x of Ni to have a better grasp of the atomic scale dynamics during the $C1_b$ - $L2_1$ phase transition. Due to instrumental problems with the diffractometer 3T2 at LLB (Saclay, France), correction coefficients were determined by utilizing models first developed by Rietveld (1969) and Pawley (1981), computed using high-resolution diffractograms collected at SPODI in FRMII (Garching, Germany). In this chapter, we will discuss the ordering phenomena determined by the extraction of both structural and dynamical information covering a wide range of temperature and composition in $Ni_{2-x}MnSb$ following the refinement of new models on the corrected diffractograms.

3.1 The $L2_1$-$C1_b$ phase transition in $Ni_{2-x}MnSb$

The most recent phase diagram for the $Ni_{2-x}MnSb$ system is given by a representative combination of both DSC and High-Resolution Scanning Transmission Electron Microscopy (HRSTEM) (Nagasako et al. 2015) besides neutron powder diffraction measurements (Webster and Mankikar 1984), it is drawn in figure 3.1 as a function of the amount of Nickel in the alloy. Complementary measurements were performed by DSC and neutron powder diffraction (Neibecker 2018).

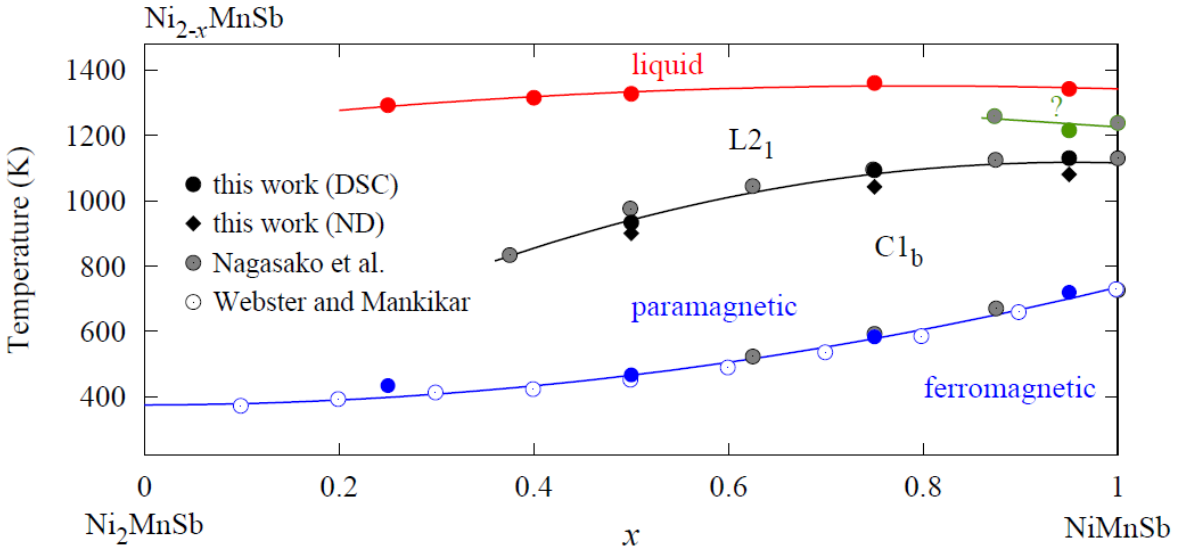

Figure 3.1: Latest phase diagram for the $Ni_{2-x}MnSb$ structure, given by the summation of the work of Webster and Mankikar (1984), Nagasako et et al. (2015) and Neibecker (2018).

The $L2_1$ order in the system is assumed to first result from short range order formation after the liquidus with a high number of anti-phase boundaries (APB) that

gradually grow during the ordering process into anti-phase domains (APD); characterizing the long-range order of the $L2_1$ structure and then of the $C1_b$ structure in the lattice. The correlation function describing the ordering process can be linked to the size of the anti-phase domains. However, one must determine what kind of ordering process takes place in the lattice during the following $C1_b/L2_1$ transition.

Room temperature diffraction results (Webster and Mankikar 1984) showed that the half-Heusler structure is stable for compositions going from NiMnSb to $Ni_{1.60}MnSb$ in a highly ordered $C1_b$ structure with vacancy occupancy on the C site (figure 1.3). Nevertheless, the ordering in NiMnSb proved to be a function of heat-treatment (J Brown et al. 2010) and vacancies have been identified randomly occupying both A and C site in NiMnSb. A magnetic transition has been confirmed for intermediate compositions of $Ni_{2-x}MnSb$ (Webster and Mankikar 1984; Nagasako et al. 2015). The emphasis if however on the continuous structural transition confirmed (Nagasako et al. 2015) between an $L2_1$ structure towards a $C1_b$ structure, for intermediate systems with composition ranging between $x \approx 0.40$ and $x = 1$. No features accompanying the structural transition was observed for $Ni_{1.75}MnSb$ in any of the DSC measurements, the kinetics being probably too slow and the compositions too similar for a transition to happen for composition with $x < 0.40$. Overall, these results suggest a vacancy order-disorder phase transition ruled by the dynamics of the structural vacancies. An additional transition for $x > 0.85$ has been identified by DSC measurements and could be the result of a transition between a disordered B2 structure to an ordered $L2_1$ structure for compositions near NiMnSb. This is however unclear since the intensity of the featured DSC peak was reported to decrease after several heating and cooling cycles (Neibecker 2018), requiring further studies. The stability of the $L2_1$ structure near Ni_2MnSb has also been confirmed experimentally for off-stochiometric composition near NiMnSb (Sánchez-Alarcos et al. 2013) and theoretically by density functional theory (DFT) (Sasioglu et al. 2004).

As the temperature is lowered, the lattice transforms from the $L2_1$ structure (figure 1.3) in which the Nickel and the structural vacancies are equally hosted by both the A and C sites to a $C1_b$ structure in which the structural vacancies and the Nickel are each hosted on one Nickel sublattice, specifically the Ni on the A site and the vacancies on the C site. This results in a breaking of symmetry and a second-order phase transition from a $L2_1$ structure towards a $C1_b$ structure. Another explanation could reside in anti-site disorder and the annihilation of structural vacancies during the transition.

A first approach to the temperature dependant phase transition can be derived via the Gibbs Free Energy G (Easterling and Sherif 2009) defined by:

$$G = H - TS \tag{3.1}$$

with H the enthalpy (J), T the temperature (K) and S the entropy (J/K). For a given composition, we assume that the structural transition is a vacancy order-disorder transition during which the $C1_b$ structure gradually becomes more energetically favourable regarding H than the $L2_1$ structure. By linking the entropy to disorder in the lattice, the entropy term clearly favours the $L2_1$ structure since disorder between the two Nickel sub-lattices maximises entropy. The entropy being proportional to the temperature of the system in the right term of (3.1), the difference in the right term gradually increases between the two structures with temperature. The transition would then be ruled by the configuration entropy of structural vacancies (Nagasako et al. 2015) resulting in $L2_1$ structures at high temperatures.

Since the entropy term is supposedly greater in the $L2_1$ structure than in the $C1_b$ structure, the enthalpy term of the $L2_1$ structure must be greater than for $C1_b$ structure to act as a counterpart at lower temperatures. For a system with vacancies, one can draw a simple picture by linking the enthalpy to the interaction between the vacancies. If one looks at the half-Heusler and full-Heusler system as defined by Graf (Graf, Felser, and Parkin 2011) (figure 1.1 and 1.2), one can determine two basic interaction for vacancies and their neighbours. If the vacancies are more favorably neighbours, then at low temperature the lattice would show a phase separation between MnSb on a NaCl structure and fully-ordered Ni_2MnSb. Since this phenomena is not observed, the vacancies tend to not be neighbours and the final result is a $C1_b$ structure. Complex models have been developed that take into account magnetic interactions (Rusz et al. 2006). Nevertheless, this chapter will be focused on experimental data to solve the ordering process.

3.2 Bragg peaks and structural analysis

3.2.1 X-Ray diffraction

To characterize the samples and assert their purity, the samples were first studied by X-ray diffraction. X-ray powder diffraction was performed on a laboratory Rigaku SmartLab diffractometer at Tohoku University, Japan using Cu-Kα radiation and a Bragg-Brentano geometry (figure 3.2). Samples for X-ray diffraction have been grounded manually to grain sizes $< 32\mu m$ after quenching from 1173K. The high-resolution X-ray diffractograms were then Rietveld refined for occupancy (table 3.1). This was done previously by Pascal Neibecker as a part of his PhD thesis (Neibecker 2018).

Compound	rel. Ni occ. (4a)	rel. Ni occ. (4b)	lattice parameter a (Å)
$Ni_{1.05}MnSb$	1.077(8)	-0.027(8)	5.93015(5)
$Ni_{1.25}MnSb$	1.074(10)	0.176(10)	5.97334(6)
$Ni_{1.50}MnSb$	1.125(12)	0.375(12)	5.99265(7)
$Ni_{1.75}MnSb$	1.097(20)	0.653(20)	5.99962(3)

Table 3.1: Refined relative site occupancies of Ni and lattice parameters for room temperature X-ray diffractograms of a series of $Ni_{2-x}MnSb$ samples quenched from 1173 K, taken from Neibecker (2018).

The occupancy of the 4a site is superior to one for each composition, a breaking of symmetry is observed between the 4a and 4b sites regarding the occupancies of Ni or of the vacancies. The refined occupancies on the 4a and 4b sites for Nickel, assuming fully ordered Mn and Sb sublattices, confirm a fully ordered $C1_b$ structure at room temperature, despite the quenching from 1173K, temperature at which all structures have a $L2_1$ order. It is possible that the kinetics of the transition were too fast and that there is no residual disorder from the $L2_1$ phase for $x > 0.5$ as reported by Hollender (2016). However, this can be surprising considering $Ni_{1.75}MnSb$ for which no structural phase transition was confirmed in previous DSC measurements (Nagasako et al. 2015; Neibecker 2018). It is possible that the two structures are too similar for this composition to measure a change by DSC and that there is no observable difference

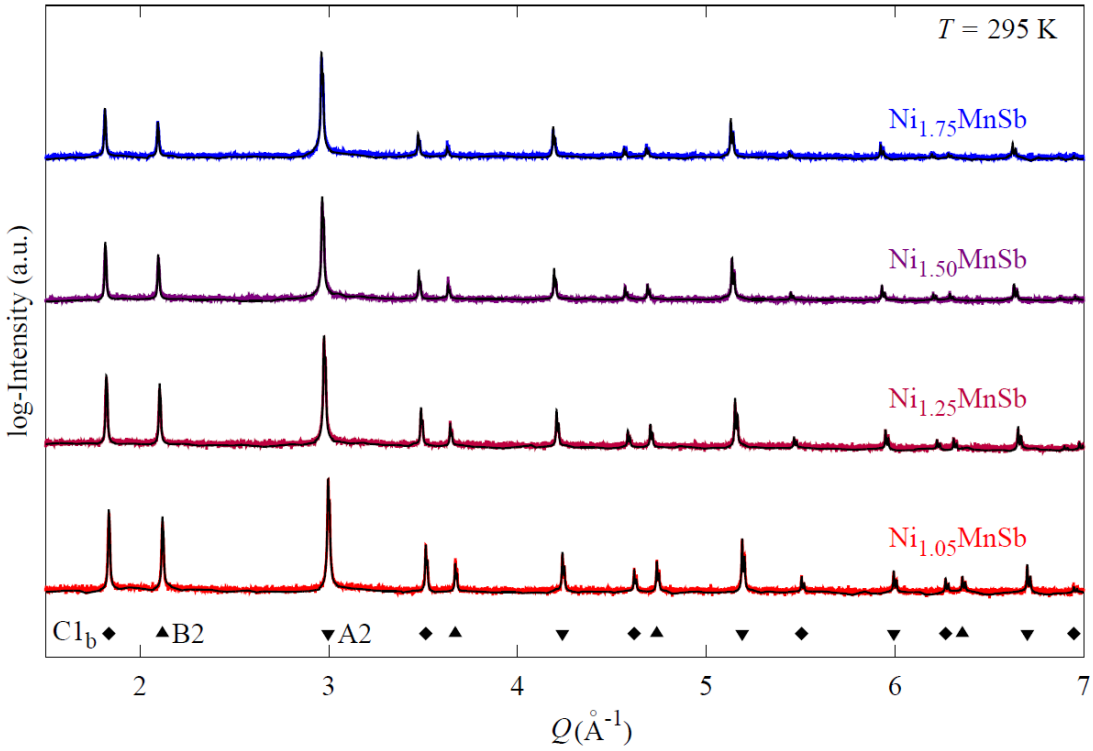

Figure 3.2: XRD diffractograms of $Ni_{2-x}MnSb$ samples on a logarithmic intensity scale showing the measured data (colored curves) and the Rietveld-refined diffractograms (black curves). The patterns have been recorded at room temperature using Cu-Kα radiation. Samples have been quenched from 1173 K. Peak families are indicated below the diffractograms, taken from Neibecker (2018).

between the $C1_b$ and $L2_1$ order for this composition. The slight deviations observed in the occupancy values could be the result of the hypothesis taken during the refinement, i.e. that the Mn and Sb sites are fully ordered, making it impossible to consider any anti-site disorder yet.

Moreover, an increase of the lattice parameter with the amount of Nickel is noted, constant with the values given in previous room temperature studies (J Brown et al. 2010; Webster and Mankikar 1984) with a maximum deviation of 0.14%. The value of the lattice parameter is of course sensible to the heat-treatment applied to the samples as it will be evidenced later.

The study was then performed by neutrons that allowed us to discriminate with more ease between Ni, Mn or Sb due to their coherent scattering length being much more different than their atomic form factor. Indeed we have $\sigma_{Ni} = 10.3\,barn$, $\sigma_{Mn} = -3.73\,barn$ and $\sigma_{Sn} = 5.6\,barn$.

3.2.2 Ordering and structure factor for neutron diffraction in $Ni_{2-x}MnSb$

It was shown that the atomic ordering in the lattice can in principle be determined from diffraction measurements, the analysis of the peaks giving insight into the position of the atoms in the lattice via the relative intensity of the structure factor. It is possible to proceed to the refinement of the site occupancy following Neibecker (2018). However, a more fundamental approach is preferred in this study by analyzing the structure

factor of the A2, B2, $L2_1$ and $C1_b$ structures. The expression of the structure factor can be derived from (1.46) for different order in the lattice, depending on the relative positions $\vec{r}$ of the atoms in the lattice. A first approach to the ordering in the lattice by computing the structure factor is given in the following table by assuming perfectly ordered A2, B2, $C1_b$ and $L2_1$ structure. Since the $L2_1$ structure is a superstructure of the B2 structure which again is a superstructure of the A2 structure, every peak in the diffractogram can be assigned to either the A2, B2 or $C1_b/L2_1$ family. A peak family being here defined as the peaks whose Miller indices are defined following the same symmetry rules, e.g. (h+k+l)=4n for the A2 peak family.

Bragg peak family	Order independent A2	Superstructure B2	Superstructure $C1_b$/L21
Miller indices of planes in Bragg condition	$(h+k+l) = 4n$	$(h+k+l) = 4n+2$	h, k, l all odd
Structure factor	$F = 4[(A+B+C+D]$	$F = 4[(A+C)-(B+D)]$	$F = 4[(A-C)^2+(B-D)^2]^{1/2}$

Table 3.2: Miller indices and structure factor of the crystalline planes associated to each peak family assuming perfect order and occupations.

The B2 structure is achieved before the $L2_1$ or $C1_b$ structure, the B2 structure possibly also showing disorder, it can be assessed through the B2 peak family. However, one can see through table 3.2 that only the intensity of the peaks differ between $L2_1$ and $C1_b$ associated to the same superstructure. Indeed, the Miller indices of the crystalline planes being the same, both peak families have the same peak positions (1.43) i.e. when h,k and l are all odd. The general solution of the structure factor derived for each family must be extended to $Ni_{2-x}MnSb$ with the A, B, C and D sites respectively occupied by Ni, $(1-x)Ni$, Mn and Sb in the $C1_b$ structure and by $(1-\frac{x}{2})Ni$, $(1-\frac{x}{2})Ni$, Mn and Sb in the $L2_1$ structure (figure 1.4). The intensity of the peaks within the same family is then only affected by the multiplicity, the Debye-Waller factor and the Lorentz factor (1.45). We have X, Y and Z respectively the scattering length of Ni, Mn and Sb and $(2-x)$ the relative amount of Nickel in our crystalline system. To resume, for a $C1_b$ structure, we have three family of peaks each characterizing one kind of order in the lattice and whose intensity is ruled by the three following equations.

$$F_{A2} = 4\,[\,(2-x)X + Y + Z\,], \tag{3.2}$$
$$F_{B2} = 4\,[\,(2-x)X - (Y+Z)\,], \tag{3.3}$$
$$F_{C1_b} = 4\,[\,(xX)^2 + (Y-Z)^2\,]^{1/2} \tag{3.4}$$

When for a $L2_1$ structure with both the 4a and 4b sites partially filled with vacancy, we have three family of peaks whose intensity is ruled by the next three following equations. As seen before, only the intensity of the last family differs.

$$F_{A2} = 4\,[\,(2-x)X + Y + Z\,], \tag{3.5}$$
$$F_{B2} = 4\,[\,(2-x)X - (Y+Z)\,], \tag{3.6}$$
$$F_{L2_1} = 4\,[\,Y - Z\,] \tag{3.7}$$

The important result extracted from these equations is that the structure factor, which defines the intensity of each peak family, can directly yield information about the ordering of the lattice. For example, the A2 structure factor results from all lattice sites contributing in phase, the structure factor of the A2 reflections is thereby only dependent on the general composition of the system. The B2 structure factor results in this case from a diffraction contrast between the 1a site (randomly occupied by Ni and vacancies) and 1b site (randomly occupied by Mn and Sb) of the B2 ($Pm\bar{3}m$) structure (figure 1.4). The $C1_b/L2_1$ structure factor results from the diffraction contrast between the 4a (occupied by Mn) and 4b site (occupied by Sb) of the $L2_1$ ($Fm\bar{3}m$) structure. There is also contribution from Ni on the 8c sites for $C1_b$ that allows us to differ between both order if full order is assumed for Mn and Sb.

The final goal of the refinement is to extract temperature-dependent structure factor and lattice constant that could then lead to a satisfactory microscopic explanation, in terms of vacancies and anti-sites, of the ordering process in $Ni_{2-x}MnSb$.

3.3 In-situ neutron powder diffraction

3.3.1 Refinement results

After the correction of the in-situ neutron powder diffractograms in Chapter 2, the refinement of the model was done via Pawley's method (Pawley 1981). Each peak is modelled by its peak intensity I_{hkl}, its peak position θ_k computed via the lattice parameter and a peak shape determined by the half-width parameters U, V and W (G.Caglioti 1958). The intensity of the peak here is not calculated from the structure factor in contrast with Rietveld refinement (Rietveld 1969). Having no overlap between neighbouring Bragg peaks in the diffractograms proved to ease the task, the Pawley method being known to show some limitations in the case of strong overlap that lead to the definition of new methods (Le Bail 2005). The refinement procedure took as argument the intensity of each peak, the lattice parameter, the zero shift and the half-width parameters (2.15).

The output of the refinement of each diffractogram was stocked in a Python class, taking advantage of the object-oriented aspect of this language, allowing a quick analysis of each diffractogram, mandatory when working with several data sets. Creating classes also allowed to introduce class methods that would then give additional information for each diffractogram such as the relative absolute squared structure factor (RASSF) defined earlier. Table 3.3 resumes the information stocked in each class and provides a simple picture of how one can extract miscellaneous information from the refinement of a model. Such a table can be printed for each one of the neutron powder diffractograms.

Room temperature neutron diffraction at SPODI

If the data acquisition at SPODI was first performed to correct the 3T2 diffractograms, it is also possible to proceed to the extraction of the structure factor from the Bragg peaks on this data-set, allowing to test the different models used before applying the method to the 3T2 data-sets. Room temperature neutron diffraction has been performed on 5 different samples. The $Ni_{1.75}MnSb$ sample was only quenched from 1173K when the other, also analyzed at 3T2, were slowly furnace cooled from high tem-

peratures during the in-situ neutron diffraction. No additional heat-treatment was performed after this. Since the quenched samples showed a fully ordered structure in the Rietveld refinement of the XRD data, a fully-ordered $C1_b$ structure should also result from the slow furnace cooled samples.

Miller indices	Peak area	Peak position (°)	Peak position ($Å^{-1}$)	Multiplicity	Lorentz factor	DWF	RASSF
(1, 1, 1)	16124.235510	25.981643	1.824843	8	10.154461	0.956273	207.563268
(3, 1, 1)	10644.084071	50.978134	3.493409	24	2.991032	0.848861	174.678528
(3, 3, 1)	6034.470406	68.878832	4.590902	24	1.895583	0.753528	176.029695
(3, 3, 3)	5591.257589	84.773835	5.472490	32	1.489577	0.668907	175.359962
(5, 3, 1)	6918.620968	100.261995	6.230517	48	1.324092	0.593794	183.325969
(5, 3, 3)	2963.421430	116.574978	6.905792	24	1.314371	0.527120	178.219160

Table 3.3: Miller indices, peak area, peak position, multiplicity, Lorentz factor, Debye-Waller factor and RASSF computed for the $C1_b$ peak family via refinement of the room temperature diffractogram recorded at SPODI for $Ni_{1.25}MnSb$.

One can extract the structure factor of each peak family for each composition from the diffractograms utilizing the peak intensity of each peak. Each peak is corrected by its multiplicity, Lorentz factor and Debye-Waller factor. One must be careful that the (6,0,0) and (4,4,2) peaks form the B2 family coincides due to the high symmetry of the cubic structure, giving a multiplicity of 30 for that peak. The same occurs in the $C1_b$ peak family for the (3,3,3) and (5,1,1) peaks with a multiplicity of 32. Moreover, the first peaks will have some contribution due to magnetism as seen in Chapter 1 (figure 1.8). Following literature reports by Brown (2010) and Galanakis (2006), a collinear ferromagnetic structure is considered (1.81). This contribution from magnetism can be excluded by modelling the magnetic structure factor dependence on q, one would then have to assume a certain ordering of the lattice to compute the magnetic structure factor since the contribution is mainly due to the Mn sites which is slightly counter-intuitive in out current approach. The peak with medium to high q-values having a magnetic contribution decreasing slower with q, the intensity of the first two peaks were ignored into the determination of the Debye-Waller factor due to important contribution from the magnetic structure. These results are presented for the $C1_b$ peak family in the table 3.3 for $Ni_{1.05}MnSb$ at SPODI.

Each peak is assigned to a peak family following its Miller indices. After the multiplicity, Lorentz and Debye-Waller correction, the value of the corrected peak intensity should be the same for each peak of the family, except for the magnetic contribution. The average of the corrected peak intensity is taken for each peak family and then divided by the corrected peak intensity of the A2 family to delete the instrumental contribution. One has then computed the relative squared structure factor for each peak family per neutron powder diffractogram. On the other hand, the relative absolute squared structure factor (RASSF) are then computed theoretically for different ordering of the lattice as a function of the amount x of Nickel in $Ni_{2-x}MnSb$ (table 3.4).

The final results for SPODI are presented in figure 3.3. It is evident that at room temperature, the data points follow the theoretical $C1_b$ curve rather than the $L2_1$ curve, proving that the lattice exhibits a $C1_b$ order at room temperature and confirming what had already been stated in previous studies. The possibility to discriminate between the $L2_1$ and $C1_b$ structures, despite common peak positions, is here highlighted. However,

A2	B2	$L2_{1,(Ni_{2-x})}$	$L2_{1,(MnSb)}$	$C1_b$
$(Ni_{2-x}MnSb)$	$(Ni_{2-x})(MnSb)$	$(Ni_{2-x})MnSb$	$Ni_1Ni_{1-x}(MnSb)$	$Ni_1Ni_{1-x}MnSb$
$4[(2-x)X+Y+Z]$	$4[(2-x)X-(Y+Z)]$	$4(Y-Z)$	$4(xX)$	$4[(xX)^2+(Y-Z)^2]^{1/2}$

Table 3.4: Equations followed for the computation of the theoretical relative absolute structure factor. The final results plotted in the following figures have been normalised regarding the intensity of A2. The brackets indicate a state of disorder.

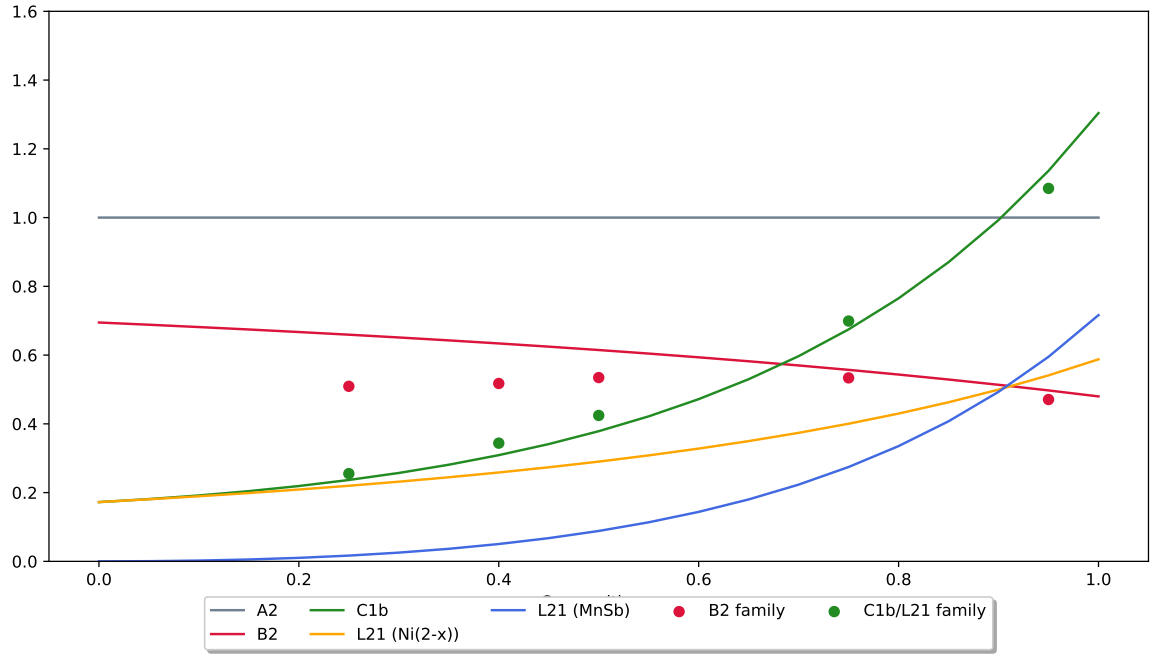

Figure 3.3: Room temperature relative absolute squared structure factors (RASSF) obtained via SPODI (circles) for the A2, B2 and $C1_b/L2_1$ peak families for 5 compositions of the $Ni_{2-x}MnSb$ system together with the calculated absolute squared structure factors under various types of disorder (lines). As introduced before, brackets indicate a state of disorder between the constituents.

one can notice that the B2 intensity is systematically too low when the $C1_b$ intensity is systematically too high, except for the $C1_b$ intensity in $Ni_{1.75}MnSb$ which is slightly lower. Overall, it seems that the system shows some disorder for all compositions but more importantly for compositions close to $Ni_{1.5}MnSb$ for which the two structures supposedly differ the most. We could also have deviations from stochiometry.

If one keeps in mind the previous equations (3.4) and the fact that the scattering length of Mn is negative. A first hypothesis can be formulated to explain the deviations observed in figure 3.3. If a Mn was to switch its 4c site with a vacancy on a 4b site, the result would be a decrease of the B2 structure factor with an increase of the $C1_b$ structure factor. This phenomena would be less important for compositions near NiMnSb in which the $C1_b$ structure is stable up to higher temperatures as evidenced in the previous figure. To confirm this hypothesis, the anti-site disorder, i.e. the transfer between a Mn and a vacancy must be energetically more favorable. Another possible explanation could hold in the annihilation of structural vacancies by the redistribution of the atoms inside the lattice (Alling, Shallcross, and Abrikosov 2006). However, more measurements are first needed to confirm the disorder in the lattice.

The precision of the measurements is crucial, as one can see the deviation for $C1_b$ are sometimes very little compared to the deviations for B2. Nevertheless, these results prove that diffraction measurements can be a powerful tool to understand the ordering in the lattice through the analysis of the peak intensities. This method has then been repeated for different temperatures on the 3T2 diffractometer at LLB (Saclay, France) to provide a full picture of the complex interplay between the anti-site disorder and the possible annihilation of structural vacancies in $Ni_{2-x}MnSb$.

In-situ neutron powder diffraction at 3T2

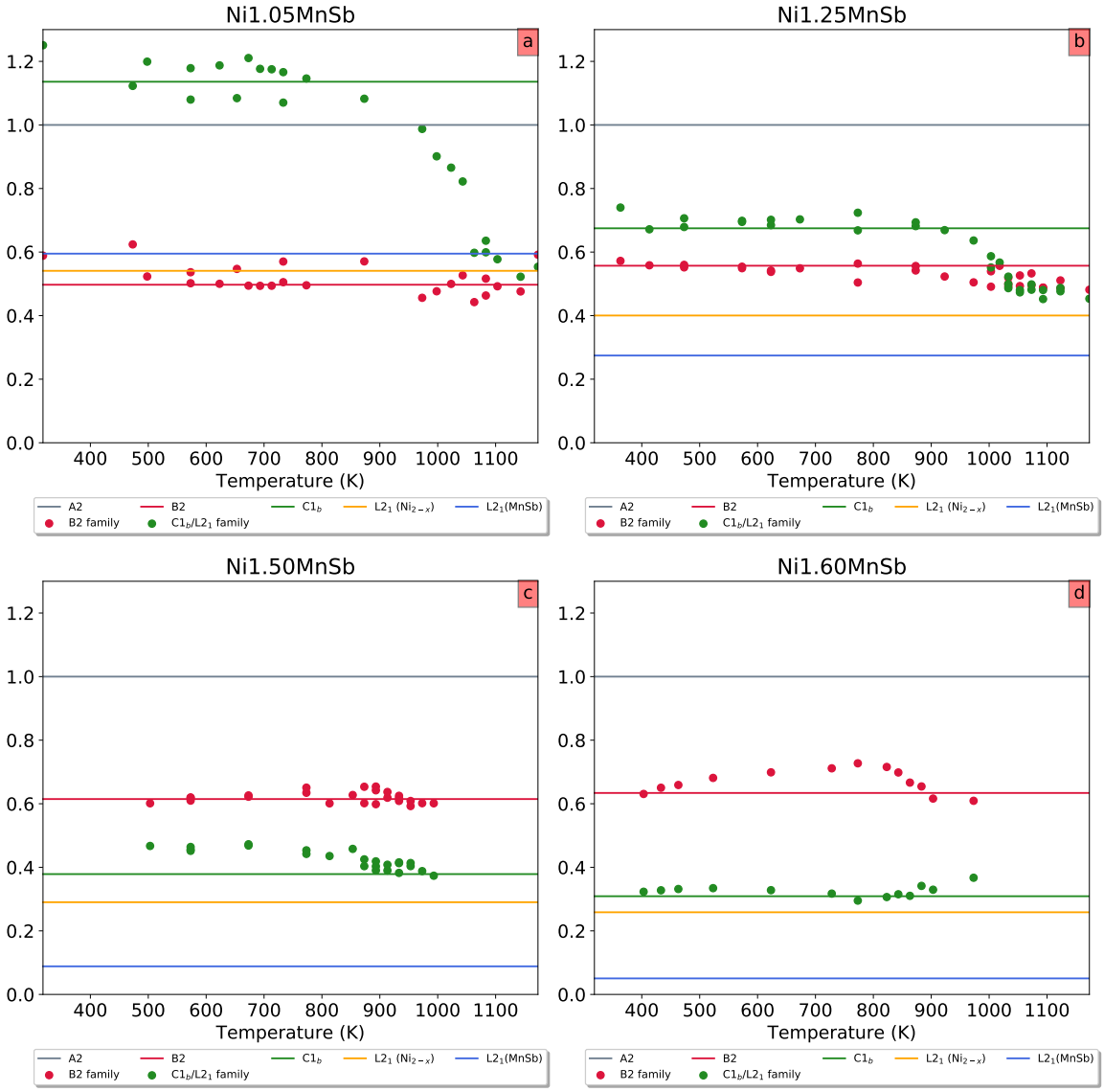

Figure 3.4: Temperature dependant relative absolute squared structure factors obtained via 3T2 (circles) for the A2, B2 and C1b/L21 peak families for 5 compositions of the $Ni_{2-x}MnSb$ system together with the calculated absolute squared structure factors under various types of disorder (lines). As introduced before, brackets indicate a state of disorder between the constituents.

For $Ni_{1.05}MnSb$, $Ni_{1.25}MnSb$ and $Ni_{1,50}MnSb$, the data acquisition was performed on both heating and cooling while $Ni_{1.60}MnSb$ was only measured on heating. Due to

relatively long acquisition times, it was not possible to measure the samples continuously upon heating/cooling. Instead, isothermal measurements have been performed at various temperatures. The temperature range of the data collection is set in accordance with the reported phase transitions by (Nagasako et al. 2015) for each sample. After correcting the data as seen in Chapter 2, the previous method has been repeated by correcting the intensity of each peak for the multiplicities, the Lorentz and the Debye-Waller factor in the A2, B2 and $C1_b/L2_1$ peak families. The importance of determining precisely the Debye-Waller factor is here underlined to be certain that the relative absolute squared structure factor computed at different temperatures can be correctly plotted on the same figure and analyzed without errors. The RASSF is plotted in figure 3.4 for four different compositions.

Regarding the low temperature values of the relative absolute squared structure factor for the B2 and $C1_b/L2_1$ peak families, all systems show a fully ordered $C1_b$ structure confirming the previous measurements at SPODI and the refined occupancies extracted from XRD. The transition between the fully ordered $C1_b$ and the disordered $L2_1$ structures is noticeable by the important decrease of the $C1_b/L2_1$ data points with temperature,. The data is first in accordance with the $C1_b$ curve at low temperatures and with the $L2_1$ curve computed for disorder between Ni and vacancy on the 4a and 4b sites at higher temperatures. This decrease is particularly strong for $Ni_{1.05}MnSb$ but only slightly noticeable in $Ni_{1.50}MnSb$ and absent in $Ni_{1.60}MnSb$. However, one can see that the phase transition is difficult to confirm for both compositions when the two curves are very similar in intensity.

Regarding the B2 points, it seems that they also tend to slightly decrease with temperature for $Ni_{1.05}MnSb$ and $Ni_{1.25}MnSb$, again the decrease is even less visible in $Ni_{1.50}MnSb$ and an interesting phenomena is featured in $Ni_{1.60}MnSb$ in which the B2 points tend to slowly increase around 500K before decreasing after 800K. This could be explained by deviations from stochiometry, as seen in figure 3.3, the relative intensity between the A2 family and the B2 or C1b families are dependent on the amount of Nickel in the lattice. A structure with higher amounts of Nickel would shift the relative B2 curve towards values closer to 0.7, the $C1_b$ curve towards values closer to 0.3 and the $L2_1(Ni_{2-x})$ curve even closer to the $C1_b$ curve. The observed data points would then respectively follow the B2 curve and be comprised between the $C1_b$ and $L2_1(Ni_{2-x})$ curves that are relatively close for $Ni_{1.60}MnSb$, proving that the transition is difficult to detect in this region.

Following the analysis of possible disorder between Mn and vacancies in the $C1_b$ structure previously written for the room temperature SPODI data, the intensity of the B2 and $C1_b$ peak families were expected to be respectively lower and higher than their theoretical curves for temperatures well into the $C1_b$ thereby confirming that the $C1_b/L2_1(Ni_{2-x})$ phase transition is not only the result of mixing between Ni and vacancies. This phenomena is observed for $Ni_{1.50}MnSb$ and $Ni_{1.60}MnSb$. However, a global conclusion cannot be drawn here due to different behaviours of the structure factors regarding the different compositions. Another hypothetical explanation to the phase transition could be given by density functional theory (DFT) of structural defects energies and was first drawn determined by Neibecker (2018). The possibility of thermal vacancy annihilation, with a global rearrangement of the lattice resulting in the reduction of the total amount of unit cells. The energy of different process such as atomic swaps and anti-sites were computed by Alling Alling, Shallcross, and Abrikosov 2006 for NiMnSb, assuming a fully ordered structure, in the optic of keeping

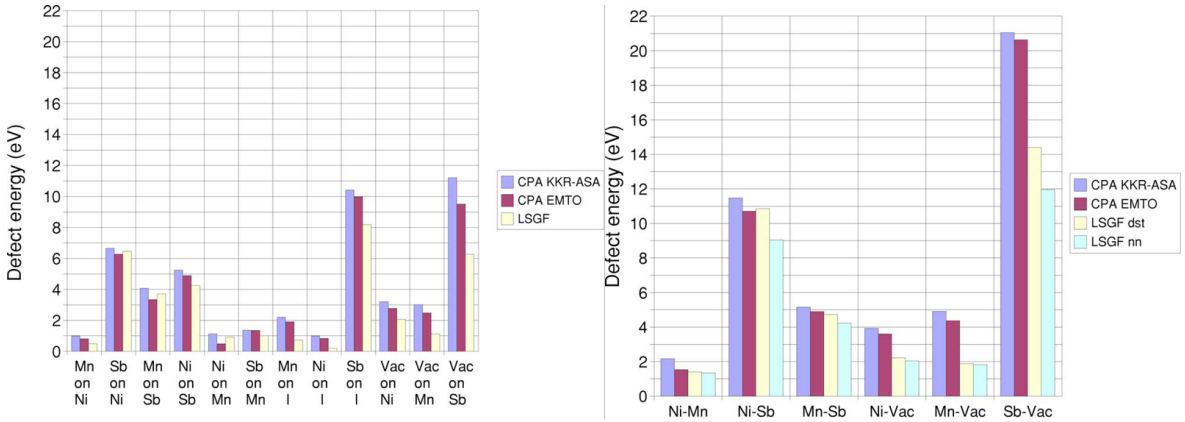

Figure 3.5: Energies of anti-site defects (left) and atomic swap defects (right) in $C1_b$ NiMnSb. For the swap defects, the energy of the distant and nearest-neighbor swap are respectively in the third and fourth columns. Computed by different methods, taken from Alling, Shallcross, and Abrikosov 2006 .

the half-metallic character of the alloy. Some possible processes resulting in vacancy annihilation are detailed in the table 3.5. The idea being the redistribution of 1Ni, 1Mn and 1Sb to effectively reduce the total amount of unit cell by one. The process with the lowest activation energy would then be the most likely to happen.

Energy cost	Defects created	Process
2.67 eV	4 defects	1Sb on Mn site, 2Mn and 1Ni on vacancy sites
2.63 eV	5 defects	1Sb on Mn site, 1Mn on vacancy site, 1 Mn on Ni site, 2 Ni on vacancy sites
2.59 ev	6 defects	1Sb on Mn site, 2Mn on Ni sites, 3 Ni on vacancy sites

Table 3.5: Energy cost and amount of defects created for different vacancy annihilation process. The energy is computed by utilizing the swap or anti-site energy of individual process given by Alling, Shallcross, and Abrikosov 2006.

The measurements being performed on NiMnSb and for individual defects, it can be difficult to be certain of the precision in the energy calculation of the processes resumed in table 3.5, especially when it comes to multiple defects. However, it proves that such dynamics could be possible in our system. An example of disorder is given.

Some elements have a preferential site onto which migrating is less costly (figure 3.5). Mn on a Ni site (0.49 eV) and Mn on vacancy site (0.73eV) are both relatively cheap compared to other types of anti-site disorder. E.g. Sb on Ni costs 6.47 eV and Sb on vacancy costs 8.19 eV. Overall, Sb shows high energy defects besides anti-site Sb on Mn three to four times cheaper than any other defect. This has been computed assuming a fully ordered C_b structure. Nevertheless, a qualitative description of the an energy-wise plausible process could be as follows. Combining Sb on Mn site and Mn on Ni/vacancy sites, one would then have Ni, Mn and vacancies on the 4a and 4b sites while having Sb and Mn of the 4c and 4d sites. This would result in a decrease of the B2 and $L2_1$ peak families intensity at high temperature for a $L2_1$ structure. Such decreases are observed for $Ni_{1.05}MnSb$ at high temperatures and perhaps in $Ni_{1.60}MnSb$ after correction of stochiometry.

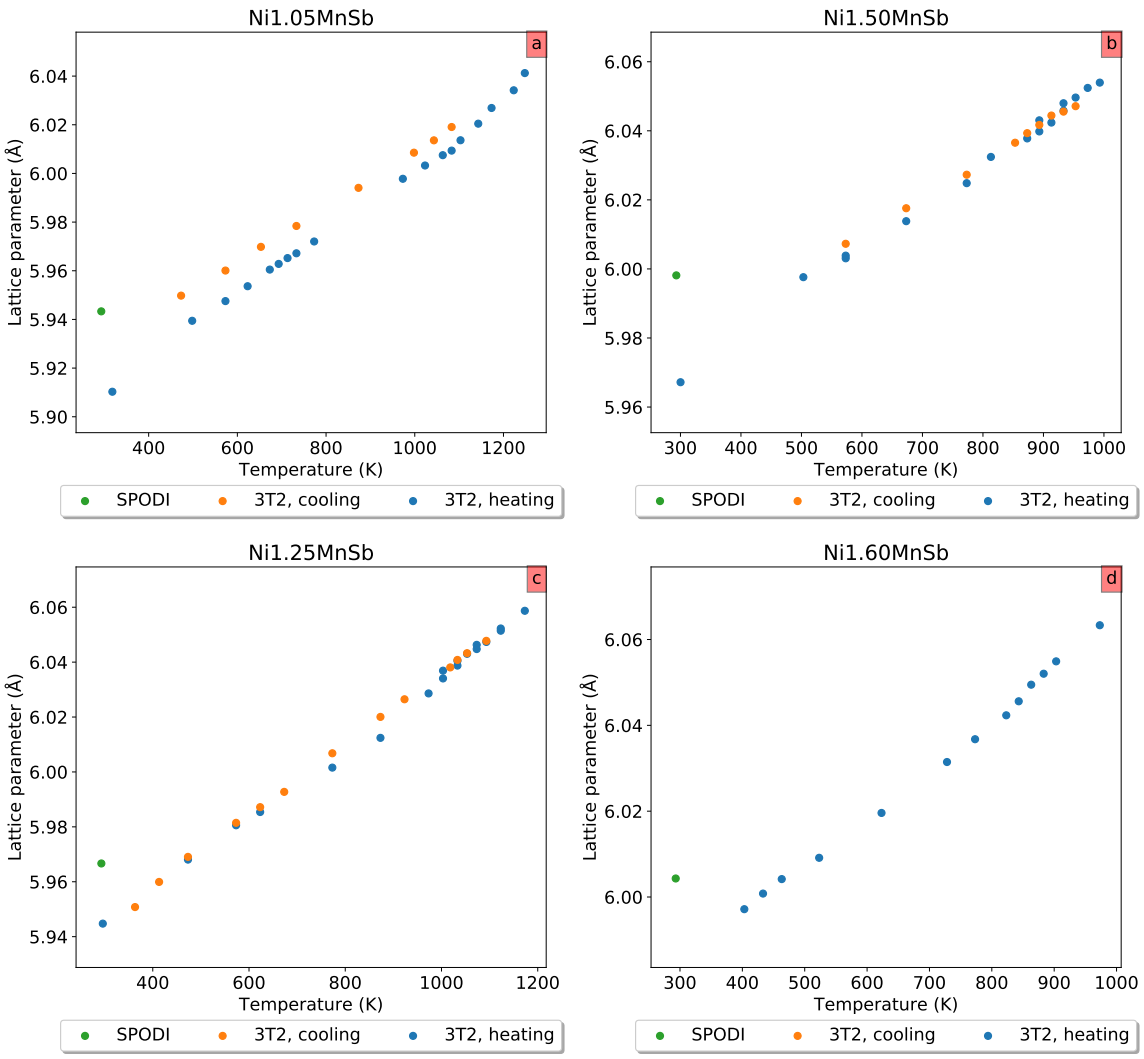

Figure 3.6: Temperature dependent lattice parameters for four compositions of the $Ni_{2-x}MnSb$ (a,b,c,d) system as obtained from in-situ neutron diffraction at 3T2 (heating and cooling) and from SPODI.

Lattice parameter

By directly refining for the lattice parameter, one can plot its evolution as a function of temperature for the four intermediate composition (figure 3.6). All samples have been first quenched from 1173K, then slowly heated and cooled in a furnace during the acquisition at 3T2, they were then again measured at SPODI. The lattice parameter a increase with the amount of Nickel can be understood intuitively, the lattice increasing in size with more Nickel and less structural vacancies. The values given by SPODI are overall higher than for 3T2.

At room temperature, the results seem to be consistent with the lattice parameter given by X-Ray in table 3.1, who themselves showed a maximum deviation of 0.14% with literature (Webster and Mankikar 1984). The 3T2 values seem however to be systematically lower than both literature and X-Ray values. This could be explained by the linear decrease in the shift observed in Chapter 2 and might need additional refinements.

Moreover, a difference between heating and cooling is observed for $Ni_{1.05}MnSb$,

$Ni_{1.25}MnSb$ and $Ni_{1.50}MnSb$. The lattice parameter is constantly higher on cooling for $Ni_{1.05}MnSb$ whereas a slower increase is observed instead during heating compared to cooling for temperatures ranging between 750K and 950K in $Ni_{1.25}MnSb$ and between 550K and 800K in $Ni_{1.50}MnSb$. The phenomena is more obvious in $Ni_{1.25}MnSb$, the values merge then for both low and high temperatures. Due to the lack of data points, it is difficult to precisely determine the exact range of these deviations, making it uncertain whether or not the slower increase of the lattice parameter is related to the structural transition, the magnetic transition being too far off for both structures.

What first comes to mind when observing a difference in the lattice parameter between heating and cooling is the annihilation of quenched-in vacancies. This however would result into an increase of the lattice parameter during cooling. Then comes the problem that one must find a phenomena that causes the lattice parameter to decrease linearly but result into a slower increase on a given temperature range. Perhaps a process that needs a certain activation energy during the transition from $C1_b$ to $L2_1$ order. If the slower increase during heating was reversible and seen also during cooling, we could have a disordering process taking place on a given temperature range, e.g. disorder on the 4a and 4b sites. This could then be confirmed by the Debye-Waller factor through an abrupt increase due to disorder in the lattice. However, no such reversible transition is seen in the lattice parameter.

Debye-Waller factor

The Debye-Waller factor computed previously to obtain the evolution of the RASSF following (1.55) has been plotted as a function of temperature for the four intermediate compositions studied at 3T2 and for the room temperature results from SPODI. Logically, the value of the mean displacement increases with the temperature. The increase appears to be linear for $Ni_{1.25}MnSb$, $Ni_{1.50}MnSb$ and $Ni_{1.60}MnSb$. For $Ni_{1.05}MnSb$, the increase is much slower at first on heating, and seems to converge towards a higher value at room temperature. The Debye-Waller factor being proportional to the disorder in the lattice, vacancy disorder could start occurring only after 900K when the $C1_b$ structure approaches the $L2_1$ structure.

If one takes 1000K as a reference, one can see that the mean displacement increases with the amount of Ni in the $L2_1$ structure for high temperatures. For such temperatures, the lattice is highly disordered with Ni supposedly equally distributed between the 4a and 4b sites. The phonons could have a better propagation in compositions with less vacancies at high temperatures, explaining this observation.

3.3.2 Discussion

The evolution of the $C1_b/L2_1$ RASSF in figure 3.4 implies a structural transition between a fully ordered $C1_b$ structure as presented in figure 1.1 and a $L2_1$ structure with disorder between the Ni and the vacancies on the 4a and 4b sites. The phase transition is evident for compositions up to $Ni_{1.50}MnSb$. It is clear, however, that the ordering process in the lattice is more complex than expected. Different types of disorder in the lattice were presented to try to explain parts of the evolution of the peak families with temperature. Complementary calculation would be necessary to fully understand the phase transition in $Ni_{2-x}MnSb$. Density functional theory proved to be a standard tool to understand the general properties of Heusler alloys (Sasioglu et al. 2004) and shed light on the ordering process by giving susceptible types of anti-site and swap disorder

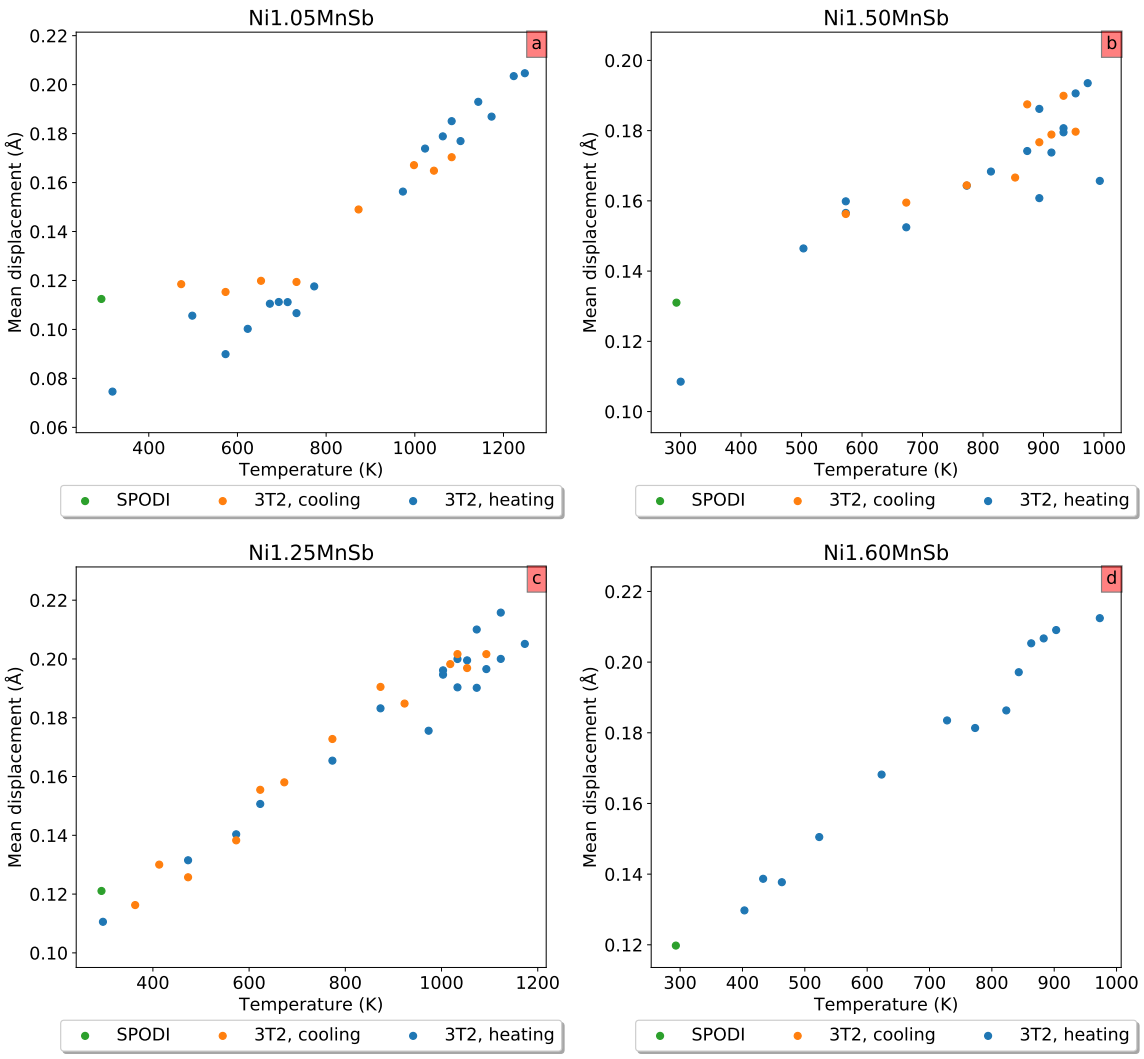

Figure 3.7: Temperature dependent Debye-Waller factor for four compositions of the $Ni_{2-x}MnSb$ (a,b,c,d) system as obtained from in-situ neutron diffraction at 3T2 (heating and cooling) and from SPODI.

in the lattice (Alling, Shallcross, and Abrikosov 2006) More specific computations for intermediate compositions and for different structures as well as the use of Monte-Carlo methods, in place for several decades to solve phase transitions (Binder 1985), could allow one to have a better grasp of the ordering process in $Ni_{2-x}MnSb$. Efforts are being made into this direction regarding Monte-Carlo simulations (Zweck and Leitner 2020).

Moreover, complementary in-situ X-ray diffraction measurements could be performed, offering better resolutions and demanding more detailed models to precisely describe the diffractograms. Hence, X-ray diffraction would allow one to see inherent broadening, due to strains or to anti-phase domains in the structure. Despite the fact that no contrast exists between Mn and other elements of the lattice with X-ray, it would be possible to extract X-ray weighted structure factor and occupancies for the lattice sites, allowing one to have a more precise understanding of the sublattices occupations with temperature. Furthermore, lattice parameters could be determined with more precision. Regarding the evolution of the anti-phase boundaries (APB) with

temperature, one could complement X-ray diffraction data with Lorentz transmission electron microscope measurements (Murakami et al. 2013), which allows one to see the spin-domains in the sample. The degree of order in the lattice and the magnetic properties of Heusler alloys are linked; as such, knowledge of the ordering process during the phase transition, and therefore the magnetism of the system could allow tailoring of the alloy's properties

Nevertheless, solutions have been found (Neibecker et al. 2014) to increase the ordering kinetics in Heusler alloys by retaining excess quenched-in vacancies, showing a promising future for Heusler alloys that up to now had limited applications due to disorder.

Conclusion

This thesis was focused on two separate yet complementary projects. The first being the understanding of process modelling applied to neutron diffraction curves, for the sake of determining new detectors efficiency and shift corrections coefficients. The newly determined coefficients allowing one to quickly correct entire data-sets after problems appeared during data acquisition and to then create a model that could be fitted on the diffractograms. The novelty here also being the combined use of diffractograms recorded on the same samples but at two different neutron diffractometers. The exact understanding of the modelling and correction process was deemed important. Rather than using existing programs, self-written scripts and functions were precisely determined for every aspect mentioned in the thesis.

Secondly, the ordering process for intermediate compositions of $Ni_{2-x}MnSb$ was investigated by the means of in-situ neutron powder diffraction. The possibility of determining the exact ordering process during the $C1_b/L2_1$ phase transition is of great interest due to numerous industrial applications besides the desire to truly understand the dynamics of this phase transition. An emphasis was put on the extraction of structural information from the models fitted onto the corrected diffractograms.

The correction coefficients that were applied to the 3T2 data sets were computed by using room temperature measurements performed at SPODI. Both the overlap between the neighbouring detectors and the intensity, too high for medium q, were successfully corrected and allowed new models to be refined on more qualitative data-sets. The $C1_b/L2_1$ phase transition has been confirmed through X-ray diffraction for the quenched sample (up to $Ni_{1.75}MnSb$) at room temperature with full order of Ni and vacancies on the 4a and 4b site, the 4b sites being shared between Ni and vacancies. Moreover, the structural analysis performed via the extraction of quantitative information from refined models computed on in-situ temperature dependent neutron diffractograms confirmed the $C1_b/L2_1$ phase transition on a wide range of temperature for intermediate compositions up to $Ni_{1.50}MnSb$. However, the ordering process proved to be complex and requires complementary approaches such as Monte-Carlo simulations, density functional theory or additional characterization of intermediate compounds via in-situ X-ray diffraction and TEM to be fully understood. Combining in-situ X-ray diffraction and density functional theory to compute the energy of various defects for intermediate compositions and $L2_1$ order could result in models relying on more complete data to understand the ordering process

Bibliography

Alling, Björn, S. Shallcross, and IA Abrikosov (2006). "Role of stoichiometric and nonstoichiometric defects on the magnetic properties of the half-metallic ferromagnet NiMnSb". In: Physical Review B 73, pp. 64418–. DOI: 10.1103/PhysRevB.73.064418.

Als-Nielsen, J and D McMorrow (2011). Elements of Modern X-ray Physics. 2nd. John Wiley & Sons.

Bacon, G E and J S Plant (1971). "Chemical ordering in Heusler alloys with the general formula A2BC or ABC". In: Journal of Physics F: Metal Physics 1.4, pp. 524–532. DOI: 10.1088/0305-4608/1/4/325.

Bacon, G.E. (1975). Neutron diffraction. 3rd ed. Oxford University Press.

Baral, Madhusmita et al. (2019). "Presence of atomic disorder and its effect on the magnetic and electronic properties of NiCrGa half Heusler alloy". In: Journal of Magnetism and Magnetic Materials 475, pp. 675–682. DOI: 10.1016/j.jmmm.2018.10.089.

Baxter, R.J. (1982). Exactly solved models in statistical mechanics. Academic Press.

Bewer, Brian (2012). "Soller slit design and characteristics". In: Journal of Synchrotron Radiation 19.2, pp. 185–190. DOI: 10.1107/s0909049511052319.

Binder, K (1985). "The Monte Carlo method for the study of phase transitions: A review of some recent progress". In: Journal of Computational Physics 59.1, pp. 1–55. ISSN: 0021-9991. DOI: https://doi.org/10.1016/0021-9991(85)90106-8.

Borfecchia, Elisa et al. (2013). "CHAPTER 5. Characterization of MOFs. 2. Long and Local Range Order Structural Determination of MOFs by Combining EXAFS and Diffraction Techniques". In: Catalysis Series Metal Organic Frameworks as Heterogeneous Catalysts, pp. 143–208. DOI: 10.1039/9781849737586-00143.

Brown, P. J. (2003). Neutron Data Booklet: Magnetic form factors. Old City Publishing.

Cardias, R. et al. (2017). "The Bethe-Slater curve revisited; new insights from electronic structure theory". In: Scientific Reports. DOI: 10.1038/s41598-017-04427-9.

Castelliz, L. (1951). "Eine ferromagnetische phase im system nickel-mangan-antimon." In: Monatshefte fur Chemie und verwandte Teile anderer Wissenschaften 82, pp. 1059–1085.

Chatterjee, S. et al. (2008). "Magnetic after-effect in Ni–Mn–Sb Heusler alloy". In: Journal of Magnetism and Magnetic Materials 320, pp. 617–621. ISSN: 0304-8853. DOI: 10.1016/j.jmmm.2007.07.023.

Dubenko, Igor et al. (2009). "Magnetocaloric effects in Ni–Mn–X based Heusler alloys with X=Ga, Sb, In". In: Journal of Magnetism and Magnetic Materials 321.7. Proceedings of the Forth Moscow International Symposium on Magnetism, pp. 754–757. ISSN: 0304-8853. DOI: 10.1016/j.jmmm.2008.11.043.

Easterling, D. A. Porter K. E. and M. Sherif (2009). Phase Transformations in Metals and Alloys. Revised Reprint. CRC press.

Galanakis, I et al. (2006). "Electronic structure and Slater–Pauling behaviour in half-metallic Heusler alloys calculated from first principles". In: Journal of Physics D: Applied Physics 39.5, pp. 765–775. DOI: 10.1088/0022-3727/39/5/s01.

Galanakis, I. and E. Şaşıoğlu (2011). "Structural-induced antiferromagnetism in Mn-based full Heusler alloys: The case of Ni2MnAl". In: Applied Physics Letters 98.10, p. 102514. DOI: 10.1063/1.3565246.

G.Caglioti A.Paoletti, F.P.Ricci (1958). "Choice of Collimators for a Crystal Spectrometer for Neutron Diffraction". In: Nuclear Instruments 3. DOI: 10.1016/0369-643X(58)90029-X.

Ghosh, Sheuly and Subhradip Ghosh (2019). "Role of composition, site ordering, and magnetic structure for the structural stability of off-stoichiometric Ni_2MnSb alloys with excess Ni and Mn". In: Phys. Rev. B 99 (6), p. 064112. DOI: 10.1103/PhysRevB.99.064112.

Graf, Tanja, Claudia Felser, and Stuart S.P. Parkin (2011). "Simple rules for the understanding of Heusler compounds". In: Progress in Solid State Chemistry 39.1, pp. 1–50. DOI: 10.1016/j.progsolidstchem.2011.02.001..

Groot, R. A. de et al. (1983). "New Class of Materials: Half-Metallic Ferromagnets". In: Phys. Rev. Lett. 50 (25), pp. 2024–2027. DOI: 10.1103/PhysRevLett.50.2024.

Hahn, Theo (2006). International Tables for Crystallography, volume A, Space-group symmetry. Ed. by Springer-Verlag. DOI: 10.1107/97809553602060000100.

Heusler, Fr. (1903). "Über magnetische Manganlegierungen." In: Verh. DPG 5, p. 219. DOI: 10.1002/ange.19040170903.

— (1904). "Über Manganbronze und über die Synthese magnetisierbarer Legierungen aus unmagnetischen Metallen". In: Angewandte Chemie 17.9, pp. 260–264. DOI: 10.1002/ange.19040170903.

Hoelzel, Markus, Anatoliy Senyshyn, and O Dolotko (2015). "SPODI: High resolution powder diffractometer". In: Journal of large-scale research facilities JLSRF 1. DOI: 10.17815/jlsrf-1-24.

Hollender, Lucas (2016). The C1b-L21 Transition in the $Ni_{2-x}MnSb$ System.

Hunter, J. D. (2007). "Matplotlib: A 2D Graphics Environment". In: Computing in Science Engineering 9.3, pp. 90–95. ISSN: 1521-9615. DOI: 10.1109/MCSE.2007.55.

J Brown, P et al. (2010). "Atomic order and magnetization distribution in the half metallic and nearly half metallic C1 b compounds NiMnSb and PdMnSb".

In: Journal of physics. Condensed matter 22, p. 206004.
DOI: 10.1088/0953-8984/22/20/206004.
Jones, Eric, Travis Oliphant, Pearu Peterson, et al. (2001).
"SciPy: Open source scientific tools for Python". In: URL: http://www.scipy.org/.
Juan Rodriguez-Carvajal, Thierry Roisnel (1998).
"FullProf.98 and WinPLOTR: New Windows 95/NT Applications for Diffraction Commission For Powder Diffraction".
In: International Union for Crystallography 20.
Lázpita, P et al. (2011). "Magnetic moment and chemical order in off-stoichiometric Ni–Mn–Ga ferromagnetic shape memory alloys".
In: New Journal of Physics 13.3, p. 033039. DOI: 10.1088/1367-2630/13/3/033039.
Le Bail, Armel (2005). "Whole powder pattern decomposition methods and applications: A retrospection". In: Powder Diffraction 20.4, pp. 316–326.
DOI: 10.1154/1.2135315.
Lynn, Jeffrey W. (2012). MAGNETIC NEUTRON SCATTERING. Vol. 2.
Wiley & sons, Inc., Hoboken, NJ.
McCusker, L. et al. (1999). "Rietveld Refinement Guidelines".
In: Journal of Applied Crystallography 32, pp. 36–50.
DOI: 10.1107/S0021889898009856.
McKinney, Wes (2010). "Data Structures for Statistical Computing in Python".
In: Proceedings of the 9th Python in Science Conference.
Ed. by Stéfan van der Walt and Jarrod Millman, pp. 51–56.
Miyamoto, T., M. Nagasako, and R. Kainuma (2018).
"Phase equilibria in the Ni-Mn-Sb alloy system".
In: Journal of Alloys and Compounds 772, pp. 64–71. ISSN: 0925-8388.
DOI: 10.1016/j.jallcom.2018.09.035.
Murakami, Y. et al. (2013). "Determination of magnetic flux density at the nanometer-scale antiphase boundary in Heusler alloy Ni50Mn25Al12.5Ga12.5".
In: Acta Materialia 61.6, pp. 2095–2101. ISSN: 1359-6454.
DOI: https://doi.org/10.1016/j.actamat.2012.12.029.
Nagasako, M. et al. (2015). "Order–disorder transition of vacancies from the full- to the half-Heusler structure in Ni2 − xMnSb alloys".
In: Intermetallics 61, pp. 38–41. ISSN: 0966-9795.
DOI: 10.1016/j.intermet.2015.02.014.
Neibecker, Pascal (2018). "Atomic order and its influence on functional properties of NiMn-based Heusler systems". PhD thesis. Technische Universität Munchen.
Neibecker, Pascal et al. (2014). "Increasing the achievable state of order in Ni-based Heusler alloys via quenched-in vacancies".
In: Applied Physics Letters 105.26, p. 261904. DOI: 10.1063/1.4905223.
Nelson, Andrew R. J. and Stuart W. Prescott (2019).
"*refnx*: neutron and X-ray reflectometry analysis in Python".
In: Journal of Applied Crystallography 52.1, pp. 193–200.
DOI: 10.1107/S1600576718017296.
"Neutron News" (1992). In: 3.3, pp. 29–37.
URL: https://www.ncnr.nist.gov/resources/n-lengths/list.html.
NIST/SEMATECH (2012). e-Handbook of Statistical Methods. Vol. 4. Methods.
URL: http://www.itl.nist.gov/div898/handbook/.

Oed, A. (2003). Neutron Data Booklet: Detectors for Thermal Neutrons. Old City Publishing.

Orgassa, D. et al. (1999). "First-principles calculation of the effect of atomic disorder on the electronic structure of the half-metallic ferromagnet NiMnSb". In: Phys. Rev. B 60 (19), pp. 13237–13240. DOI: 10.1103/PhysRevB.60.13237.

Pawley, G. S. (1981). "Unit-cell refinement from powder diffraction scans". In: Journal of Applied Crystallography 14.6, pp. 357–361. DOI: 10.1107/S0021889881009618.

Rietveld, H. M. (1969). "A profile refinement method for nuclear and magnetic structures". In: Journal of Applied Crystallography 2.2, pp. 65–71. DOI: 10.1107/S0021889869006558.

Ritchie, Lance et al. (2003). "Magnetic, structural, and transport properties of the Heusler alloys Co2MnSi and NiMnSb". English (US). In: Physical Review B-Condensed Matter 68.10, pp. 1044301–1044306. ISSN: 0163-1829.

Rusz, J. et al. (2006). "Exchange interactions and Curie temperatures in $Ni_{2-x}MnSb$ alloys: First-principles study". In: Physical Review B 73. DOI: 10.1103/PhysRevB.73.214412.

Sánchez-Alarcos, V. et al. (2013). "Effect of high-temperature quenching on the magnetostructural transformations and the long-range atomic order of Ni–Mn–Sn and Ni–Mn–Sb metamagnetic shape memory alloys". In: Acta Materialia 61.12, pp. 4676–4682. ISSN: 1359-6454. DOI: https://doi.org/10.1016/j.actamat.2013.04.040.

Sasioglu, Ersoy et al. (2004). "First-principles calculation of the intersublattice exchange interactions and Curie temperatures of full Heusler alloys Ni2MnX (X=Ga, In, Sn, Sb)". In: Physical Review B 70. DOI: 10.1103/PhysRevB.70.024427.

Soulen, R. J. et al. (1998). "Measuring the Spin Polarization of a Metal with a Superconducting Point Contact". In: Science 282.5386, pp. 85–88. ISSN: 0036-8075. DOI: 10.1126/science.282.5386.85.

Squires, G.L. (1997). Introduction to the Theory of Thermal Neutron Scattering. Dover.

Szytuła, A. et al. (1972). "Atomic and magnetic structure of the Heusler alloys Ni2MnSb, Ni2MnSn, and Co2MnSn". In: physica status solidi (a) 11.1, pp. 57–65. DOI: 10.1002/pssa.2210110105.

The reactor and the neutron sources (2003). URL: http://www-llb.cea.fr/spectros/pdf/neutron-source-llb.pdf.

Van der Walt, S., S. C. Colbert, and G. Varoquaux (2011). "The NumPy Array: A Structure for Efficient Numerical Computation". In: Computing in Science Engineering 13.2, pp. 22–30. ISSN: 1521-9615. DOI: 10.1109/MCSE.2011.37.

Van Laar, B. and W. B. Yelon (1984). "The peak in neutron powder diffraction". In: Journal of Applied Crystallography 17.2, pp. 47–54. DOI: 10.1107/S0021889884011006.

Waskom, Michael et al. (2014). seaborn: v0.5.0 (November 2014). DOI: 10.5281/zenodo.12710.

Webster, P.J. (1968). "The magnetic and chemical structure of the Heusler alloys". PhD thesis. Sheffield University.

Webster, P.J. and R.M. Mankikar (1984). "Chemical order and magnetic properties of the $Ni_{2-x}MnSb$ system". In: Journal of Magnetism and Magnetic Materials 42, pp. 300–308. ISSN: 0304-8853. DOI: 10.1016/0304-8853(84)90113-6.

Wolf, S. A. et al. (2001). "Spintronics: A Spin-Based Electronics Vision for the Future". In: Science 294, pp. 1488–1495. ISSN: 0036-8075. DOI: 10.1126/science.1065389.

Wolff, Maximilian et al. (2019). "Time Resolved Polarised Grazing Incidence Neutron Scattering from Composite Materials". In: Polymers 11.3. ISSN: 2073-4360. DOI: 10.3390/polym11030445.

Zhu, Zhiyong, Yingchun Cheng, and Udo Schwingenschlögl (2011). "Vacancy induced half-metallicity in half-Heusler semiconductors". In: Phys. Rev. B 84 (11), p. 113201. DOI: 10.1103/PhysRevB.84.113201.

Zweck, Ulrike and Michael Leitner (2020). "Antiphase domain growth on a cubic lattice." Unpublished article.

Appendix A

Models for correction

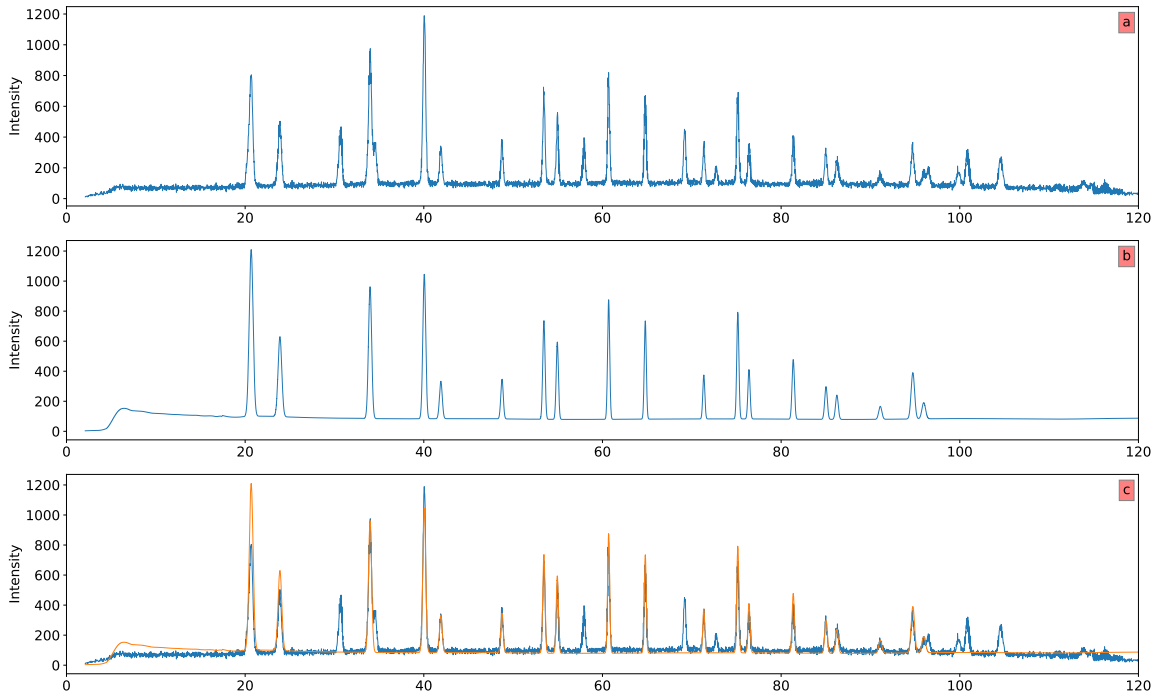

Figure A.1: 3T2 data at 200°C for $Ni_{1.25}MnSb$ as a function of the scattering angle 2θ(a), model created by merging the SPODI and 3T2 models (b), Superposition of both curves underlining the intensity issues regarding the background and the peaks for 3T2 (c).

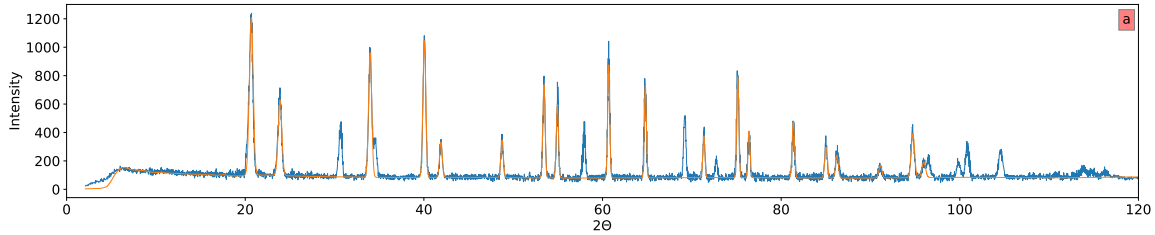

Figure A.2: Superposition of both the corrected 3T2 data at 200°C for $Ni_{1.25}MnSb$ as a function of the scattering angle 2θ(blue) and the previous model that was created by merging the SPODI and 3T2 models (orange) (a).

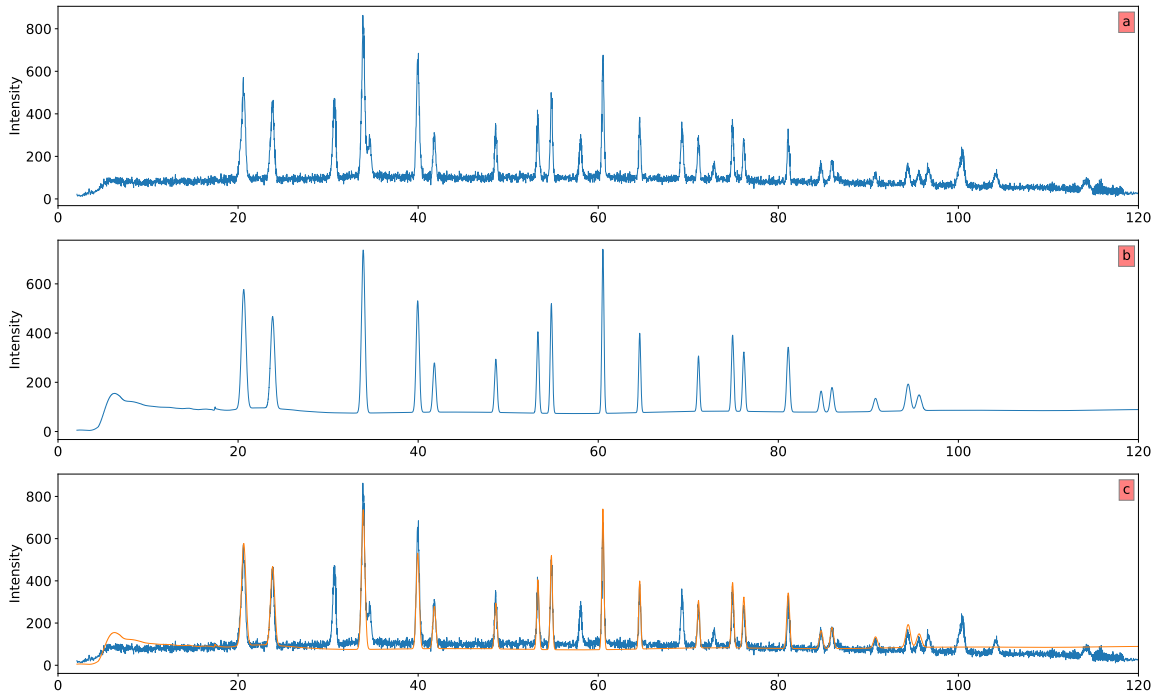

Figure A.3: 3T2 data at room temperature for $Ni_{1.50}MnSb$ as a function of the scattering angle 2θ (a), model created by merging the SPODI and 3T2 models (b), Superposition of both curves underlining the intensity issues regarding the background and the peaks for 3T2 (c).

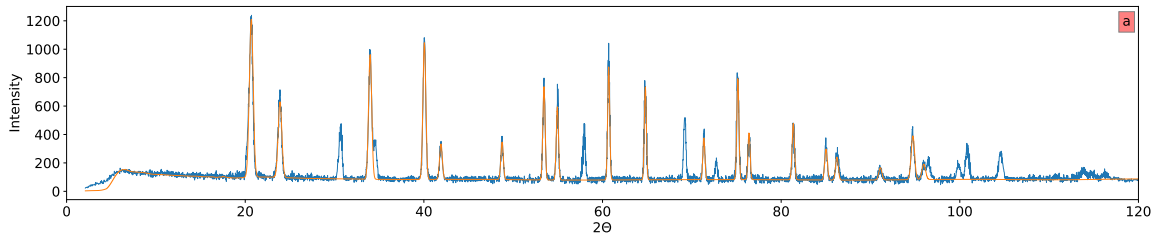

Figure A.4: Superposition of both the corrected 3T2 data at room temperature for $Ni_{1.50}MnSb$ as a function of the scattering angle 2θ (blue) and the previous model that was created by merging the SPODI and 3T2 models (orange) (a).

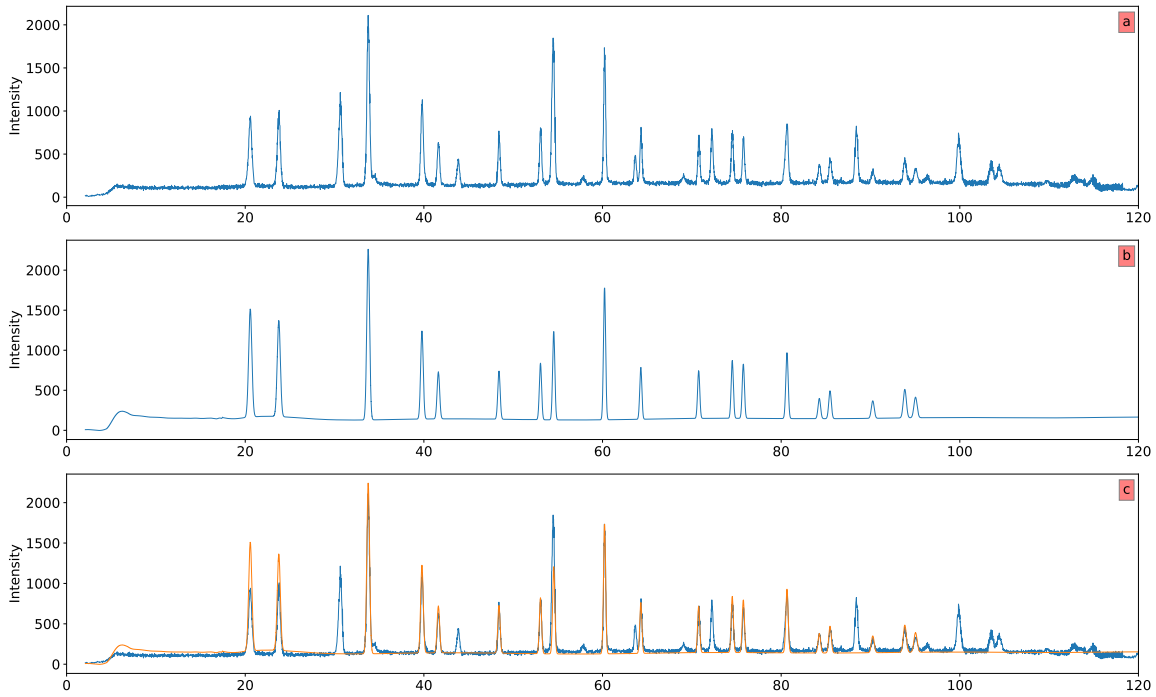

Figure A.5: 3T2 data at 130°C for $Ni_{1.60}MnSb$ as a function of the scattering angle 2θ (a), model created by merging the SPODI and 3T2 models (b), Superposition of both curves underlining the intensity issues regarding the background and the peaks for 3T2 (c).

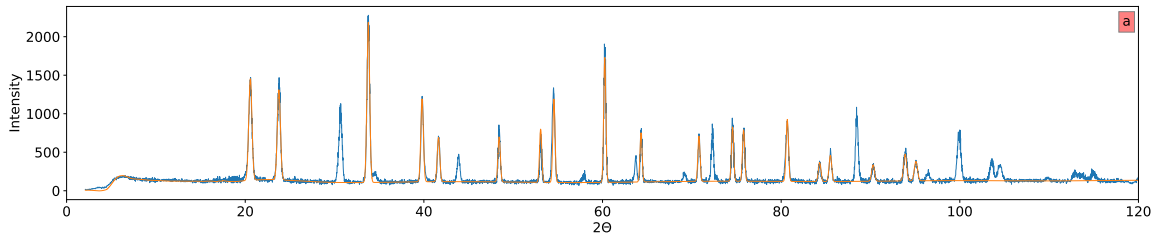

Figure A.6: Superposition of both the corrected 3T2 data at 130°C for $Ni_{1.60}MnSb$ as a function of the scattering angle 2θ (blue) and the previous model that was created by merging the SPODI and 3T2 models (orange) (a).